

<https://doi.org/10.14379/iodp.proc.369.107.2019>



Contents

- 1 Background and objectives
- 2 Operations
- 5 Lithostratigraphy
- 10 Biostratigraphy and micropaleontology
- 17 Paleomagnetism
- 24 Petrophysics
- 29 Geochemistry
- 33 Stratigraphic correlation
- 35 References

Site U1516¹

B.T. Huber, R.W. Hobbs, K.A. Bogus, S.J. Batenburg, H.-J. Brumsack, R. do Monte Guerra, K.M. Edgar, T. Edvardsen, M.L. Garcia Tejada, D.L. Harry, T. Hasegawa, S.J. Haynes, T. Jiang, M.M. Jones, J. Kuroda, E.Y. Lee, Y.-X. Li, K.G. MacLeod, A. Maritati, M. Martinez, L.K. O'Connor, M.R. Petrizzo, T.M. Quan, C. Richter, L. Riquier, G.T. Tagliaro, C.C. Wainman, D.K. Watkins, L.T. White, E. Wolfgring, and Z. Xu²

Keywords: International Ocean Discovery Program, IODP, *JOIDES Resolution*, Expedition 369, Site U1516, Hot Cretaceous Greenhouse, oceanic anoxic events, Mentelle Basin, Naturaliste Plateau, Great Australian Bight, Gondwana breakup, Tasman Gateway, Indonesian Gateway, cyclostratigraphy, carbon isotope excursions, Paleocene/Eocene Thermal Maximum, Eocene greenhouse, Miocene, volcanic rifted margin, nonvolcanic rifted margin

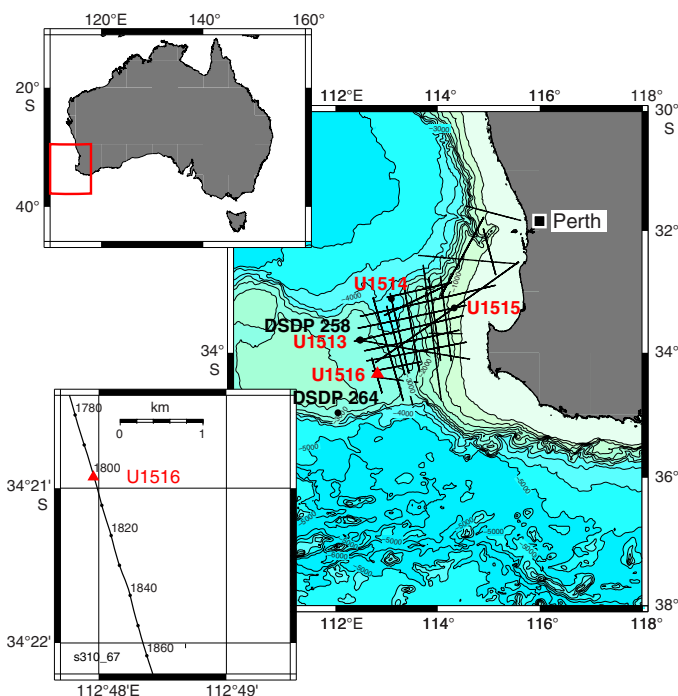
Background and objectives

International Ocean Discovery Program (IODP) Site U1516 (34°20.9169'S, 112°47.9553'E; Figures F1, F2) lies at ~2675 m water depth in the south-central Mentelle Basin. The basin is adjacent to the Naturaliste Plateau and was located at ~60°S paleolatitude during the mid-Cretaceous. Underlying the Mentelle Basin is synrift Permian to Jurassic sediment that is part of an earlier rifting event extending along the western margin of Australia (Borissova et al., 2002). Following the separation of India and Australia/Antarctica in the Early Cretaceous, the basin underwent a period of rapid thermal subsidence with deposition of a sequence of deltaic sediments, shale and claystone, followed by deep-water chinks and limestones. The current seabed is composed of Paleogene/Neogene/Quaternary oozes that overlie Cretaceous chalk (Maloney et al., 2011).

Objectives for drilling Site U1516 were as follows:

1. Obtain a continuous and expanded Cenozoic and Upper Cretaceous pelagic carbonate sediment record in the Mentelle Basin to reconstruct climatic shifts across the rise and fall of the Turonian and early Eocene hot greenhouse climates;
2. Determine the relative roles of productivity, ocean temperature, and ocean circulation at high southern latitudes during Cretaceous oceanic anoxic events (OAEs) and across the Paleocene/Eocene Thermal Maximum (PETM); and
3. Characterize how oceanographic conditions changed during the Cenozoic opening of the Tasman Gateway and the restriction of the Indonesian Gateway.

Figure F1. Location of Site U1516 on the western margin of the Mentelle Basin.



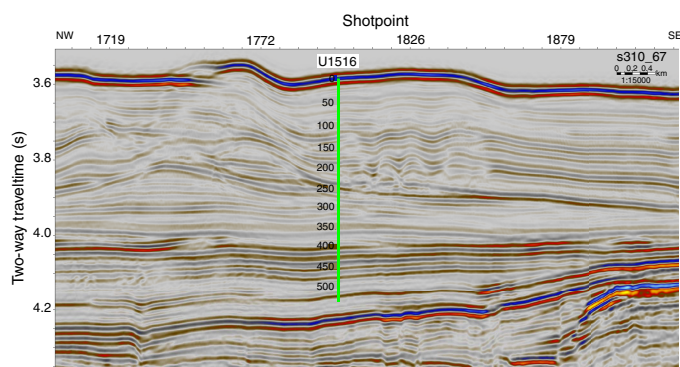
¹ Huber, B.T., Hobbs, R.W., Bogus, K.A., Batenburg, S.J., Brumsack, H.-J., do Monte Guerra, R., Edgar, K.M., Edvardsen, T., Garcia Tejada, M.L., Harry, D.L., Hasegawa, T., Haynes, S.J., Jiang, T., Jones, M.M., Kuroda, J., Lee, E.Y., Li, Y.-X., MacLeod, K.G., Maritati, A., Martinez, M., O'Connor, L.K., Petrizzo, M.R., Quan, T.M., Richter, C., Riquier, L., Tagliaro, G.T., Wainman, C.C., Watkins, D.K., White, L.T., Wolfgring, E., Xu, Z., 2019. Site U1516. In Hobbs, R.W., Huber, B.T., Bogus, K.A., and the Expedition 369 Scientists, *Australia Cretaceous Climate and Tectonics*. Proceedings of the International Ocean Discovery Program, 369: College Station, TX (International Ocean Discovery Program). <https://doi.org/10.14379/iodp.proc.369.107.2019>

² Expedition 369 Scientists' affiliations.

MS 369-107: Published 25 May 2019

This work is distributed under the [Creative Commons Attribution 4.0 International](https://creativecommons.org/licenses/by/4.0/) (CC BY 4.0) license. 

Figure F2. Prestack depth-migrated Geoscience Australia reflection seismic Profile s310_67 with location of Site U1516.



The Site U1516 sequence will be compared with coeval Expedition 369 sections cored elsewhere in the Mentelle Basin and with other IODP and industry data from the southern and Western Australia margins to correlate recovered lithologies with seismic lines across the Mentelle Basin and to identify regional differences in the geochemical biological responses to OAEs and Cretaceous and Neogene ocean circulation history.

Operations

Four holes were cored at Site U1516 (Table T1). Hole U1516A was cored with the advanced piston corer (APC) and half-length APC (HLAPC) systems to 223.6 m drilling depth below seafloor (DSF). Hole U1516B penetrated ~15 m with the APC system. Hole U1516C was drilled without coring to 196 m DSF and then cored with the rotary core barrel (RCB) system to 541.6 m DSF. Hole U1516D was drilled without coring to 458 m DSF, and then four RCB cores were recovered to 477.6 m DSF for an additional copy of the Cenomanian/Turonian boundary.

In total, 476.99 m was recovered of 605.0 m cored (78.8%). We recovered 206.57 m of 197.5 m cored (104.6%) with the APC system, 43.55 m of 42.3 m cored (103%) with the HLAPC system, and 226.87 m of 365.2 m cored (62.1%) with the RCB system. We spent 5.9 days at Site U1516.

Transit to Site U1516

The ship arrived at Site U1516 at 0148 h (UTC + 11 h) on 14 November 2017 after a transit that covered 100 nmi over 11.9 h (average speed = 8.4 kt).

Hole U1516A

Hole U1516A (34°20.9169'S, 112°47.9553'E) was cored with the APC/extended core barrel (XCB) system. Nonmagnetic drill collars and core barrels were used when possible. Core orientation was performed on all cores recovered with the APC system using the Ice-field MI-5 or FlexIT core orientation tools. Hole U1516A was

started at 1220 h on 14 November 2017 at 2676.5 meters below sea level and recovered a 4.68 m long mudline core (1H). Cores 2H through 20H were then recovered. In situ formation temperature measurements with the advanced piston corer temperature tool (APCT-3) were made while taking Cores 3H, 5H, 7H, and 17H. While coring Core 20H, significant overpull was needed to recover the core barrel. When the core barrel was on the rig floor, we observed a split core liner and flow-in. Therefore, we switched to the HLAPC system. HLAPC coring continued through the recovery of Core 29F to 223.6 m DSF. After recovering Core 29F, piston coring refusal was reached, and coring ended at 1600 h on 15 November. The drill string was brought up and cleared the seafloor at 1725 h, ending Hole U1516A. Overall, 233.26 m was recovered of 223.6 m cored (104.3%), with 189.76 m recovered of 181.3 m cored (104.7%) with the APC system and 43.55 m recovered of 42.3 m cored (103.0%) with the HLAPC system. In total, 1.7 days were spent in Hole U1516A.

Hole U1516B

The vessel was offset 20 m east, and Hole U1516B (34°20.9175'S, 112°47.9684'E) was started at 1905 h on 15 November 2017. Two APC cores were taken to 16.2 m DSF, recovering 16.81 m of material (103.8%). The cores were immediately sectioned into 30 cm whole rounds on the catwalk and placed in light-proof bags; these whole rounds will be analyzed postexpedition for optically stimulated luminescence (OSL). The drill string was then brought to the rig floor at 0345 h on 16 November. The total time spent in this hole was 0.4 days.

Hole U1516C

The vessel was offset 20 m south, and preparations were made for drilling/coring with the RCB system. Hole U1516C (34°20.9272'S, 112°47.9711'E) was started at 1240 h on 16 November 2017 at 2676.6 m water depth. We drilled without coring to 196 m DSF, after which the center bit was pulled to allow for coring. We recovered Cores 2R through 41R to 541.6 m DSF by 1715 h on 18 November 2017. The drill string was then brought up and cleared the seafloor at 1950 h, ending Hole U1516C. In total, 208.32 m were recovered of 345.6 m cored (60.3%). Overall, 2.7 days were spent in Hole U1516C.

Hole U1516D

The vessel was offset 20 m west, and Hole U1516D (34°20.9277'S, 112°47.9573'E) was started at 2115 h on 18 November 2017. Like Hole U1516C, the water depth was 2676.6 m. We drilled without coring to 458 m DSF. The center bit was pulled, and RCB coring started at 0930 h on 19 November. We recovered Cores 2R through 5R to 477.6 m DSF. The drill string was brought up, clearing the seafloor at 1715 h. The beacon was recovered at 1825 h. The drill string was back on the rig floor at 2255 h, ending Hole U1516D. In total, we recovered 18.55 m of 19.6 m cored (94.6%). Overall, we spent 1.1 days in Hole U1516D.

Table T1. Coring summary, Site U1516. * = sectioned into 30 cm whole rounds on catwalk; all material for postcruise analyses. DRF = drilling depth below rig floor, DSF = drilling depth below seafloor, APC_CALC = drill string length from rig floor to the bit, plus the length of the extended advanced piston corer (APC) core barrel minus the length of core recovered, OFFSET = seafloor depth is adopted from the previous hole, NA = not applicable. Core type: H = APC, F = half-length APC (HLAPC), X = extended core barrel (XCB), R = rotary core barrel (RCB), numeric core type = drilled interval. (Continued on next page.) [Download table in CSV format.](#)

Hole U1516A						Hole U1516B					
Latitude: 34°20.9169'S						Latitude: 34°20.9175'S					
Longitude: 112°47.9553'E						Longitude: 112°47.9684'E					
Water depth (m): 2676.46						Water depth (m): 2676.42					
Date started UTC (h): 13 Nov 2017 1748						Date started UTC (h): 15 Nov 2017 0925					
Date finished UTC (h): 15 Nov 2017 0925						Date finished UTC (h): 15 Nov 2017 1945					
Time on hole (days): 1.65						Time on hole (days): 0.43					
Seafloor depth DRF (m): 2687.8						Seafloor depth DRF (m): 2687.8					
Seafloor depth estimation method: APC_CALC						Seafloor depth estimation method: APC_CALC					
Rig floor to sea level (m): 11.34						Rig floor to sea level (m): 11.38					
Penetration DSF (m): 223.6						Penetration DSF (m): 16.2					
Cored interval (m): 223.6						Cored interval (m): 16.2					
Recovered length (m): 233.26						Recovered length (m): 16.81					
Recovery (%): 104.32						Recovery (%): 103.77					
Drilled interval (m): NA						Drilled interval (m): NA					
Total cores (no.): 29						Total cores (no.): 2					
APC cores (no.): 20						APC cores (no.): 2					
HLAPC cores (no.): 9											
Hole U1516C						Hole U1516D					
Latitude: 34°20.9272'S						Latitude: 34°20.9277'S					
Longitude: 112°47.9711'E						Longitude: 112°47.9573'E					
Water depth (m): 2676.62						Water depth (m): 2676.62					
Date started UTC (h): 15 Nov 2017 1945						Date started UTC (h): 18 Nov 2017 1150					
Date finished UTC (h): 18 Nov 2017 1150						Date finished UTC (h): 19 Nov 2017 1455					
Time on hole (days): 2.67						Time on hole (days): 1.13					
Seafloor depth DRF (m): 2688						Seafloor depth DRF (m): 2688					
Seafloor depth est. method: OFFSET						Seafloor depth estimation method: OFFSET					
Rig floor to sea level (m): 11.38						Rig floor to sea level (m): 11.38					
Penetration DSF (m): 541.6						Penetration DSF (m): 477.6					
Cored interval (m): 345.6						Cored interval (m): 19.6					
Recovered length (m): 208.32						Recovered length (m): 18.55					
Recovery (%): 60.28						Recovery (%): 94.64					
Drilled interval (m): 196						Drilled interval (m): 458					
Drilled interval (no.): 1						Drilled interval (no.): 1					
Total cores (no.): 40						Total cores (no.): 4					
RCB cores (no.): 40						RCB cores (no.): 4					

Core	Top depth drilled DSF (m)	Bottom depth drilled DSF (m)	Advanced (m)	Recovered length (m)	Curated length (m)	Top depth cored CSF (m)	Bottom depth recovered (m)	Recovery (%)	Time on deck UTC (h)	Sections (N)
369-U1516A-										
1H	0.0	4.7	4.7	4.68	4.68	0.0	4.68	100	14 Nov 2017 0440	4
2H	4.7	14.2	9.5	9.92	9.92	4.7	14.62	104	14 Nov 2017 0555	8
3H	14.2	23.7	9.5	10.07	10.07	14.2	24.27	106	14 Nov 2017 0700	8
4H	23.7	33.2	9.5	9.88	9.88	23.7	33.58	104	14 Nov 2017 0755	8
5H	33.2	42.7	9.5	9.89	9.89	33.2	43.09	104	14 Nov 2017 0900	8
6H	42.7	52.2	9.5	9.94	9.94	42.7	52.64	105	14 Nov 2017 0955	8
7H	52.2	61.7	9.5	9.99	9.99	52.2	62.19	105	14 Nov 2017 1105	8
8H	61.7	71.2	9.5	9.92	9.93	61.7	71.63	104	14 Nov 2017 1205	8
9H	71.2	80.7	9.5	9.72	9.72	71.2	80.92	102	14 Nov 2017 1300	8
10H	80.7	90.2	9.5	10.07	10.07	80.7	90.77	106	14 Nov 2017 1355	8
11H	90.2	99.7	9.5	10.05	10.05	90.2	100.25	106	14 Nov 2017 1455	8
12H	99.7	109.2	9.5	9.96	9.96	99.7	109.66	105	14 Nov 2017 1555	8
13H	109.2	118.7	9.5	9.96	9.96	109.2	119.16	105	14 Nov 2017 1655	8
14H	118.7	128.2	9.5	10.08	10.08	118.7	128.78	106	14 Nov 2017 1750	8
15H	128.2	137.7	9.5	9.88	9.88	128.2	138.08	104	14 Nov 2017 1840	8
16H	137.7	147.2	9.5	10.03	10.03	137.7	147.73	106	14 Nov 2017 1935	8
17H	147.2	156.7	9.5	10.30	10.30	147.2	157.50	108	14 Nov 2017 2035	8
18H	156.7	166.2	9.5	9.76	9.76	156.7	166.46	103	14 Nov 2017 2125	8
19H	166.2	175.7	9.5	10.01	10.01	166.2	176.21	105	14 Nov 2017 2225	8
20H	175.7	181.3	5.6	5.65	5.65	175.7	181.35	101	14 Nov 2017 2315	6
21F	181.3	186.0	4.7	5.00	5.00	181.3	186.30	106	15 Nov 2017 0025	5
22F	186.0	190.7	4.7	5.04	5.04	186.0	191.04	107	15 Nov 2017 0115	5
23F	190.7	195.4	4.7	4.82	4.82	190.7	195.52	103	15 Nov 2017 0200	5
24F	195.4	200.1	4.7	3.84	4.74	195.4	200.14	82	15 Nov 2017 0240	5

Table T1 (continued).

Core	Top depth drilled DSF (m)	Bottom depth drilled DSF (m)	Advanced (m)	Recovered length (m)	Curated length (m)	Top depth cored CSF (m)	Bottom depth recovered (m)	Recovery (%)	Time on deck UTC (h)	Sections (N)
25F	200.1	204.8	4.7	5.01	5.01	200.1	205.11	107	15 Nov 2017 0320	5
26F	204.8	209.5	4.7	5.00	5.00	204.8	209.80	106	15 Nov 2017 0405	5
27F	209.5	214.2	4.7	4.95	4.95	209.5	214.45	105	15 Nov 2017 0455	5
28F	214.2	218.9	4.7	5.02	5.02	214.2	219.27	107	15 Nov 2017 0540	5
29F	218.9	223.6	4.7	4.82	4.82	218.9	223.72	103	15 Nov 2017 0710	5
Hole U1516A totals:			223.6	233.26	234.17					199
369-U1516B-										
1H*	0.0	6.70	6.7	6.77	6.77	0.0	6.77	101	15 Nov 2017 1125	6
2H*	6.7	16.20	9.5	10.04	10.04	6.7	16.74	106	15 Nov 2017 1220	8
Hole U1516B totals:			16.2	16.81	16.81					14
369-U1516C-										
11	0.0	196.00	196.0			****Drilled interval****			16 Nov 2017 0920	0
2R	196.0	205.6	9.6	0.04	0.04	196.0	196.04	0	16 Nov 2017 1020	1
3R	205.6	215.2	9.6	2.52	2.52	205.6	208.12	26	16 Nov 2017 1115	3
4R	215.2	224.8	9.6	1.80	1.80	215.2	217.00	19	16 Nov 2017 1205	3
5R	224.8	234.4	9.6	1.09	1.09	224.8	225.89	11	16 Nov 2017 1305	2
6R	234.4	244.0	9.6	0.07	0.07	234.4	234.47	1	16 Nov 2017 1400	1
7R	244.0	253.6	9.6	4.01	4.01	244.0	248.01	42	16 Nov 2017 1450	5
8R	253.6	263.2	9.6	8.77	8.77	253.6	262.37	91	16 Nov 2017 1540	8
9R	263.2	272.8	9.6	9.50	9.50	263.2	272.70	99	16 Nov 2017 1630	8
10R	272.8	282.4	9.6	6.27	6.27	272.8	279.07	65	16 Nov 2017 1715	6
11R	282.4	292.0	9.6	2.79	2.79	282.4	285.19	29	16 Nov 2017 1755	3
12R	292.0	301.6	9.6	5.10	5.10	292.0	297.10	53	16 Nov 2017 1845	5
13R	301.6	311.2	9.6	3.02	3.02	301.6	304.62	31	16 Nov 2017 1930	3
14R	311.2	320.8	9.6	0.05	0.05	311.2	311.25	1	16 Nov 2017 2020	1
15R	320.8	330.4	9.6	6.59	6.59	320.8	327.39	69	16 Nov 2017 2105	6
16R	330.4	340.0	9.6	3.40	3.40	330.4	333.80	35	16 Nov 2017 2155	4
17R	340.0	349.6	9.6	8.89	8.89	340.0	348.89	93	16 Nov 2017 2240	8
18R	349.6	359.2	9.6	8.07	8.07	349.6	357.67	84	16 Nov 2017 2330	7
19R	359.2	368.8	9.6	8.56	8.56	359.2	367.76	89	17 Nov 2017 0015	7
20R	368.8	378.4	9.6	1.21	1.21	368.8	370.01	13	17 Nov 2017 0100	2
21R	378.4	388.0	9.6	8.15	8.15	378.4	386.55	85	17 Nov 2017 0145	7
22R	388.0	397.6	9.6	2.56	2.56	388.0	390.56	27	17 Nov 2017 0240	4
23R	397.6	407.2	9.6	5.83	5.83	397.6	403.43	61	17 Nov 2017 0420	6
24R	407.2	416.8	9.6	9.93	9.93	407.2	417.13	103	17 Nov 2017 0605	9
25R	416.8	426.4	9.6	7.95	7.95	416.8	424.75	83	17 Nov 2017 0810	8
26R	426.4	436.0	9.6	8.36	8.36	426.4	434.76	87	17 Nov 2017 1010	7
27R	436.0	445.6	9.6	6.62	6.62	436.0	442.62	69	17 Nov 2017 1205	6
28R	445.6	455.2	9.6	8.85	8.85	445.6	454.45	92	17 Nov 2017 1400	7
29R	455.2	460.0	4.8	3.91	3.91	455.2	459.11	81	17 Nov 2017 1535	5
30R	460.0	464.8	4.8	5.33	5.33	460.0	465.33	111	17 Nov 2017 1655	5
31R	464.8	469.6	4.8	5.12	5.12	464.8	469.92	107	17 Nov 2017 1830	5
32R	469.6	474.4	4.8	4.22	4.22	469.6	473.82	88	17 Nov 2017 1950	4
33R	474.4	479.2	4.8	5.61	5.61	474.4	480.01	117	17 Nov 2017 2110	6
34R	479.2	484.0	4.8	4.49	4.55	479.2	483.75	94	17 Nov 2017 2230	5
35R	484.0	488.8	4.8	4.60	4.69	484.0	488.69	96	17 Nov 2017 2350	5
36R	488.8	493.6	4.8	4.83	4.90	488.8	493.70	101	18 Nov 2017 0110	5
37R	493.6	503.2	9.6	4.38	4.43	493.6	498.03	46	18 Nov 2017 0240	4
38R	503.2	512.8	9.6	6.57	6.57	503.2	509.77	68	18 Nov 2017 0415	7
39R	512.8	522.4	9.6	1.88	1.88	512.8	514.68	20	18 Nov 2017 0600	3
40R	522.4	532.0	9.6	9.35	9.45	522.4	531.85	97	18 Nov 2017 0735	8
41R	532.0	541.6	9.6	8.03	8.10	532.0	540.10	84	18 Nov 2017 0910	7
Hole U1516C totals:			345.6	208.32	208.76					206
369-U1516D-										
11	0.0	458.0	458.0			****Drilled interval****			19 Nov 2017 0135	0
2R	458.0	462.5	4.5	4.02	4.02	458.0	462.02	89	19 Nov 2017 0300	5
3R	462.5	467.0	4.5	3.99	3.99	462.5	466.49	89	19 Nov 2017 0430	4
4R	467.0	473.0	6.0	5.94	5.94	467.0	472.94	99	19 Nov 2017 0600	6
5R	473.0	477.6	4.6	4.60	4.60	473.0	477.60	100	19 Nov 2017 0730	4
Hole U1516D totals:			19.6	18.55	18.55					19
Site U1516 totals:			605.0	476.94	478.29					438

Lithostratigraphy

The sedimentary sequence recovered at Site U1516 is divided into four main lithostratigraphic units, and Unit I is divided into three subunits (Figure F3; Table T2). The cores from Hole U1516B are dedicated for future OSL measurements and were immediately preserved upon recovery and not described onboard (see **Operations**). Lithostratigraphic units and boundaries are defined by changes in lithology and sedimentary characteristics as identified by

macroscopic core description (Figure F4), smear slide examination (Figures F5, F6; see Site U1516 smear slides in **Core descriptions**), X-ray diffraction (XRD) (Figure F5) and handheld portable X-ray fluorescence (pXRF) (Table T3) measurements. Unit I is a Pleistocene to Paleocene sequence of white, pinkish gray, and gray calcareous/foraminiferal/nannofossil ooze/chalk and pale yellow to grayish green nannofossil-rich claystone (sometimes with chert) and claystone. A lithologic contact and a shift to higher natural gamma radiation (NGR) values (see **Petrophysics**) in Section 369-U1516C-8R-4

Figure F3. Lithostratigraphic summary, Site U1516.

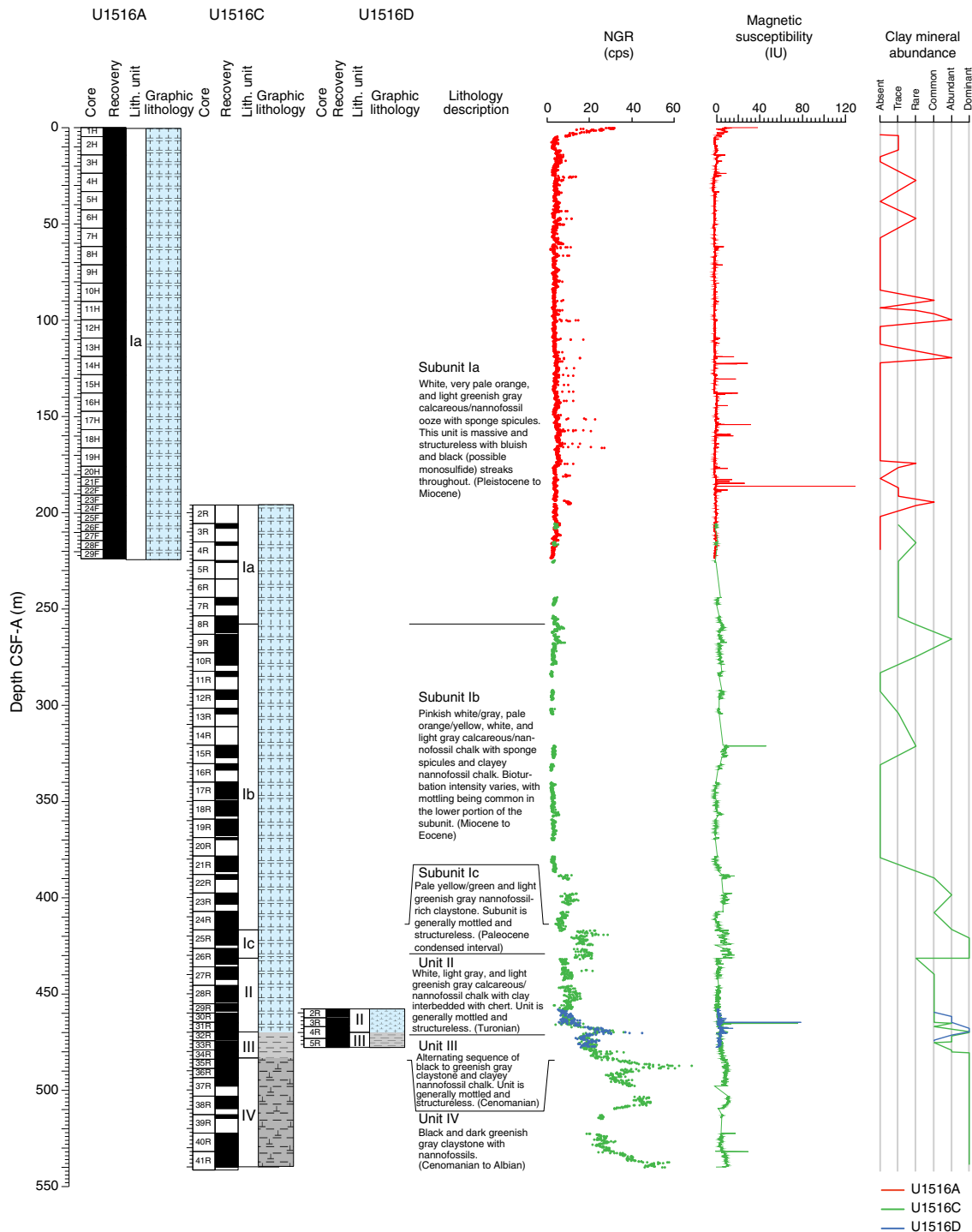


Table T2. Lithostratigraphic units, Site U1516. TOH = top of hole, BOH = bottom of hole. [Download table in CSV format.](#)

Unit	Subunit	Core, section	Depth in Hole U1516A CSF-A (m)	Core, section, interval (cm)	Depth in Hole U1516C CSF-A (m)	Core, section, interval (cm)	Depth in Hole U1516D CSF-A (m)
		369-U1516A-		369-U1516C-		369-U1516D-	
I	la	(TOH) 1H-1 to 29F-CC	0.00–223.72	2R-1, 0, to 8R-4, 58	196.00–257.86		
	lb			8R-4, 59, to 24R-CC, 18	257.87–417.08		
	lc			25R-1, 0, to 24R-4, 106	416.80–431.56		
II				26R-4, 106, to 31R-4, 119	431.54–469.85	2R-1, 0, to 4R-3, 48	458.00–469.91
III				31R-4, 119, to 33R-CC	469.85–479.96	4R-3, 48, to 5R-CC, 24 (BOH)	469.91–477.60
IV				34R-1, 0, to 41R-CC (BOH)	479.20–540.10		

Unit	Subunit	Lithology	Age
I	la	White to light greenish gray calcareous/nannofossil ooze with sponge spicules; massive and structureless	Pleistocene to Miocene
	lb	Pinkish white/gray and very pale orange calcareous/nannofossil chalk with sponge spicules; massive, mottled, and structureless	Miocene to Eocene
	lc	Pale yellow and light greenish gray nannofossil-rich claystone (sometimes with chert) and claystone; mottled and structureless with intense bioturbation	Paleocene (condensed interval)
II		Light greenish gray and greenish gray nannofossil chalk with clay; massive and structureless	Turonian
III		Alternating black/light greenish gray/greenish gray/very dark greenish gray claystone (sometimes with nannofossils) and clayey nannofossil chalk; massive, mottled or laminated	Cenomanian
IV		Black and dark greenish gray nannofossil-rich claystone and claystone with nannofossils; some subtle color alternations (black to dark greenish gray) throughout; mottled or massive	Cenomanian to Albian

(257.86 m core depth below seafloor, Method A [CSF-A]) defines the boundary between Subunits Ia and Ib. Subunit Ic, which is also characterized by a shift in NGR and magnetic susceptibility (416.80–431.56 m CSF-A), is likely to be a condensed interval (see [Biostratigraphy and micropaleontology](#)). Poor recovery at the top of Hole U1516C (Cores 2R through 5R) hinders correlation of the bottom of Hole U1516A to the top of Hole U1516C (see [Stratigraphic correlation](#)). Because no anchored stratigraphic splice is provided for Site U1516, the true thickness of Unit I cannot be determined. Unit II is a 38.29 m thick Turonian sequence of white, light olive-brown, and light gray calcareous chalk interbedded with chert that gradually transitions into light greenish gray and greenish gray nannofossil chalk with clay interbedded with chert. Unit III is a 10.11 m thick Cenomanian sequence of claystone with nannofossils, nannofossil-rich claystone, and clayey nannofossil chalk that regularly alternates in color. Unit IV is a 60.90 m thick Cenomanian to Albian sequence of black and dark greenish gray claystone that is sometimes nannofossil rich.

Unit I

Intervals: 369-U1516A-1H-1, 0 cm (top of hole [TOH]), through 29F-CC (bottom of hole [BOH]); 369-U1516C-3R-1, 0 cm, to 26R-4, 105 cm

Depths: Hole U1516A = 0–223.72 m CSF-A; Hole U1516C = 205.60–431.56 m CSF-A

Age: Pleistocene to Paleocene

Lithology: calcareous ooze with sponge spicules, foraminiferal ooze with sponge spicules, nannofossil ooze with sponge spicules, silty calcareous ooze and silty calcareous ooze with sponge spicules, sponge spicule-rich calcareous ooze with clay, and calcareous chalk with sponge spicules

Drilling disturbance type and intensity: various (soupy, bowed, and punctured); none to severe

Nature of top contact: seafloor

Nature of bottom contact: sharp

Lithostratigraphic Unit I is dominated by calcareous/foraminiferal/nannofossil ooze with sponge spicules, silty calcareous ooze with common to dominant sponge spicules, sponge spicule-rich calcareous ooze with clay, and calcareous chalk with common to abundant sponge spicules (Figures [F3](#), [F4A–F4C](#); see Site U1516 smear slides in [Core descriptions](#)). This unit is massively bedded or mottled and structureless.

In smear slides, the biogenic components largely consist of rare to dominant calcareous nannofossils and foraminifers, rare to abundant sponge spicules, and trace to rare radiolarians. A notable feature of Unit I is the poor preservation of the siliceous sponge spicules from Section 369-U1516A-14H-1 to and from Core 369-U1516C-3R through at least Section 20R-CC. The sponge spicules commonly have small holes (Figure [F6](#)). In smear slides, siliciclastic grains are either absent or consist of trace to common quartz, feldspar, clay, opaque grains (including pyrite and possible monosulfides), and glauconite with occasional trace zircon and chlorite. Allogenic carbonate grains are also present in trace amounts. Unit I is divided into Subunit Ia (nannofossil ooze); Subunit Ib (nannofossil chalk), which is more indurated; and Subunit Ic (nannofossil-rich claystone) (Figures [F3](#), [F4A–F4C](#)).

Subunit Ia

Intervals: 369-U1516A-1H-1, 0 cm (TOH), through 29F-CC (BOH); 369-U1516C-3R-1, 0 cm (TOH), to 8R-4, 58 cm

Depths: Hole U1516A = 0–223.72 m CSF-A; Hole U1516C = 205.60–257.86 m CSF-A

Age: Pleistocene to Miocene

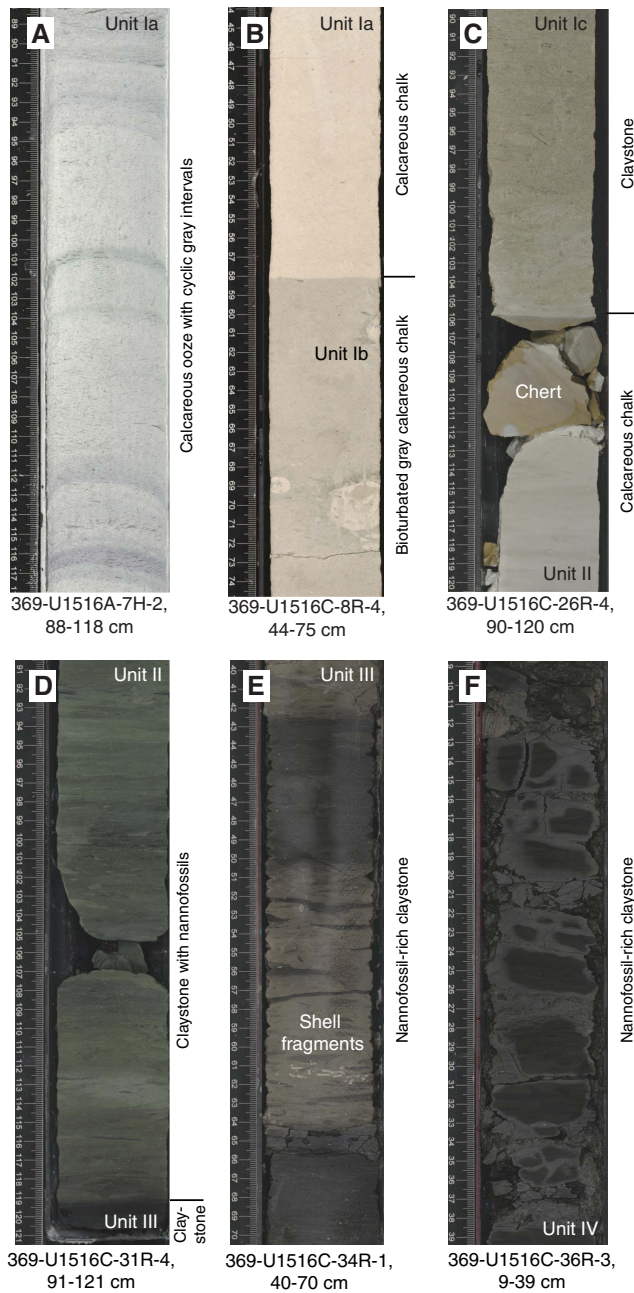
Lithology: calcareous ooze with sponge spicules, nannofossil ooze with sponge spicules, silty calcareous ooze, silty calcareous ooze with common sponge spicules, and sponge spicule-rich calcareous ooze with clay

Drilling disturbance type and intensity: various (soupy, bowed, and punctured); none to severe

Nature of top contact: seafloor

Nature of bottom contact: lithologic

Figure F4. Lithologies and unit boundaries, Site U1516. A. Subunit Ia. B. Subunit Ia/Ib boundary. C. Subunit Ic/Unit II boundary. D. Unit II/III boundary. E. Unit III with shell fragments. F. Unit IV boundary.



Lithostratigraphic Subunit Ia consists of white to light greenish gray calcareous/nannofossil ooze with sponge spicules, sponge spicule-rich calcareous ooze, silty calcareous ooze (sometimes with common sponge spicules), and sponge spicule-rich calcareous ooze with clay (Figures F3, F4A, F4B; Table T2). This unit is massive and structureless. Overall, bioturbation is absent. In Sections 369-U1516A-1H-1 through 13H-CC, this subunit largely consists of ooze made up of foraminifers. In contrast, from Section 14H-1 to the bottom of the hole and from Core 369-U1516C-3R through Section 8R-4, trace to rare occurrences of clay minerals were observed. The boundary between Subunits Ia and Ib is defined by a lithologic contact in Section 8R-4 (257.86 m CSF-A; Figure F4B).

Figure F5. Sediment constituents in Units I–IV, Holes U1516A and U1516C. A. Calcareous ooze with sponge spicules (plane-polarized light [PPL]). B–D. Nannofossil chalk with (B) sponge spicules (cross-polarized light [XPL]) and clay; (C) PPL, (D) XPL. E. Clayey nannofossil chalk (XPL). F. Claystone with nannofossils (PPL).

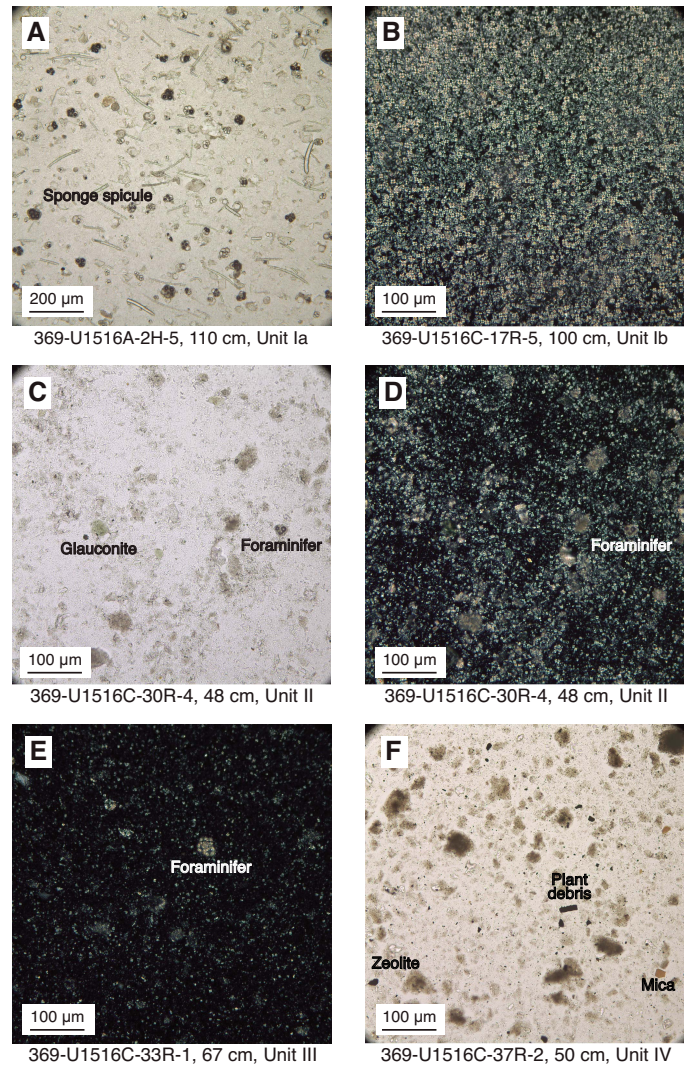


Figure F6. Siliceous sponge spicules with holes, Hole U1516C. A. Smear slide photomicrograph. B. Scanning electron micrograph (SEM) from siliceous fraction (sample was acidified to remove carbonate).

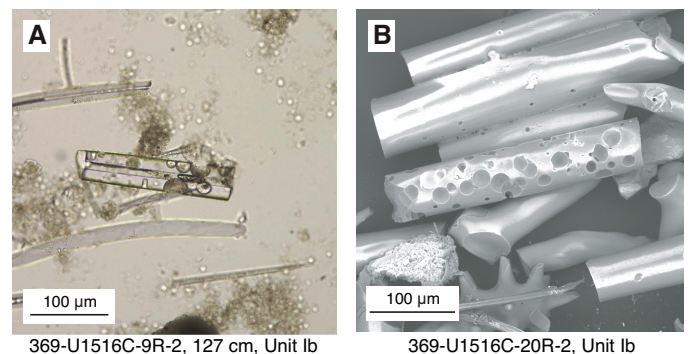


Table T3. X-ray diffraction results, Site U1516. [Download table in CSV format.](#)

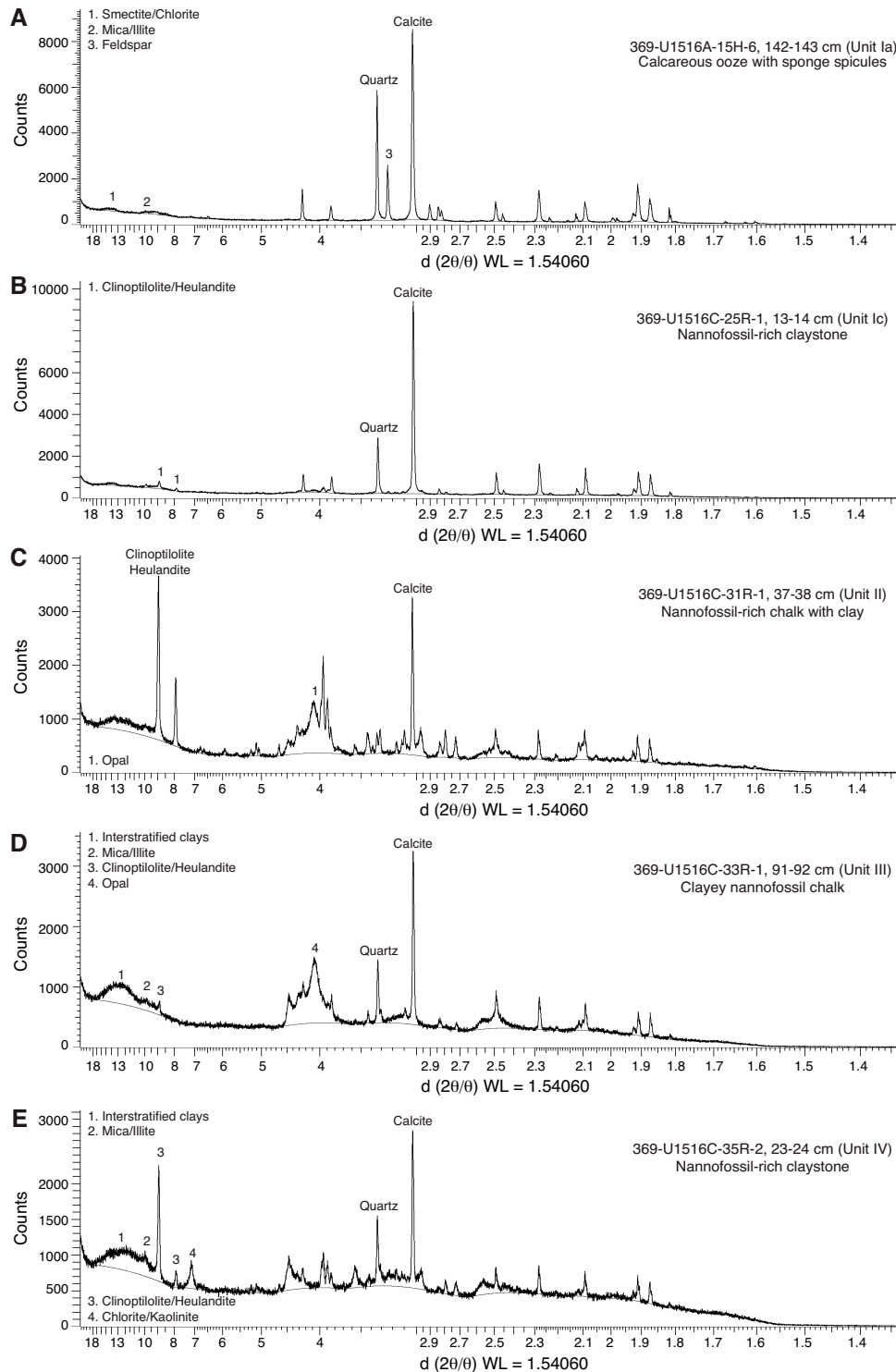
This boundary is also marked by a shift to higher NGR and bulk density and a decrease in L^* (Figure F3; see **Petrophysics**), reflecting a shift from the white ooze/chalk to the darker chalk.

In smear slides, biogenic grains largely comprise rare to dominant nannofossils and foraminifers, rare to abundant sponge spicules, and trace to rare radiolarians (Figure F5A; see Site U1516 smear slides in **Core descriptions**). Siliciclastic grains consist of trace to abundant clay, trace to common glauconite, trace to rare

quartz, and occasional trace to rare feldspar. Opaque minerals are present throughout the subunit (trace to abundant) and consist of pyrite and possible monosulfides. Several silty intervals occur throughout this subunit, some of which contain zircon grains (Sections 369-U1516A-6H-3, 14H-1, 18H-5, and 27F-2).

XRD analyses confirm that calcite is the dominant mineral in Subunit Ia (Figure F7A). Other minerals present in trace amounts include quartz, halite, chlorite/kaolinite, illite/mica, montmorillonite,

Figure F7. A–E. XRD results, Site U1516.



and possible interstratified clay. In silty intervals, however, quartz and feldspars are more abundant. This composition is consistent with >84 wt% carbonate content (see **Geochemistry**) and >37 wt% Ca content (except in silty intervals) (Table **T3**).

Subunit Ib

Interval: 369-U1516C-8R-4, 58 cm, to 25R-1, 0 cm

Depth: Hole U1516C = 257.86–416.80 m CSF-A

Age: Miocene to Eocene

Lithology: sponge spicule–rich calcareous chalk, calcareous chalk with sponge spicules, nannofossil chalk, nannofossil chalk with sponge spicules, sponge spicule–rich nannofossil chalk with clay, clayey nannofossil chalk and clayey calcareous chalk.

Drilling disturbance type and intensity: various (fractured, soupy, biscuited, brecciated, and void); none to severe

Nature of top contact: lithologic

Nature of bottom contact: not observed (core gap)

Lithostratigraphic Subunit Ib is a 158.94 m thick sequence of pinkish white, pinkish gray, and very pale orange sponge spicule–rich calcareous chalk, calcareous chalk with sponge spicules, nannofossil chalk (sometimes with sponge spicules), sponge spicule–rich nannofossil chalk with clay, and clayey nannofossil/calcareous chalk (Figures **F3**, **F4B**). Bioturbation intensity in this subunit ranges from absent to intense with discrete *Zoophycos*, *Chondrites*, and *Planolites* ichnofacies. Large *Cylindrichnus* burrows (as much as 9 cm in diameter) representing multiple phases of burrowing are present in this subunit (Cores 369-U1516C-8R through 12R). Occasional chert nodules are present in Cores 22R and 23R. Placement of the Subunit Ib/Ic boundary is supported by a shift in NGR and magnetic susceptibility (Figure **F3**; see **Petrophysics**).

In smear slides, biogenic constituents largely consist of abundant to dominant calcareous nannofossils, trace to common foraminifers, and absent to rare radiolarians (Figure **F5B**; see Site U1516 smear slides in **Core descriptions**). Sponge spicules are common to abundant throughout this subunit but are rare in Cores 369-U1516C-19R through 23R. The siliciclastic fraction is composed of absent to abundant clay, trace to rare quartz, glauconite and opaque grains (including pyrite and monosulfides), and occasional trace feldspar and mica.

XRD analyses show that Subunit Ib is dominated by calcite (Figure **F7A**). Other minerals present in trace amounts in this subunit are quartz, halite, chlorite/kaolinite, montmorillonite, and clinoptilolite/heulandite, which is consistent with >35% Ca content measured by pXRF (Table **T3**).

Subunit Ic

Interval: 369-U1516C-25R-1, 0 cm, to 26R-4, 105 cm

Depth: Hole U1516C = 416.80–431.56 m CSF-A

Age: Paleocene

Lithology: nannofossil-rich claystone, nannofossil-rich claystone with chert and claystone

Drilling disturbance type and intensity: fractured; slight to moderate

Nature of top contact: not observed (core gap)

Nature of bottom contact: sharp

Lithostratigraphic Subunit Ic is a 14.76 m thick pale yellow, pale green, light greenish gray, and grayish green sequence of claystone that is commonly nannofossil rich and contains several intervals

with abundant chert (Figure **F3**). This subunit is massive and structureless. Most of the interval is mottled due to intense bioturbation, and *Zoophycos* burrows are common in Sections 369-U1516C-26R-2 through 26R-4. Subunit Ic is likely a condensed interval (see **Biostratigraphy and micropaleontology**) characterized by greater induration, intense bioturbation, and more quartz and feldspar than adjacent units.

Smear slide observation data from Subunit Ic is limited because the sediments were too indurated to scrape. The two smear slides for this subunit suggest that rare to common nannofossils are the only biogenic components. The siliciclastic components include dominant clay, common quartz and feldspar, common authigenic carbonate, rare to common glauconite, rare mica, and trace opaques (Table **T3**).

XRD analysis of one sample from Subunit Ic indicates that the mineral assemblage is mainly composed of calcite and quartz (Figure **F7B**). Clinoptilolite/heulandite are present in trace amounts. Bulk-rock pXRF analysis of the single sample in this subunit (Sample 369-U1516C-25R-4, 17–18 cm) reveals higher contents of Si (13 wt%), K (0.45 wt%), and Fe (1.7 wt%) than those in Subunits Ia and Ib (Table **T3**).

Unit II

Intervals: 369-U1516C-26R-4, 105 cm, to 31R-4, 119 cm; 369-U1516D-2R-1, 0 cm, to 4R-3, 31 cm

Depths: Hole U1516C = 431.56–469.85 m CSF-A; Hole U1516D = 458.00–469.74 m CSF-A

Age: Turonian

Lithology: calcareous chalk, nannofossil chalk with clay, clayey nannofossil chalk, claystone with nannofossils, claystone and chert

Drilling disturbance type and intensity: various (fractured and fragmented); none to severe

Nature of top contact: sharp

Nature of bottom contact: sharp

Lithostratigraphic Unit II is a 38.29 m thick sequence of white, light olive brown, and light gray calcareous chalk interbedded with chert that gradually transitions into light greenish gray and greenish gray calcareous/nannofossil chalk with clay interbedded with chert and then into claystone at the bottom of the unit (Figures **F3**, **F4C**, **F4D**; Table **T2**). This unit is generally massive and structureless and contains some mottled intervals. Bioturbation intensity ranges from absent to intense. Trace and common occurrences of shell fragments, including those of inoceramid bivalves, occur throughout.

The top of Unit II (Section 369-U1516C-26R-4, 105 cm) is defined by an unconformity between the Paleocene and Turonian indicated by changes in the foraminiferal and nannofossil assemblages (see **Biostratigraphy and micropaleontology**) and a decrease in NGR and magnetic susceptibility (Figure **F3**; see **Petrophysics**). The light greenish gray interval begins in Core 29R, extends through the bottom of Unit II, and is characterized by 10–20 cm thick, slightly darker greenish gray intervals. Compared with Unit I, Unit II is characterized by lower abundances of sponge spicules and the presence of discrete chert layers and nodules. This unit meets the underlying Unit III with a sharp contact at 469.85 m CSF-A in Section 31R-4 (Figure **F4D**).

Smear slides indicate that the biogenic fraction in Unit II is composed of rare to dominant calcareous nannofossils and rare to common foraminifers. Siliciclastic components comprise rare to dominant clay, trace to rare feldspar, trace quartz, and occasional

trace glauconite (Figure F5C, F5D; see Site U1516 smear slides in **Core descriptions**). The mineral assemblage is dominated by calcite for most of the discrete samples, but XRD analyses reveals the presence of opal in most samples and an increase of clinoptilolite/heulandite abundance (Figure F7C). Quartz is present in variable proportions. Clay minerals (interstratified clay, montmorillonite, illite/mica, and chlorite/kaolinite) are absent or present in trace abundances. Bulk-rock pXRF analyses reveal that chemical compositions vary widely in Unit II (e.g., 0.66–3.4 wt% Al, 11–48 wt% Si, 10–34 wt% Ca, and 0.53–2.5 wt% Fe) (Table T3).

Unit III

Intervals: 369-U1516C-31R-4, 119 cm, to 33R-CC, 22 cm;
369-U1516D-4R-3, 31 cm, to 5R-CC, 24 cm (BOH)
Depths: Hole U1516C = 469.85–479.96 m CSF-A; Hole U1516D
= 469.74–477.60 m CSF-A
Age: Cenomanian
Lithology: claystone, claystone with nannofossils, nannofossil-rich claystone, and clayey nannofossil chalk
Drilling disturbance type and intensity: various (biscuited, fractured, fragmented, and brecciated); none to moderate
Nature of top contact: sharp
Nature of bottom contact: gradational

Lithostratigraphic Unit III is a 10.11 m thick alternating sequence of black, light greenish gray, greenish gray, and very dark greenish gray claystone (sometimes with common to abundant nannofossils) and clayey nannofossil chalk. Parallel lamination is present in interval 369-U1516C-32R-1, 52–74 cm; the remainder of the unit is either massive or mottled (Figure F4D, F4F). Bioturbation intensity ranges from sparse to low with occasional discrete burrows and shell fragments in Cores 369-U1516C-33R through 34R and 369-U1516D-5R (Figure F4E).

The top of this unit is marked by a distinct 2 cm thick black laminated claystone bed (Sections 369-U1516C-31R-4, 119 cm, and 369-U1516D-4R-3, 31 cm) that approximates the Cenomanian/Turonian boundary (Figures F3, F4D; see **Biostratigraphy and micropaleontology**). The upper Cenomanian in Holes U1516C and U1516D includes four discrete, 2–13 cm thick black claystone intervals. Microfossils in these black intervals are either absent or in trace amounts, although organic matter content varies. Bioturbation in these intervals also varies from laminated to mottled. A notable characteristic of Unit III is the regular color alternation of the claystone (black, dark greenish gray, and greenish gray).

Smear slides confirm that the siliciclastic fraction is composed of common to dominant clay, trace to common quartz, and trace to rare mica, feldspar, glauconite, and opaques (including pyrite). The biogenic fraction comprises trace to dominant calcareous nannofossils, rare radiolarians, and trace to rare foraminifers (Figure F5E; see Site U1516 smear slides in **Core descriptions**). XRD analysis of one sample from Unit III indicates that the mineral assemblage is mainly composed of calcite, quartz, and opal. Interstratified clays, mica/illite, and clinoptilolite/heulandite are present (Figure F7D). pXRF measurements show that Sample 369-U1516C-33R-1, 91–92 cm, consists of 3.8 wt% Al, 32 wt% Si, 8.4 wt% Ca, and 2.7 wt% Fe (Table T3).

Unit IV

Interval: 369-U1516C-34R-1, 0 cm, through 41R-CC, 26 cm (BOH)
Depth: 479.20–540.10 m CSF-A

Age: Cenomanian to Albian

Lithology: nannofossil-rich claystone and claystone with nannofossils

Drilling disturbance type and intensity: various (biscuited, fractured, fragmented, and void); none to completely destroyed

Nature of top contact: gradational

Nature of bottom contact: BOH

Lithostratigraphic Unit IV is an at least 60.90 m thick sequence of massive to mottled black and dark greenish gray nannofossil-rich claystone and claystone with nannofossils (Figure F4F; Table T2). Color alternates regularly but subtly throughout this unit from black to dark greenish gray. Bioturbation varies from entirely absent to completely destroyed. Trace to common shell fragments (including inoceramid shell fragments and disseminated prisms) were observed in Cores 369-U1516C-34R (Figure F4F), 40R, and 41R.

The siliciclastic fraction includes trace to common quartz; trace to rare feldspar, glauconite, and opaques (including pyrite); and trace mica and zeolite. The biogenic fraction is composed of trace to abundant calcareous nannofossils, trace to rare foraminifers, and radiolarians. Smear slides also show an elevated abundance of organic matter relative to the overlying intervals, with plant debris and other organic matter occurring in trace to common abundance throughout the interval (Figure F5F; see Site U1516 smear slides in **Core descriptions**). XRD analyses show that the mineral assemblage is variable in Unit IV. The main minerals are calcite, quartz, clinoptilolite/heulandite, opal, interstratified clays, illite/mica, and chlorite/kaolinite (Figure F7E). Bulk-rock pXRF analyses reveal higher contents of Al (4.8–9.1 wt%), K (0.67–1.6 wt%), and Fe (3.5–6.2) in Unit IV compared with those in Units I–III (Table T3).

Biostratigraphy and micropaleontology

Samples from core catchers and samples taken from split cores at Site U1516 were analyzed for calcareous nannofossils, planktonic foraminifers, and benthic foraminifers. The presence of planktonic and benthic foraminifers, calcareous nannofossils, fish debris, sponge spicules, ostracods, and the mineral glauconite is documented in Table T4. Calcareous nannofossils are abundant to common throughout the section, with barren samples only in the middle Albian and within the Cenomanian/Turonian boundary interval. Preservation is generally good to moderate, with poor preservation associated only with a condensed Paleocene sequence. Reworking of Paleogene taxa into the Neogene assemblages is common. Preservation of planktonic foraminifers is generally good at Site U1516, and some samples in the upper Albian are ranked as excellent. Abundance is more variable; the Neogene, Paleogene, and Turonian generally contain abundant planktonic foraminifers, whereas the Albian contains only rare specimens. Benthic foraminiferal abundance and preservation are also variable. In general, examination of benthic foraminifers indicates a bathyal paleodepth during the Albian through Cenozoic.

Calcareous nannofossil and foraminiferal datums and depths form the chronologic framework at Site U1516 (Tables T5, T6). Paleomagnetic reversal stratigraphy (Table T14) provides additional temporal control for the biochronology. These data define the age-depth plot for this site (Figure F8), which illustrates the general trend of sediment accumulation.

The Neogene has an average sediment accumulation rate of ~18 m/My from the Pleistocene through the upper Miocene. Much of the middle and lower Miocene are missing at a disconformity

Table T4. Selected microfossil groups and minerals identified in smear slides and the >45 µm sieve size fraction, Site U1516. [Download table in CSV format.](#)

Table T5. Calcareous nannofossil bioevents, Site U1516. Ages are from Gradstein et al. (2012). T = top, B = base. [Download table in CSV format.](#)

Datum	Age (Ma)	Core, section, interval (cm)	Top depth CSF-A (m)	Base depth CSF-A (m)
369-U1516A-				
T <i>Pseudoemiliana lacunosa</i>	0.44	2H-CC, 13–18	4.63	14.57
T <i>Discoaster brouweri</i>	1.93	4H-CC, 0–5	24.22	33.53
T <i>Discoaster pentaradiatus</i>	2.39	7H-CC, 25–30	52.59	62.20
T <i>Discoaster surculus</i>	2.49	8H-CC, 0–5	62.20	71.46
T <i>Discoaster tamalis</i>	2.8	8H-CC, 0–5	62.20	71.46
T <i>Sphenolithus abies</i>	3.54	11H-CC, 17–22	90.72	100.20
T <i>Reticulofenestra pseudumbilica</i>	3.7	11H-CC, 17–22	90.72	100.20
T <i>Amaurolithus primus</i>	4.5	13H-CC, 15–20	109.61	119.11
T <i>Discoaster quinqueramus</i>	5.59	17H-CC, 0–5	147.68	157.45
T <i>Nicklithus amplificus</i>	5.94	17H-CC, 0–5	147.68	157.45
B <i>Nicklithus amplificus</i>	6.91	19H-CC, 16–21	166.41	176.16
B <i>Amaurolithus primus</i>	7.42	20H-CC, 15–20	176.16	181.30
T <i>Discoaster loeblichii</i>	7.53	21F-CC, 16–21	181.30	186.25
B <i>Discoaster quinqueramus</i>	8.12	21F-CC, 16–21	181.30	186.25
T <i>Minylitha convalis</i>	8.68	25F-CC, 18–23	200.09	205.06
B <i>Discoaster loeblichii</i>	8.77	26F-CC, 15–20	205.06	209.75
369-U1516C-				
B <i>Discoaster neohamatus</i>	10.52	4R-CC, 0–9	216.91	225.84
B <i>Reticulofenestra pseudumbilica</i>	12.83	6R-CC, 0–7	234.40	247.95
B <i>Sphenolithus delphix</i>	23.11	9R-CC, 0–5	262.31	272.63
B <i>Sphenolithus delphix</i>	23.21	9R-CC, 0–5	272.63	278.97
T <i>Chiasmolithus altus</i>	25.44	10R-CC, 0–10	272.63	278.97
T <i>Reticulofenestra umbilica</i>	31.35	15R-CC, 0–5	311.20	327.34
T <i>Clausiococcus subdistichus acme</i>	33.43	15R-CC, 0–5	311.20	327.34
T <i>Discoaster saipanensis</i>	34.44	17R-CC, 16–23	333.75	348.84
B <i>Isthmolithus recurvus</i>	36.97	17R-CC, 16–23	348.84	357.62
B <i>Chiasmolithus oamaruensis</i>	38.09	20R-CC, 9–14	369.96	386.50
T <i>Chiasmolithus grandis</i>	37.98	21R-CC, 14–19	369.96	386.50
T <i>Heliolithus kleinpellii</i>	58.8	25R-3, 46–47	417.08	419.09
B <i>Heliolithus kleinpellii</i>	59.54	25R-6, 132–133	423.71	427.05
B <i>Fasciculithus tympaniformis</i>	61.51	26R-3, 0–1	429.06	431.93
B <i>Marthasterites furcatus</i>	90.24	26R-5, 1–2	429.06	431.93
B <i>Eiffellithus eximius</i> (s. Verbeek)	93	27R-CC, 15–20	442.57	449.69
B <i>Quadrum gartnerii</i>	93.55	30R-2, 95–98	462.45	465.28
T <i>Axopodorhabdus biramiculatus</i>	94.2	32R-2, 4–7	465.43	471.14
T <i>Lithraphidites acutus</i>	94.39	32R-CC, 0–5	471.14	473.77
T <i>Gartnerago nanum</i>	94.79	33R-CC, 22–27	473.77	479.96
B <i>Eiffellithus turrisiiffellii</i>	103.13	39R-CC, 8–13	514.63	531.70

with an estimated 8 My hiatus. The lowermost Miocene and uppermost Oligocene are present at this site and are separated from the lower Oligocene by a disconformity with ~4 My missing. The lower Oligocene through middle Eocene has an average accumulation rate of ~8 m/My. This sequence is separated from the Turonian by a condensed interval containing several middle Paleocene biostratigraphic units. The lower Paleocene through upper Turonian is missing at a disconformity with a hiatus of at least 29 My. The middle Turonian through upper Albian has an average sediment accumulation rate of ~8 m/My.

Calcareous nannofossils

Calcareous nannofossils occur throughout the succession drilled at Site U1516, with the exception of a few isolated barren intervals in the mid-Cretaceous. The upper portion of the succession, from the Holocene to the upper Miocene, is described from the Hole U1516A record, whereas the lower part of the succession, from the middle Miocene to the Albian, is described from the Hole

U1516C record. Table T5 contains the calcareous nannofossil datums used to establish the temporal framework and provides data for the sediment rate plot (Figure F8). The distribution of biostratigraphically important calcareous nannofossils appears in Tables T7 and T8.

The calcareous nannofossils in Sample 369-U1516A-1H-CC, 13–18 cm, contain abundant large *Gephyrocapsa* without *Emiliana huxleyi* (as indicated by scanning electron microscope [SEM] examination) or *Pseudoemiliana lacunosa*, indicating middle to upper Pleistocene Zone CN14. Sample 2H-CC, 13–18 cm, is strongly dominated by small *Gephyrocapsa* spp. with frequent *P. lacunosa*, indicating upper Pleistocene Subzone CN14a.

Sample 369-U1516A-3H-CC, 8–13 cm, contains a mixture of lower Neogene species, including *Discoaster quinqueramus*, *Discoaster neohamatus*, *Discoaster tamalis*, *Amaurolithus tricorniculatus*, and *Amaurolithus primus*, and Paleogene species, including *Reticulofenestra umbilica*, *Discoaster saipanensis*, and *Dictyococcites bisectus*, as well as Pliocene to Pleistocene species, including *P. lacunosa* and *Gephyrocapsa* spp. Given the large amount of reworking and probable downhole contamination, determination of the true age is difficult. Planktonic foraminifers indicate a basal Pleistocene age for this sample.

The interval from Sample 369-U1516A-4H-CC, 0–5 cm, through Core 10H contains calcareous nannofossil assemblages from upper Pliocene Zone CN12. The interval from Sample 8H-CC, 0–5 cm, through Core 10H contains *D. tamalis* (Figure F9, Specimen 1) without *Reticulofenestra pseudumbilica*, which is diagnostic for Subzone CN12a. Sample 7H-CC, 0–5 cm, contains *Discoaster brouweri* and *Discoaster pentaradiatus* but lacks *Discoaster surculus* and *D. tamalis*, indicating Subzone CN12c. The interval from Sample 4H-CC, 0–5 cm, through Core 6H contains *D. brouweri* but lacks *D. pentaradiatus*, indicating Subzone CN12d. Frequent reworked specimens from the Paleogene, such as *R. umbilica*, *Chiasmolithus altus*, and *D. bisectus*, occur throughout this zone at this site.

The interval from Sample 369-U1516A-11H-CC, 17–22 cm, through Core 12H contains *R. pseudumbilica* without amaurooliths, indicating lower Pliocene Zone CN11. Sphenoliths are absent from Sample 11H-CC, 17–22 cm, indicating the upper part of Subzone CN11b. The interval from Sample 12H-CC, 16–21 cm, through Core 16H contains *Amaurolithus delicatus*, *Amaurolithus primus*, *Amaurolithus tricorniculatus*, and *Sphenolithus abies* without *D. quinqueramus*, indicating lower Pliocene Zone CN10. Ceratoliths are absent from the Pliocene interval at this site, thus precluding division of Zone CN10. This absence probably reflects a cooler surface-water regime, which is corroborated by the presence of abundant *Reticulofenestra perplexa* through at least part of this interval.

The interval from Sample 369-U1516A-17H-CC, 0–5 cm, through Core 20H contains common *D. quinqueramus* (Figure F9, Specimen 2), indicating upper Miocene Zone CN9. The upper three cores in this succession also contain frequent *Discoaster quintatus*, *A. delicatus*, *A. tricorniculatus*, and *Nicklithus amplificus*, indicating Subzone CN9c. Rare reworked specimens from the Paleogene, including *R. umbilica*, *Zygrhablithus bijugatus*, and *D. saipanensis*, occur throughout this section.

The interval from Sample 369-U1516A-21F-CC, 16–21 cm, through Core 27F contains calcareous nannofossils characteristic of upper Miocene Zone CN8. These species include *D. neohamatus*, *Discoaster mendomobensis*, *Discoaster loeblichii*, *Minylitha convalis* (Figure F9, Specimen 4), and *Triquetrorhabdulus rugosus*. The

Table T6. Planktonic foraminiferal bioevents, Site U1516. Ages are from Gradstein et al. (2012). All depths given are the base of the sample. T = top, B = base.

[Download table in CSV format.](#)

Datum	Age (Ma)	Top core, section	Top depth CSF-A (m)	Base core, section	Base depth CSF-A (m)
		369-U1516A-		369-U1516A-	
T <i>Truncorotalia tosaensis</i>	0.61	1H-CC	4.68	2H-CC	14.62
B <i>Truncorotalia truncatulinoides</i>	1.93	3H-CC	24.27	4H-CC	33.58
T <i>Globigerinoides extremus</i>	1.98	3H-CC	24.27	4H-CC	33.58
T <i>Globoturborotalita woodi</i>	2.3	4H-CC	33.58	5H-CC	43.09
T <i>Globoturborotalita decoraperta</i>	2.75	4H-CC	33.58	5H-CC	43.09
B <i>Truncorotalia tosaensis</i>	3.35	5H-CC	43.09	6H-CC	52.64
T <i>Dentoglobigerina altispira</i>	3.47	8H-CC	71.52	9H-CC	80.92
T <i>Sphaeroidinellopsis seminulina</i>	3.59	11H-CC	100.25	12H-CC	109.66
T <i>Globorotalia plesiotumida</i>	3.77	11H-CC	100.25	12H-CC	109.66
T <i>Globorotalia margaritae</i>	3.85	11H-CC	90.77	12H-CC	100.25
B <i>Globorotalia crassaformis</i> sensu lato	4.31	13H-CC	119.16	14H-CC	128.78
T <i>Globoturborotalita nepenthes</i>	4.37	17H-CC	157.50	18H-CC	166.46
B <i>Globorotalia margaritae</i>	6.08	16H-CC	147.73	17H-CC	157.50
B <i>Globigerinoides conglobatus</i>	6.2	18H-CC	166.46	19H-CC	176.21
B <i>Globorotalia plesiotumida</i>	8.58	28F-CC	219.27	29F-CC	223.72
B <i>Globorotalia cibaensis</i>	9.44	26F-CC	209.80	27F-CC	214.45
		369-U1516C-		369-U1516C-	
B <i>Globorotalia plesiotumida</i>	8.58	3R-CC	208.12	4R-CC	217.00
T <i>Paragloborotalia mayeri</i>	10.46	4R-CC	217.00	5R-CC	225.89
B <i>Globoturborotalita nepenthes</i>	11.63	6R-CC	234.47	7R-CC	248.01
B <i>Globoquadrina dehiscens</i>	22.44	8R-CC	262.37	9R-CC	272.70
T <i>Paragloborotalia opima</i>	26.93	9R-CC	272.70	10R-CC	279.07
T <i>Turborotalia ampliapertura</i>	30.28	10R-CC	279.07	11R-CC	285.19
B <i>Paragloborotalia opima</i>	30.72	11R-CC	285.19	12R-CC	297.10
B common <i>Pseudohastigerina micra</i>	33.89	16R-CC	333.80	17R-CC	348.89
T <i>Globigerinatheka index</i>	34.61	16R-CC	333.80	17R-CC	348.89
T <i>Acarinina primitiva</i>	39.12	20R-CC	370.01	21R-CC	386.55
B <i>Globigerinatheka index</i>	42.64	22R-CC	390.56	24R-CC	417.13
T <i>Guembeltrioides nuttalli</i>	42.07	22R-CC	390.56	24R-CC	417.13
B <i>Ticinella primula</i>	101.51	40R-CC	531.85	41R-CC	540.10

Figure F8. Age-depth plot, Site U1516. Vertical bars = depth uncertainty on events (see Tables T5 and T6 for values). Age estimates are from Gradstein et al. (2012).

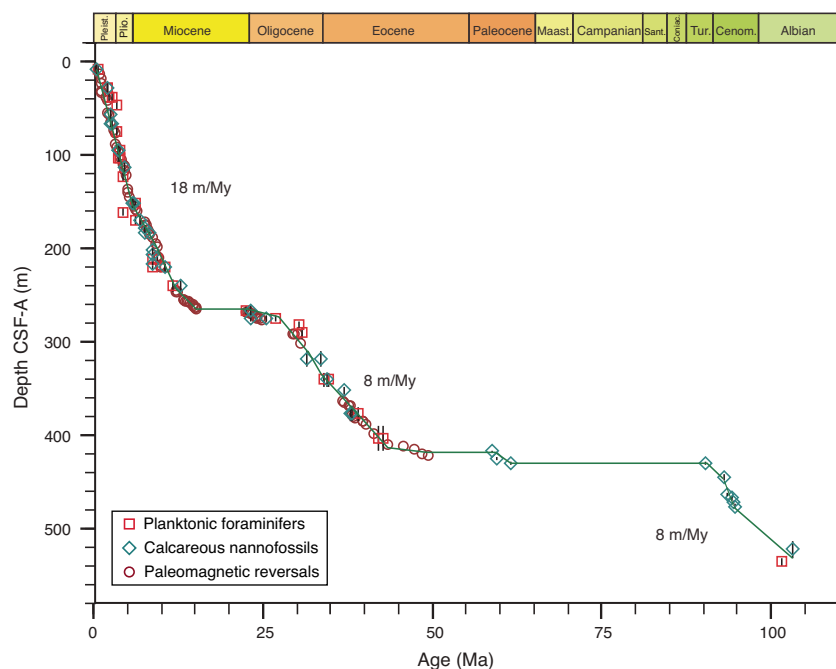
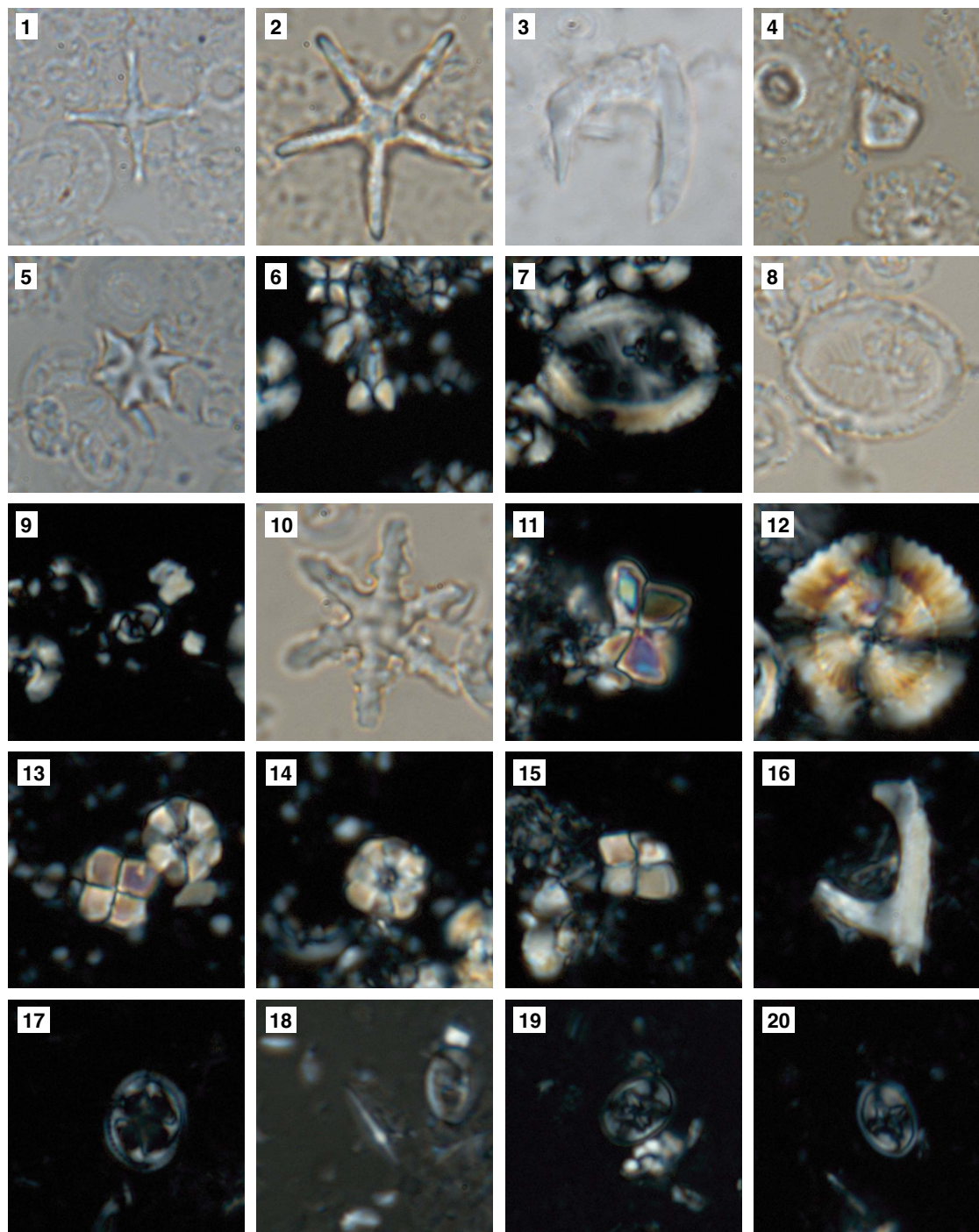


Table T7. Calcareous nannofossil distribution, Hole U1516A. [Download table in CSV format.](#)Table T8. Calcareous nannofossil distribution, Hole U1516C. [Download table in CSV format.](#)

Figure F9. Selected calcareous nannofossils, Site U1516. 1. *Discoaster tamalis* (U1516A-11H-CC). 2, 3. *Discoaster tamalis* (U1516A-17H-CC). 2. *Discoaster quinqueramus*. 3. *Nicklithus amplificus*. 4. *Minylithus convallis* (U1516A-27F-CC). 5. *Catinaster mexicanus* (U1516A-29F-CC). 6. *Sphenolithus akropodus* (U1516A-10R-CC). 7, 8. *Reticulofenestra oamaruensis* (U1516C-17R-CC). 9. *Clausicoccus subdistichus* (U1516C-15R-CC). 10. *Discoaster nodifer* (U1516C-15R-CC). 11. *Heliolithus riedelii* (U1516C-25R-2, 46–47 cm). 12. *Heliolithus kleinpellii* (U1516C-25R-2, 46–47 cm). 13. *Quadrum gartnerii* (right) and *Eprolithus floralis* (left) (U1516C-26R-6, 132–133 cm). 14. *Eprolithus octopetalus* (U1516C-30R-CC). 15. *Quadrum intermedium* (five elements) (U1516C-31R-CC). 16. *Ceratolithina naturalisteplateauensis* (U1516C-32R-CC). 17. *Axopodorhabdus biramiculatus* (U1516C-32R-CC). 18. *Lithraphidites acutus* (U1516C-34R-CC). 19. *Eiffellithus equibiramus* (U1516C-39R-CC). 20. *Eiffellithus monechiae* (U1516C-40R-CC).



lower part of this succession (Cores 28F and 29F) contains *Catinaster mexicanus* and rare *Catinaster calyculus*. Rare reworked specimens from the upper Eocene to lower Oligocene, including *R. umbilica*, *Isthmolithus recurvus*, and *D. saipanensis*, occur throughout this interval.

Sample 369-U1516C-6R-CC, 0–7 cm, contains *R. pseudo-umbilica*, *T. rugosus*, and *Discoaster challengerii* but lacks *Discoaster kugleri* or catinasters, indicating upper Miocene Subzone CN5b. *R. perplexa* occurs in high abundance, indicating a strong Southern Ocean component in the surface waters.

The interval from Sample 369-U1516C-7R-CC, 0–6 cm, through Core 10R contains a section spanning the Oligocene/Miocene boundary. Sample 7R-CC, 0–6 cm, contains *Sphenolithus calyculus*, *Cyclicargolithus floridanus*, and *Coccolithus miopelagicus*, suggesting lower Miocene Subzone CN1c. Nannofossil assemblages from Sample 8R-CC, 0–6 cm, through Core 9R contain frequent to common *Cyclicargolithus abisectus*, *Triquetrorhabdulus carinatus*, and *Coccolithus miopelagicus*, indicating Subzones CN1a–CN1b. The presence of *Sphenolithus delphix* in Sample 9R-CC, 0–5 cm, indicates close proximity to the base of the Miocene. Sample 10R-CC, 0–10 cm, contains *D. bisectus*, *Dictyococcites stavensis*, *T. carinatus*, and *Sphenolithus ciperoensis*, indicating the upper Oligocene Zone CP19. The stratigraphic placement of this interval across the Oligocene/Miocene boundary is corroborated by the paleomagnetic stratigraphy, which assigns this interval to the distinctive Chron C6c (see [Paleomagnetism](#)).

The interval from Sample 369-U1516C-11R-CC, 16–21 cm, through Core 14R contains lower Oligocene Zone CP17. At this site, the zone is characterized by abundant, moderately to well-preserved calcareous nannofossils, including *Sphenolithus akropodus* (Figure F9, Specimen 6), *Sphenolithus predistentus*, and *Chiasmolithus altus* without *R. umbilica* or *Sphenolithus distentus*. Upper Eocene taxa such as *I. recurvus* and *D. saipanensis* occur as rare reworked specimens.

The interval from Sample 369-U1516C-15R-CC, 0–5 cm, through Core 20R contains a sequence of sediments across the Eocene/Oligocene boundary. The interval from Sample 15R-CC, 0–5 cm, though Core 16R contains a calcareous nannofossil assemblage that includes *I. recurvus*, *R. umbilica*, *Ericsonia formosa*, and abundant *Clausicoccus subdistichus* (Figure F9, Specimen 9). This association indicates earliest Oligocene Subzone CP16a. Nannofossils are abundant and well preserved throughout this subzone at Site U1516. Sample 17R-CC, 16–23 cm, contains common *I. recurvus*, *Reticulofenestra oamaruensis*, *Chiasmolithus oamaruensis*, and *D. saipanensis*, indicating uppermost Eocene Subzone CP15b. Nannofossils are abundant and well preserved in this sample. The interval from Sample 18R-CC, 11–16 cm, through Core 20R contains *C. oamaruensis* and *Cribrocentrum reticulatum* without *I. recurvus*, indicating upper Eocene Subzone CP15a.

The middle Eocene is contained in three cores at this site, and each sample represents a different biostratigraphic unit. Sample 369-U1516C-21R-CC, 14–19 cm, contains abundant, moderately preserved nannofossils, including *Chiasmolithus grandis* and *D. bisectus* without *Discoaster bifax*, that indicate Subzone CP14b. Sample 22R-CC, 15–20 cm, has only common, poorly preserved calcareous nannofossils with common *R. umbilica* and *Chiasmolithus solitus* but without *D. bisectus* or *Nannotetrina* spp., indicating Subzone CP14a. Sample 23R-3, 81–82 cm, has common, poorly preserved calcareous nannofossils with *Nannotetrina cristata* and rare, relatively small (>14 µm) *R. umbilica* but without *Coccolithus gigas*, indicating Subzone CP13c. The core catcher for Core 23R

consists of silicified limestone with abundant, glauconite-filled burrows, suggesting an omission surface similar to those found below in the Paleocene.

Sample 369-U1516C-24R-CC, 18–23 cm, contains a common but poorly preserved calcareous nannofossil assemblage that includes *Discoaster lodoensis*, *Discoaster keupperii*, *Toweius gamma-tion*, and *Toweius magnacrassus* without *Tribrachiatus orthostylus* or *Discoaster sublodoensis*. This association indicates lower Eocene Zone CP11.

Cores 369-U1516C-25R and 26R contain a sequence of glauconitic calcareous claystone beds separated by burrowed and partially mineralized horizons (e.g., interval 26R-1, 0–5 cm) that represent omission surfaces dividing sedimentary units of distinctly different age, composition, and nannofossil preservation. The upper part (~3.5 m) of Core 25R, represented by Samples 25R-3, 46–47 cm, and 25R-4, 18–19 cm, contains common, moderately preserved nannofossils, including *Discoaster mohleri* and *Heliolithus riedelii* (Figure F9, Specimen 11), which indicate the upper part of upper Paleocene Zone CP6. Zone CP6 is separated from the underlying sediment by a burrowed, mineralized horizon (interval 26R-4, 85–92 cm). The underlying interval in Core 26R, represented by Samples 25R-5, 85–86 cm, and 25R-6, 132–133 cm, contains *Heliolithus kleinpellii* (Figure F9, Specimen 12), *Heliolithus cantabriae*, *Fasciculithus tympaniformis*, and *Sphenolithus primus* without discoasters, indicating middle Paleocene Zone CP5. Core 26R is divided into upper and lower parts by a silicified, burrowed horizon at interval 26R-3, 50–55 cm. The upper part of this core, represented by Samples 26R-1, 65–66 cm, and 26R-3, 0–1 cm, contains a middle Paleocene calcareous nannofossil assemblage that includes *F. tympaniformis* and *Bomolithus elegans* but not *H. kleinpellii*, indicating Zone CP4. *H. cantabriae* is present in the former sample but not in the latter, indicating that Sample 26R-1, 65–66 cm, is from upper Zone CP4, whereas Sample 26R-3, 0–1 cm, is from lower in Zone CP4.

The condensed Paleogene section lies disconformably in the lower part of Core 369-U1516C-26R. This interval, represented by Samples 26R-5, 1–2 cm, and 26R-6, 89–90 cm, and the core catcher, are middle Turonian Zone CC12, as indicated by the presence of *Eiffellithus eximius* (sensu Verbeek) without *Marthasterites furcatus*. This zone continues downhole through Core 27R.

Samples 369-U1516C-28R-3, 141–142 cm, to 30R-2, 95–96 cm, contain a lower Turonian Zone CC11 nannofossil assemblage that includes *Quadrum gartnerii* (Figure F9, Specimen 13), *Quadrum intermedium*, *Eprolithus moratus*, and (small) *Ahmuellerella octoradiata*. Nannofossil abundance and preservation varies widely through this interval and appears to reflect the small-scale rhythmicity of the bedding, with darker intervals having abundant, well to moderately preserved nannofossils as opposed to the lighter intervals with few, moderately to poorly preserved nannofossils.

Subzone CC10b at this site includes a complete Cenomanian/Turonian boundary with an (apparently) complete OAE 2 sequence. Samples 369-U1516C-30R-CC, 9–14 cm, and 31R-1, 63–64 cm, contain *Eprolithus octopetalus* (Figure F9, Specimen 14), *Q. intermedium* (with five segments; Figure F9, Specimen 15), and very small *A. octoradiata* without *Q. gartnerii*, indicating the upper part of Subzone CC10b. The latter sample consists largely of calcareous nannofossils and opal-CT lepispheres, although nannofossil preservation remains good. The lower part of Subzone CC10b is, in part, barren of calcareous nannofossils and contains only siliceous microfossils, zeolites, and opal-CT lepispheres in a dark gray to black organic-rich claystone.

Subzone CC10a, represented in Samples 369-U1516C-32R-2, 4–7 cm, and 32R-CC, 0–5 cm, contains abundant to common, well-preserved nannofossils, including *Helenea chiastia*, *Ceratolithina naturalisteplateauensis* (Figure F9, Specimen 16), and *Axopodorhabdus biramiculatus*. The former sample is dominated by opal-CT lepispheres in a calcareous zeolitic claystone matrix. The latter sample also includes *Lithraphidites acutus* (s.s.).

Zone CC9 extends from Sample 369-U1516C-33R-CC, 22–27 cm, through Core 39R. Division of this zone is hampered to some degree by paleoecological exclusion of several taxa and preservational problems near the Albian/Cenomanian boundary. The interval from Sample 33R-CC, 22–27 cm, through Core 35R is placed confidently in middle to lower Cenomanian Subzone CC9c based on the presence of *Zeughrabdotus xenotus* and *Gartnerago nanum* without *Watznaueria britannica*. The absence of *Hayesites albiensis* and sporadic occurrence of *Corollithion kennedyi* on the Naturaliste Plateau preclude their use for division of Zone CC9. Nannofossil preservation is poor in samples from Cores 36R and 37R, although the presence and stratigraphic position of *Eiffellithus turriseiffellii* in these samples indicates Zone CC9. Sample 38R-CC, 24–29 cm, contains *W. britannica* and *E. turriseiffellii*, indicating upper Albian Subzones CC9a–CC9b. Sample 39R-CC, 8–13 cm, also includes *Eiffellithus equibiramus* (Figure F9, Specimen 19), a species known to occur in association with OAE 1d.

Sample 369-U1516C-40R-CC, 17–22 cm, lacks *Eiffellithus casulus*, *E. turriseiffellii*, and *E. equibiramus* but contains *Eiffellithus monechiae* (Figure F9, Specimen 20), indicating upper Albian Subzone CC8d. This horizon lies below the OAE 1d excursion. Calcareous nannofossils are common and moderately preserved in this sample but degrade notably downhole; Sample 41R-CC, 21–26 cm, is barren.

Planktonic foraminifers

Hole U1516A and U1516C core catcher samples were analyzed for planktonic foraminiferal biostratigraphy (Tables T6, T9, T10). Several thousand particles (multiple picking trays) were scanned routinely for each sample. Planktonic foraminiferal assemblages span the Pleistocene through upper Miocene in Hole U1516A and the upper Miocene through Albian in Hole U1516C. A large hiatus exists between the middle Paleocene and Turonian in Hole U1516C. Although a number of low-latitude marker species are present in the Neogene and, to a lesser extent, in the Paleogene, the low-latitude biozonation scheme of Wade et al. (2011) can generally be applied to these sediments. Cretaceous assemblages are largely dominated by smaller taxa (<200 µm); however, the assemblages lack classic low-latitude marker species. Ages for these intervals are based largely on evaluation of whole assemblages and co-occurrence of species according to their stratigraphic distribution as presented in Premoli Silva and Sliter (1995), Petrizzo (2000, 2001, 2003), Pearson et al. (2006), Petrizzo and Huber (2006), Gradstein et al. (2012), and Falzoni et al. (2014). Preservation of planktonic foraminifers is generally good at Site U1516, and some samples in the upper Albian are ranked as excellent. Abundance is more variable; the Neogene, Paleogene, and Turonian generally contain abundant planktonic foraminifers (>30% of total particles), and the Albian contains rare specimens (<5% of total sediment particles).

Table T9. Planktonic foraminifer distribution, Hole U1516A. [Download table in CSV format.](#)

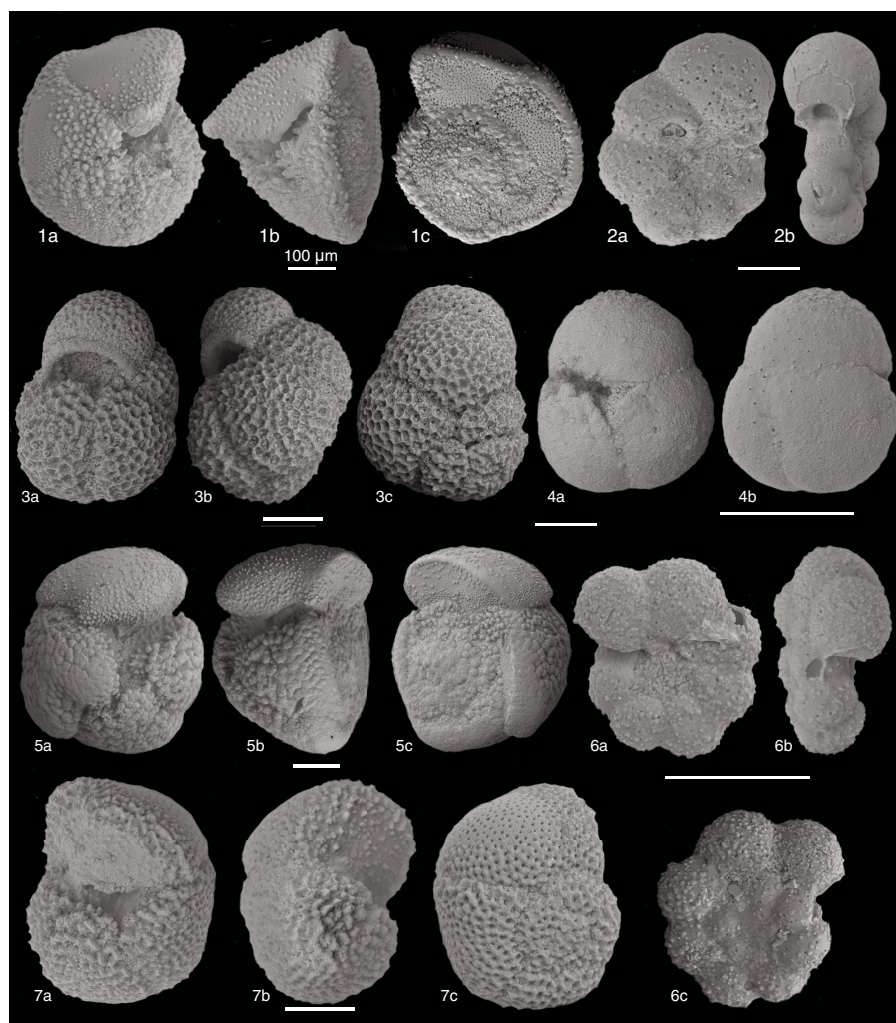
Table T10. Planktonic foraminifer distribution, Hole U1516C. [Download table in CSV format.](#)

Upper Pleistocene planktonic foraminiferal Subzone PT1b occurs in Sample 369-U1516A-1H-CC and is defined by the presence of *Truncorotalia truncatulinoides* (Figure F10, Specimen 1) and the absence of *Truncorotalia tosaensis*. Subzone PT1a in the lower Pleistocene occurs in Samples 2H-CC and 3H-CC and is defined by the overlapping occurrence of *T. truncatulinoides* and *T. tosaensis*. Sample 4H-CC is assigned to Zone PL6 based on the presence of *Globigerinoides extremus*, *Globorotalia inflata*, *Globorotalia crassaformis*, *Neogloboquadrina dutertrei*, and *T. tosaensis* and absence of *Globoturborotalita woodi*. Zone PL5 in the upper Pliocene occurs in Samples 5H-CC to 8H-CC and is defined by the overlapping occurrence of *Globigerinoides extremus*, *Globoturborotalita decoraperta*, *Globorotalia inflata*, *Globorotalia puncticulata*, and *G. crassaformis* and absence of *Dentoglobigerina altispira*. Samples 9H-CC to 11H-CC are assigned to Zone PL4 based on the presence of *D. altispira*, *Globorotalia crassaformis*, and *Globigerinoides extremus* and the absence of *Sphaeroidinellopsis seminulina*. The co-occurrence of *S. seminulina*, *Globorotalia margarita*, and *Globorotalia plesiotumida* in Samples 12H-CC to 14H-CC allow assignment to lower Pliocene Zone PL1.

The presence of *Globorotalia margaritae* and *Globigerinoides conglobatus* and the absence of *Globorotalia tumida* in Samples 369-U1516A-15H-CC to 18H-CC allow identification of late Miocene Zone M14 according to the Indo-Pacific zonation scheme (Gradstein et al., 2012). The underlying stratigraphic interval from Sample 19H-CC to Sample 28F-CC is assigned to Subzone M13b based on the overlapping occurrence of *Neogloboquadrina acostaensis*, *Globoturborotalita nepenthes* (Figure F10, Specimen 3), *Globoconella conoidea*, *Globorotalia plesiotumida*, and *Globoconella conomiozea*. Sample 29F-CC is assigned to Subzone M13a based on the absence of *Globorotalia plesiotumida* and the overlapping occurrence of *Globoturborotalita nepenthes*, *Globigerinoides extremus*, and *Globoturborotalita apertura*.

Hole U1516C overlaps with Hole U1516A. Samples 369-U1516C-2R-CC and 3R-CC are assigned to Subzone M13b based on the presence of *Globorotalia plesiotumida* and *Globoconella conomiozea* and the absence of *Globorotalia tumida* and *Globigerinoides conglobatus*. Sample 4R-CC lacks *G. plesiotumida*, *Paragloborotalia mayeri*, and *N. acostaensis* and is placed in Zone M12. Samples 5R-CC and 6R-CC both fall within Zone M11 based on the overlapping occurrence of *P. mayeri*, *G. decoraperta*, *G. nepenthes*, and *G. apertura*. Samples 7R-CC and 8R-CC are assigned to Zone M1 based on the overlapping occurrence of *Catapsydrax dissimilis*, *Globoquadrina dehiscens* (Figure F10, Specimen 7), and *Globigerina angustiumbilitata*, which indicates the presence of a hiatus in the early middle Miocene. Sample 9R-CC is Oligocene, most probably in Zones O6–O7 based on the overlapping occurrence of *Dentoglobigerina rohri*, *Dentoglobigerina pseudovenezuelana*, and *Dentoglobigerina tripartita* and the absence of *Paragloborotalia opima*. The overlapping ranges of *P. opima* and *Subbotina angiporoides* indicate that Sample 10R-CC is in planktonic foraminiferal Zones O5–O3. Sample 11R-CC is assigned to Zones O4–O3 based on the overlapping occurrence of *P. opima* and *Turborotalia ampliapertura*. Samples 12R-CC to 14R-CC are likely in Zones O1–O2 based on the presence of *Pseudohastigerina micra*, *S. angiporoides*, and *T. ampliapertura*; however, Sample 14R-CC shows strong downhole contamination because it contains >50% Miocene and Pliocene planktonic foraminifers. Samples 15R-CC and 16R-CC are in lower Oligocene Zone O1 based on the presence of *Subbotina eoceana* and *P. micra*, the latter of which is a dominant component of assemblages.

Figure F10. Selected Cretaceous and Cenozoic planktonic foraminiferal taxa, Site U1516. 1. *Truncorotalia truncatulinoides* (U1516A-1H-CC). 2. *Globigerinelloides* sp. (U1516C-26R-CC). 3. *Globoturbotalita nepenthes* (U1516C-2R-CC). 4. *Sphaeroidinellopsis seminulina* (U1516C-43R-CC). 5. *Globorotalia crassaformis* (U1516A-4H-CC). 6. *Microhedbergella praeplanispira* (U1516C-40R-CC). 7. *Globoquadrina dehiscens* (U1516C-7R-CC).



Samples 369-U1516C-17R-CC and 18R-CC are assigned to upper Eocene Zones E15–E16 based on the presence of multiple globigerinathekid taxa. Zone E14 is defined based on the overlapping occurrence of *Globigerinatheka barri* and *Subbotina gortanii* in Samples 19R-CC and 20R-CC. Undifferentiated Zones E13–E11 are assigned to Samples 21R-CC through 22R-CC based on the presence of *S. angiporoides* and *Acarinina primitiva*. Samples 23R-CC and 25R-CC are chert and were not analyzed for planktonic foraminifers. The assemblage in Sample 24R-CC contains reworked older taxa, although it predominantly reflects middle Eocene Zones E9–E10 based on the ranges of overlapping taxa, including *Globanomalina australiformis*, *Turbotalia pomeroli*, and *Guembeltioides nuttalli*.

Samples 369-U1516C-26R-CC to 27R-CC are mid-Turonian based on the presence of abundant whiteinellids and the overlapping ranges of biserial taxa such as *Planoheterohelix moremani*, *Planoheterohelix globulosa*, and *Planoheterohelix postmoremani*. Samples 28R-7, 110–115 cm, and 29R-CC likely occur within the Turonian *Helvetoglobotruncana helvetica* Zone because they contain abundant whiteinellids, *Dicarinella canaliculata*, *Dicarinella hagni*, and *Marginotruncana marginata*. Samples 30R-CC and 32R-CC are within the *Whiteinella archaeocretacea* Zone and span the

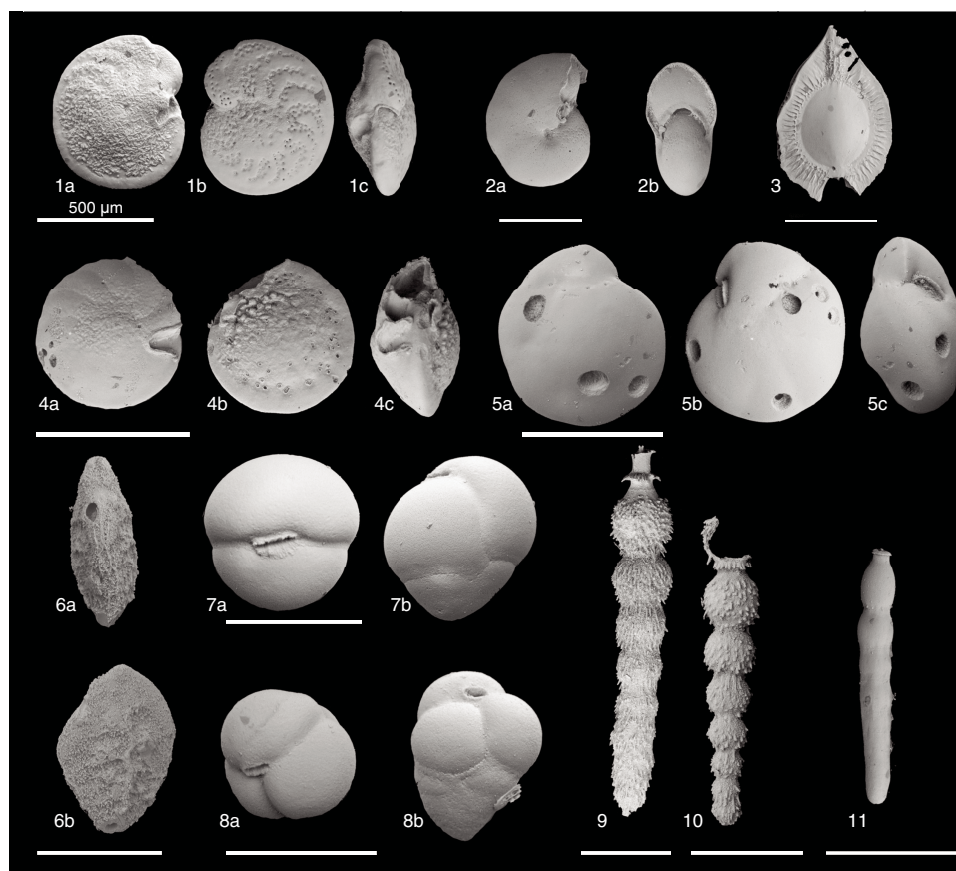
Cenomanian/Turonian boundary based on the presence of *Globigerinelloides bentonensis*. The core catcher sample from Core 31R is chert and was not analyzed for planktonic foraminifers. The presence of *G. bentonensis* and common muricohedbergellids and the absence of whiteinellids are indicative of the lower Cenomanian in Samples 33R-CC and 34R-CC. Samples 35R-CC to 41R-CC are unzoned but are likely middle to upper Albian based on a characteristic assemblage that includes various microhedbergellids and ticinellids. The *Thalmaninella appenninica* and *Pseudothalmaninella ticinensis* Zones of the upper Albian are constrained in Samples 39R-CC and 40R-CC based on the presence of rare ticinellids and *Microhedbergella praeplanispira* (Figure F10, Specimen 6) and a lack of biserials (Petrizzo and Huber, 2006; Gale et al., 2011). Sample 41R-CC contains only rare microhedbergellids and is consistent with an Albian age assignment.

Benthic foraminifers

The majority of Hole U1516A and U1516C core catcher samples were analyzed for benthic foraminifers, which are present in most samples (Tables T11, T12). Abundant benthic foraminifers are recorded in 19 samples. Rare occurrences of benthic foraminifers were observed in 25 samples. Benthic foraminifers are present in 6

Table T11. Benthic foraminifer distribution, Hole U1516A. [Download table in CSV format.](#)Table T12. Benthic foraminifer distribution, Hole U1516C. [Download table in CSV format.](#)

Figure F11. Selected benthic foraminiferal taxa, Hole U1516A. 1. *Planulina rugosa* (14R-CC). 2. *Pullenia* sp. cf. *Pullenia quinqueloba* (14R-CC). 3. *Fissurina* sp. (14R-CC). 4. *Cibicidoides* sp. aff. *Cibicidoides dohmi* (19R-CC). 5. *Oridorsalis* sp. (19R-CC). 6. *Latibolivina reticulata* (20R-CC). 7. *Dorothia brevis* (20R-CC). 8. *Eggerella bradyi* (20R-CC). 9, 10. *Siphonodosaria subspinosa* (19R-CC). 11. *Nodosaria* sp. (19R-CC).



samples, and Samples 369-U1516C-14R-CC, 25R-CC, 31R-CC, 35R-CC, 37R-CC and 41R-CC are barren of benthic foraminifers. Characteristic taxa are illustrated in Figure F11.

Samples 369-U1516A-1H-CC to 3H-CC yield taxa indicative of a bathyal environment (van Morkhoven et al., 1986). Abundant *Cibicides* spp., *Pyrgo murrhina*, and *Osangularia* sp. occur throughout this interval. The Pliocene benthic foraminiferal assemblage (Samples 4H-CC to 14H-CC) is characterized by the frequent occurrence of *P. murrhina* and dominant *Cibicidoides*. The bathyal taxa *Cibicidoides wuellerstorfi*, *Laticarinina pauperata*, *Oridorsalis* sp. (from Sample 15H-CC downhole), *Spiroplectamina* sp., *Uvigerina* sp. 1, and *Uvigerina* sp. 2 (both taxa occur in Samples 16H-CC to 22H-CC) are elements of the Miocene benthic foraminiferal assemblage. Nodosariids are highly abundant from Sample 12H-CC downhole, and *Cibicidoides* spp. is the dominant taxon.

The occurrence of *Cibicidoides grimsdalei* and *Cibicidoides subhaidingerii* associated with agglutinated foraminifers and other deep-water taxa such as *Oridorsalis umbonatus* and *Nuttallides truempyi* in Samples 369-U1516C-10R-CC to 24R-CC indicates a bathyal paleodepth (van Morkhoven et al., 1986). Sample 25R-CC is barren of benthic foraminifers and unconformably overlies the Cretaceous succession.

The taxa *Paralabamina elevata*, *Osangularia* sp., *Planulina* sp., and *Gavelinella* sp. have discontinuous appearances in Samples

369-U1516C-26R-CC to 29R-CC. Other faunal elements include *Dorothia oxycona* and *Lenticulinella* spp.

Benthic foraminiferal assemblages across the Cenomanian/Turonian boundary interval include *Gavelinella* sp. 3 (Samples 369-U1516C-29R-CC, 30R-CC, 32R-CC, and 34R-CC), *Berthelina intermedia* (recorded below the Cenomanian/Turonian boundary in Samples 33R-CC and 34R-CC), and *Gavelinella* sp. 1 (Sample 33R-CC). Paleoenvironmentally indicative taxa recorded within this interval include *Glomospira* sp. and *Gaudryina pyramidata*, indicating a bathyal paleoenvironment (Kaminski and Gradstein, 2005).

Samples 369-U1516C-35R-CC and 37R-CC are barren of benthic foraminifers, and Samples 38R-CC to 41R-CC contain a foraminiferal assemblage indicative of bathyal environments.

Paleomagnetism

We measured the natural remanent magnetization (NRM) of all Hole U1516A, U1516C, and U1516D archive-half sections (Cores 369-U1516A-1H through 29F, 369-U1516C-2R through 41R, and 369-U1516D-2R through 5R). The archive-half sections were subjected to either 5, 10, 15, and 20 mT alternating field (AF) demagnetization (Cores 369-U1516A-1H through 6H) or 10 and 20 mT AF demagnetization, and all of them were measured with the pass-through superconducting rock magnetometer (SRM) at

Figure F12. Paleomagnetic results, Hole U1516A. Declination: red = samples from oriented APC cores. Intensity: blue = 0 mT AF demagnetization, red = 20 mT AF demagnetization. Magnetic susceptibility (MS: green = whole-round (10 IU offset), red = point source).

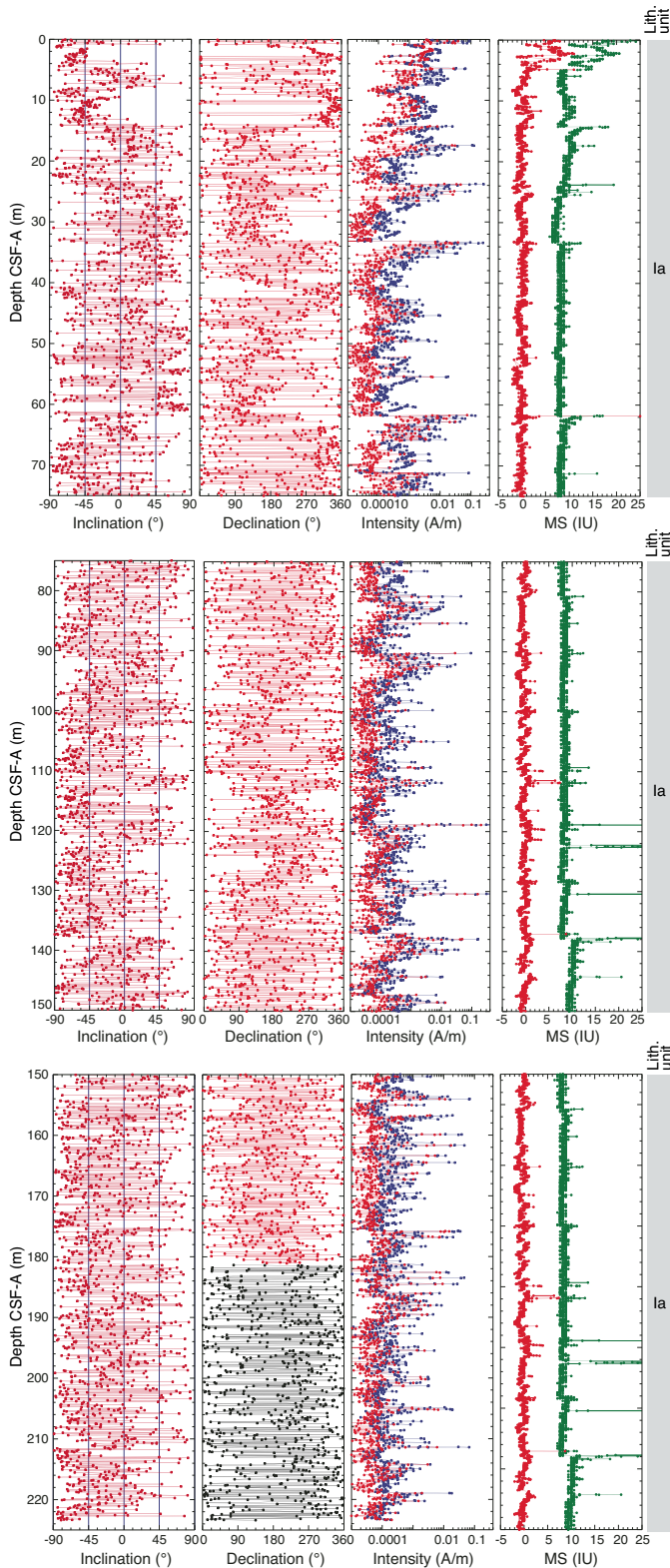


Table T13. Core orientation data, Hole U1516A. MTF = magnetic tool face declinations with respect to the double lines of the working halves, MTF' = declinations corrected for local declination (-4°). [Download table in CSV format.](#)

Core	MTF (°)	MTF' (°)	Orientation tool
369-U1516A-			
1H	291	287	FlexIT
2H	73.5	69.5	FlexIT
3H	126.5	122.5	FlexIT
4H	143.8	139.8	FlexIT
5H	8	4	FlexIT
6H	124.7	120.7	FlexIT
7H	52.7	48.7	FlexIT
8H	44	40	FlexIT
9H	338.5	334.5	FlexIT
10H	342.3	338.3	FlexIT
11H	261.5	257.5	FlexIT
12H	66.7	62.7	FlexIT
13H	243.7	239.7	Icefield MI-5
14H	267.9	263.9	Icefield MI-5
15H	176.7	172.7	Icefield MI-5
16H	187.4	183.4	Icefield MI-5
17H	216	212	Icefield MI-5
18H	42.7	38.7	Icefield MI-5
19H	354.3	318	Icefield MI-5
20H	164.5	160.5	Icefield MI-5

5 cm intervals. Discrete samples from this site were not measured because of time constraints.

Natural remanent magnetization of sedimentary cores

Hole U1516A

Downhole variations in Hole U1516A paleomagnetic results are shown in Figure F12. Hole U1516A cores (1H through 29F) were recovered with the APC and HLAPC systems. Cores 369-U1516A-1H through 20H were oriented with the FlexIT and Icefield MI-5 core orientation tools, which enabled magnetic declination correction for these cores (Table T13). In the deeper part of Hole U1516A, core orientation with the HLAPC system was not possible. APC and HLAPC core recovery was excellent. The recovered sedimentary cores consist mainly of calcareous ooze and silty or clayey calcareous ooze (lithostratigraphic Unit I; see Lithostratigraphy).

The NRM of cores from Hole U1516A shows downward-pointing moderate to steep inclinations, indicating a drilling-induced viscous overprint (e.g., Richter et al., 2007). The drilling-induced overprint can generally be removed by AF demagnetization (Figure F12). Declination values are largely scattered, except for the uppermost ~15 m and short intervals deeper than 15 m CSF-A, where distinct patterns of dominant declination values are apparent. NRM intensity in Hole U1516A sedimentary cores varies from 2.96×10^{-6} to 0.59 A/m with a mean of 2.7×10^{-3} A/m. Overall, the uppermost 24 m (Cores 369-U1516A-1H through 3H) exhibit generally elevated NRM intensity.

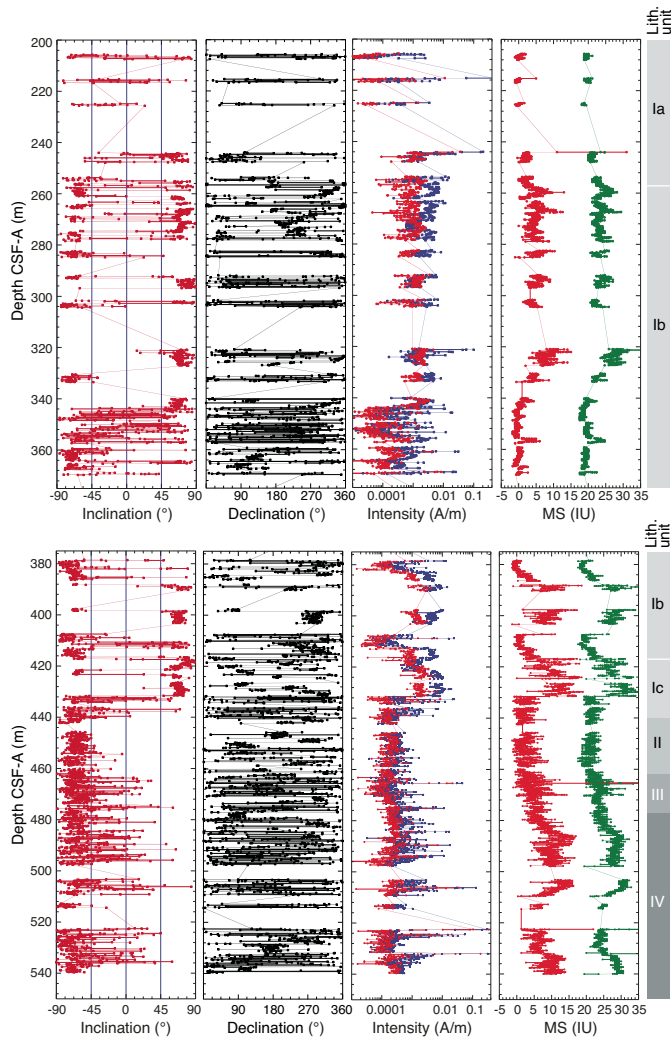
Whole-round low-field magnetic susceptibility in Hole U1516A sedimentary cores is low (Figure F12; see Petrophysics). More than half of the cores have negative magnetic susceptibility ranging from -1 to -5 instrument units (IU), indicating the predominant contribution of diamagnetic materials. Positive magnetic susceptibility occurs

mainly in the uppermost ~24 m. Approximately 12 magnetic susceptibility spikes (greater than ~5 IU) occur in Hole U1516A, mostly in the uppermost section of the cores, and correspond to elevated NRM intensity. The magnetic susceptibility spikes at the core tops were most likely introduced by the drilling process. For example, the magnetic susceptibility peak and elevated NRM intensity in Section 369-U1516A-1H-1 were noticed during paleomagnetic measurements. We subsequently found a 1–1.5 cm piece of rust, probably originating from one of the drill pipes in the uppermost 10 cm of the section.

Hole U1516C

Downhole variation in paleomagnetic results from Hole U1516C is shown in Figure F13. All Hole U1516C sedimentary cores were recovered with the RCB system. The uppermost 205.6 m of the hole was not cored, and the 205.6–223.9 m CSF-A interval overlaps with the basal part of Hole U1516A (see [Operations](#)). Hole U1516C sedimentary core recovery is moderate to poor from 205.6 to ~320 m CSF-A and improves deeper than ~320 m CSF-A. The recovered cores are composed of calcareous ooze, calcareous chalk, and claystone (the lower part of lithostratigraphic Unit I and Units II and III; see [Lithostratigraphy](#)).

Figure F13. Paleomagnetic results, Hole U1516C. Intensity: blue = 0 mT AF demagnetization, red = 20 mT AF demagnetization. MS: green = whole round (20 IU offset), red = point source.



Sedimentary cores recovered from 205.6 to ~439 m CSF-A exhibit both negative and positive NRM inclinations. AF demagnetization at 20 mT effectively removed the secondary overprints, and a distinct pattern of zones with dominantly positive and negative inclinations emerged after the 20 mT AF demagnetization treatment (Figure F13). Sedimentary cores from deeper than ~439 m CSF-A generally have upward-pointing NRM inclinations, and inclinations overall shift toward lower values after the 20 mT AF demagnetization treatment. Inclinations between ~344 and ~356 m CSF-A appear to be largely indistinguishable before and after 20 mT AF demagnetization. NRM intensity of the Hole U1516C sedimentary cores varies from 4.95×10^{-6} to 0.84 A/m with a mean of 2.7×10^{-3} A/m. In general, the ~250 to ~435 m CSF-A interval exhibits high NRM intensity mostly between 3.0×10^{-3} and 8.0×10^{-3} A/m, whereas NRM intensity in the rest of the cores is mostly $<3.0 \times 10^{-3}$ A/m. Several NRM intensity peaks observed in the Hole U1516C magnetic record (e.g., at 408.8 and 465.4 m CSF-A) correspond to subtle or distinct lithologic changes identified from visual inspection of core images.

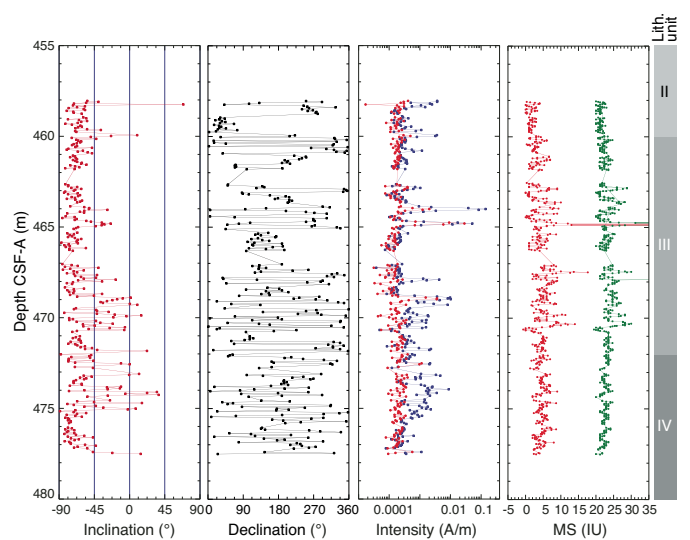
The majority of the low-field magnetic susceptibility values from the whole-round logger display positive values, except in the 205–225, 340–384, and 408–456 m CSF-A intervals, where negative magnetic susceptibility of as much as -2 IU occurs. Positive magnetic susceptibility varies from a few instrument units to ~15 IU. Downhole variations in magnetic susceptibility are generally linked to changes in lithology.

Hole U1516D

Downhole variations in Hole U1516D paleomagnetic results are displayed in Figure F14. Hole U1516D was drilled to core the Cenomanian/Turonian boundary interval recovered in Hole U1516C; the uppermost 458 m of Hole U1516D was not cored. Four sedimentary RCB cores (369-U1516D-2R through 5R) span from 458 to 472.4 m CSF-A with almost full recovery.

The recovered sedimentary cores have mostly moderate to low upward-pointing NRM inclinations (Figure F14). AF demagnetization led to a slight shift toward more negative inclinations. NRM intensity varies from 3.68×10^{-5} to 1.39×10^{-1} A/m with a mean of 1.64×10^{-3} A/m.

Figure F14. Paleomagnetic results, Hole U1516D. Intensity: blue = 0 mT AF demagnetization, red = 20 mT AF demagnetization. MS: green = whole round (20 IU offset), red = point source.



10^{-3} A/m and is mostly 10^{-4} A/m. Striking NRM intensity peaks of $\sim 1.0 \times 10^{-2}$ A/m occur at 464.0 and 464.8 m CSF-A and correspond to the greenish and dark greenish layers, respectively. Mean NRM intensity drops by about an order of magnitude after 20 mT AF demagnetization.

The most prominent feature of the downhole magnetic susceptibility variations is the occurrence of a magnetic susceptibility spike (80 IU) at 464.8 m CSF-A. The spike is accompanied by a NRM intensity peak at this level and corresponds to the dark greenish layer. Interestingly, magnetic susceptibility at ~ 464 m CSF-A, where another NRM intensity peak occurs, is subdued (Figure F14), probably indicating different environmental conditions. Magnetic susceptibility in the rest of the sedimentary core ranges from 0 to 10 IU and mostly fluctuates around 2–3 IU.

Paleomagnetic demagnetization results

Archive-half sections of Cores 369-U1516A-1H through 29F, 369-U1516C-2R through 41R, and 369-U1516D-2R through 5R were subjected to stepwise AF demagnetization up to 20 mT. The demagnetization results were visually inspected using the Laboratory Information Management System Information Viewer and the PuffinPlot (Lurcock and Wilson, 2012) and ZPlotit (<http://paleomag.ucdavis.edu/software-Zplotit.html>) software packages. Principal component analysis (PCA; Kirschvink, 1980) was performed using these software packages only for selected intervals to aid in defining characteristic remanent magnetizations (ChRMs) and assigning polarity. Shipboard preliminary analysis permitted the determination of first-order features of the paleomagnetic demagnetization results. Magnetic overprints are generally removed by 10 mT AF demagnetization, as indicated by significant changes in the demagnetization trajectories (Figures F15, F16). In many cases, ChRMs can be defined from the paleomagnetic data acquired from the pass-through measurements. ChRMs can be determined by PCA using two or three demagnetization steps that show a trajectory decaying toward the origin. In some samples, magnetic intensity either gradually increases or rapidly decreases and/or shows erratic directions upon demagnetization. In these cases, ChRMs cannot be isolated.

At Site U1516, two disturbed rock pieces were reoriented using the paleomagnetic method. First, a ~ 5 cm long black claystone fragment with burrows in the uppermost part of Section 369-U1516C-32R-1 (~ 469.9 m CSF-A) was disturbed by drilling; its bedding is oriented perpendicular to the bedding of the rest of the section. The fragment occurs near the critical interval of the Cenomanian/Turonian boundary, so it was essential to reinstate it to its original orientation. Because the age of the section is within the Cretaceous Normal Superchron (CNS), we took advantage of the CNS and measured the fragment at 2 cm intervals, which allowed us to reinstate the fragment by rotating it 90° clockwise. Second, the basal ~ 32 cm of Section 2R-1 was dropped during sectioning, and its orientation became ambiguous. The section was demagnetized at 0, 10, and 20 mT and measured with the SRM in 5 cm intervals, which allowed the basal segment to be reoriented. The orientation of the segment could only be determined after the demagnetization experiment. Apparently, the basal segment was in the wrong orientation during measurement. After the segment was rotated to its correct orientation, the section was again demagnetized at 20 mT and remeasured. NRM at the 0 and 10 mT demagnetization steps, however, could not be remeasured. Thus, if using the paleomagnetic data for this section, the results for the 0 and 10 mT demagnetization steps should be corrected.

We also encountered magnetic flux jumps of the SRM at this site. Frequent magnetic flux jumps occurred mainly between ~ 0030 and 1540 h (UTC +11 h) on 16 November 2017. Usually, 2–5 flux jumps are recorded in the y -axis, which results in near-zero inclinations and mostly westerly declinations (270°). When a magnetic flux jump occurs, NRM intensity rapidly increases and then gradually declines linearly. Flux jumps appeared randomly, sometimes during NRM measurement and sometimes during NRM measurement after 10 or 20 mT demagnetization.

Magnetic flux jumps affected measurement of Cores 369-U1516C-3R through 9R, which consist of mainly calcareous ooze with strong diamagnetism (Figure F13). High water content in these cores may have triggered the so-called “antenna effect” (Expedition 320T Scientists, 2009). However, Cores 1R and 2R have higher water content than Cores 3R through 9R and did not experience frequent magnetic flux jumps. Another suspected cause of the frequent flux jumps was magnetic field leakage through the joint between the SRM and the degausser as the ship was heading east. The cable connected to the SRM is well shielded, and the problem reported by Norris et al. (2014) does not appear to be the cause for the magnetic flux jumps we encountered. Nevertheless, several tests were run, with inconclusive results. Additional efforts to eliminate magnetic flux jumps included washing the sample tray with anti-static solution and removing the plastic wrap used in the prior point-contact magnetic susceptibility measurements from the section. Magnetic flux jumps still occurred frequently after these efforts.

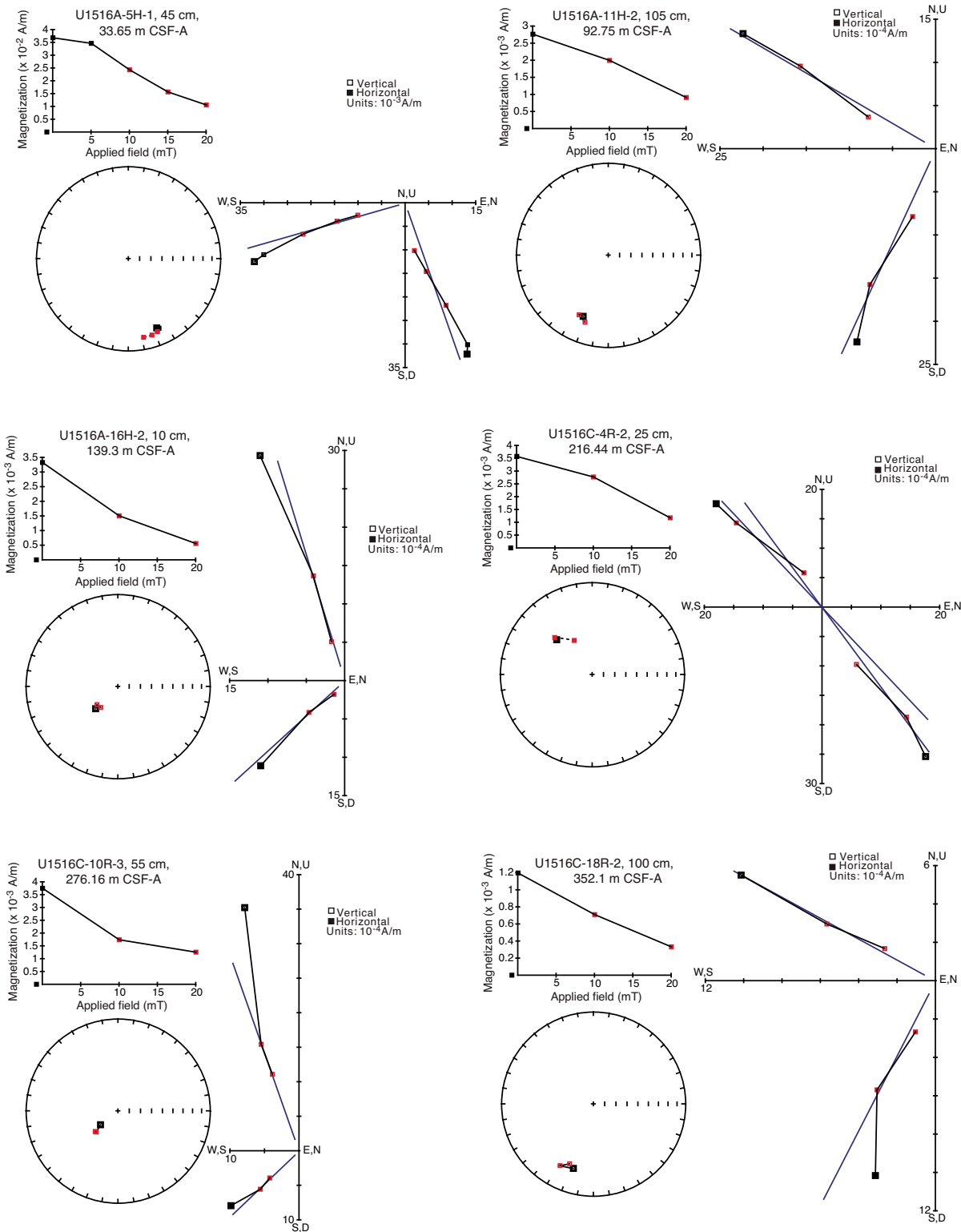
The final action we tried was reducing the speed of the tray motion by half, from 5 to 2.5 cm/s, at ~ 1530 h. Frequent magnetic flux jumps disappeared after ~ 1540 h. We were not sure whether the disappearance of the jumps was related to the reduction of the tray motion speed because magnetic flux jumps occurred occasionally afterwards, but slow tray motion was used consistently after this time. Introduction of artifacts due to the occasional flux jumps was generally avoided by repeating sequence measurements in which jumps occurred. After the flux jumps disappeared, we remeasured Cores 3R through 9R after 20 mT AF demagnetization treatment. Measurements affected by magnetic flux jumps were removed from the database.

Magnetostratigraphy

To define magnetic polarity, we mainly used inclinations from section-half measurements after the highest AF demagnetization treatment (20 mT). Age information from shipboard biostratigraphic analyses (see **Biostratigraphy and micropaleontology**) were used as the basis for making tentative correlations of the established magnetic polarity zones with the geomagnetic polarity time-scale (GPTS) (Ogg et al., 2012). For clarity of presentation, we divided Hole U1516A magnetostratigraphy into five 50 m long subsections and Hole U1516C magnetostratigraphy into three 100 and 125 m long parts (Figure F17).

Hole U1516A penetrates to ~ 224 m CSF-A with 104% average recovery. Hole U1516A sedimentary cores consist entirely of lithostratigraphic Subunit Ia. Coring in Hole U1516C started at ~ 196 m CSF-A and penetrated to ~ 542 m CSF-A with 60% average recovery. Therefore, the ~ 196 to ~ 224 m CSF-A interval overlaps in Holes U1516A and U1516C, unfortunately with very poor recovery in Hole U1516C (see **Stratigraphic correlation**). The recovered Hole U1516C sedimentary cores consist of the lower part of Subunit Ia, all of Subunits Ib and Ic, and Units II–IV. For clarity of presentation,

Figure F15. Vector endpoint diagrams (Zijderveld, 1967) of section halves from Unit I, Site U1516.

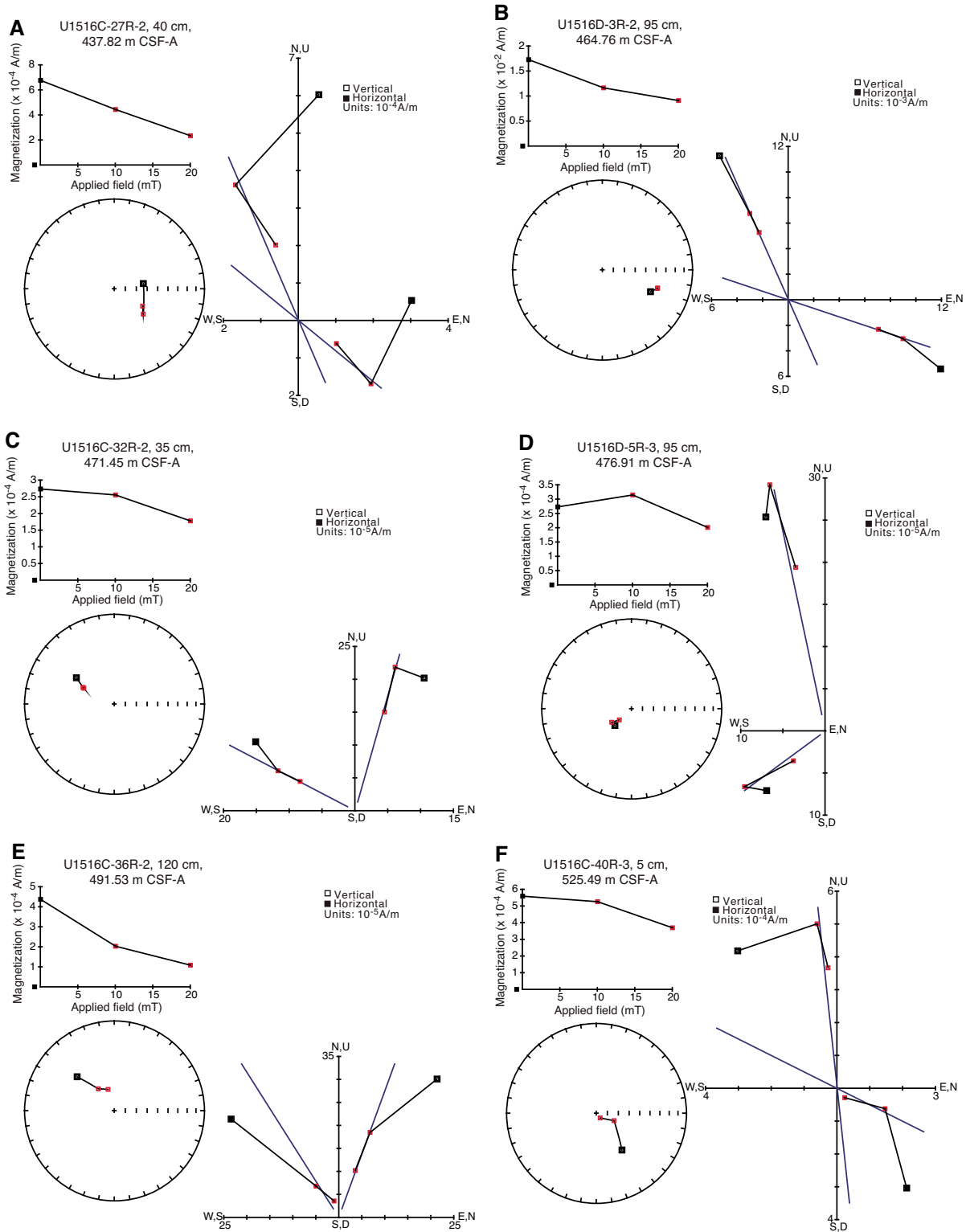


magnetostratigraphies from Holes U1516A and U1516C are presented separately.

In Hole U1516A, paleomagnetic inclinations, despite weak magnetic intensity and considerable scatter, show distinct variation patterns characterized by zones of negative and positive inclination

(Figure F17). Magnetic polarity zones are very well defined, with negative values indicating normal polarity and positive values indicating reversed polarity. Only one interval (160–170 m CSF-A) had a random distribution of paleomagnetic inclinations and thus could not be confidently assigned a magnetic polarity. We identified 39

Figure F16. Vector endpoint diagrams (Zijderveld, 1967) of section halves from Units (A, B) II, (C, D) III, and (E, F) IV.



magnetic polarity zones in the Hole U1516A sedimentary cores. Correlation of these polarity zones with the GPTS (Gradstein et al., 2012) was performed core by core with the biostratigraphic constraints from the base of each core (paleontology samples from the core catchers). The Hole U1516A magnetic polarity sequence ap-

pears to be remarkably complete and is correlated with Chron C1n through Subchron C5n.1n.

In Hole U1514C, paleomagnetic inclinations from 344 to 359 m CSF-A are randomly distributed, and magnetic polarity cannot be assigned (Figure F17). For the rest of the Hole U1516C sedimentary

Natural gamma radiation

NGR ranges from 1.6 to 68 counts/s at Site U1516 (Figures F19, F20, F21). It rapidly decreases in the uppermost 10 m and then stabilizes around 5 counts/s throughout the calcareous and nannofossil ooze in lithostratigraphic Unit I (see [Lithostratigraphy](#)). This decrease in NGR is reflected in the deconvolved uranium (U) and potassium (K) contents (Figure F22). In Unit I, NGR spikes sporadically occur in layers enriched in clays and sponge spicules (Figure F19; see [Lithostratigraphy](#)). These spikes, where NGR values exceed 10 counts/s, occur mainly from 100 to 166 m CSF-A; the lowest spike of Hole U1516A occurs at 195 m CSF-A. K, U, and thorium (Th) contents are all elevated in the clay-rich and sponge spicule-rich layers compared with surrounding intervals. Low U and Th contents prevent reliable interpretation of the U/Th ratio.

The transition from calcareous ooze to calcareous chalk (see [Lithostratigraphy](#)) at 258 m CSF-A is marked by a slight decrease in NGR to 3 counts/s (Figure F20). NGR increases to 5–10 counts/s where the lithology becomes more clayey at 388 m CSF-A. Another NGR increase at 417 m CSF-A to 17 counts/s marks the transition to indurated claystone that characterizes lithostratigraphic Subunit Ic, which encompasses the Turonian to Eocene unconformity (see [Lithostratigraphy](#) and [Biostratigraphy and micropaleontology](#)). A decrease in NGR to <10 counts/s marks a return to chalk at the top of Unit II (431 m CSF-A). Deeper than 465 m CSF-A, near the base of Unit II, NGR increases from 15 to 68 counts/s with an increase in clay content to the bottom of the hole (545 m CSF-A). In this interval, five peaks occur at 469.6 m CSF-A, the top of Unit III, and at 479.9, 488, 505, and 538 m CSF-A (Figure F20). These peaks can be correlated with Site U1513 (see [Stratigraphic correlation](#)). The peaks at 469.6 and 479.9 m CSF-A (black arrows on Figures F20, F23) could correspond to OAE 2 and possibly the Mid-Cenomanian Event (MCE), respectively. In the deconvolution of NGR, a peak in U content was observed in these intervals (Figure F23). In Hole U1516D, the peak in U matches the peak in NGR in the finely

laminated black claystone layer (Figures F21, F24) (see [Lithostratigraphy](#)).

Magnetic susceptibility

Magnetic susceptibility was measured on all whole-round sections with the WRMSL, and point magnetic susceptibility measurements were made on the archive-half sections with the SHMSL. The magnetic susceptibility data from the WRMSL and SHMSL are comparable (Figures F19, F20, F21).

Magnetic susceptibility ranges from -4.11 to 129.73 instrument units (IU). Magnetic susceptibility decreases from 10 to 0 IU in the uppermost 10 m and then stabilizes around zero throughout lithostratigraphic Subunit Ia (see [Lithostratigraphy](#)) (Figure F19). Magnetic susceptibility spikes to >10 IU sporadically throughout Subunit Ia, mostly from 120 to 190 m CSF-A. These spikes are not necessarily correlated to the NGR spikes, suggesting that the concentration and nature of iron-bearing minerals are disconnected from the occurrence of layers that are more clay rich (see [Lithostratigraphy](#)). At 244 m CSF-A, magnetic susceptibility increases to 3 IU where the lithology changes from ooze (Subunit Ia) to chalk (Subunit Ib) (Figure F20). Another magnetic susceptibility increase to 9 IU occurs at 320 m CSF-A, followed by a decrease to -1 IU from 340 to 388 m CSF-A. Magnetic susceptibility then fluctuates with clay content, increasing to 9 IU in the clayey chalk from 388 to 403 m CSF-A and decreasing from 403 to 417 m CSF-A. It increases to 10 IU between 417 and 431 m CSF-A. The same trend was observed in NGR and corresponds to a transition from clayey chalk to claystone at 417 m CSF-A at the top of Subunit Ic. Magnetic susceptibility returns to 0 IU at 431 m CSF-A, coinciding with another change in lithology (claystone to chalk) that marks the Unit I/II boundary. From 460 to 488 m CSF-A, it increases to 15 IU in clay-rich sediment. Magnetic susceptibility ranges from 0 to 10 IU to the bottom of the hole. In the possible OAE 2 interval (465–470 m CSF-A), the signal shows high-amplitude fluctuations at high frequencies

Figure F19. Physical properties, Hole U1516A. Black data curves = moving average.

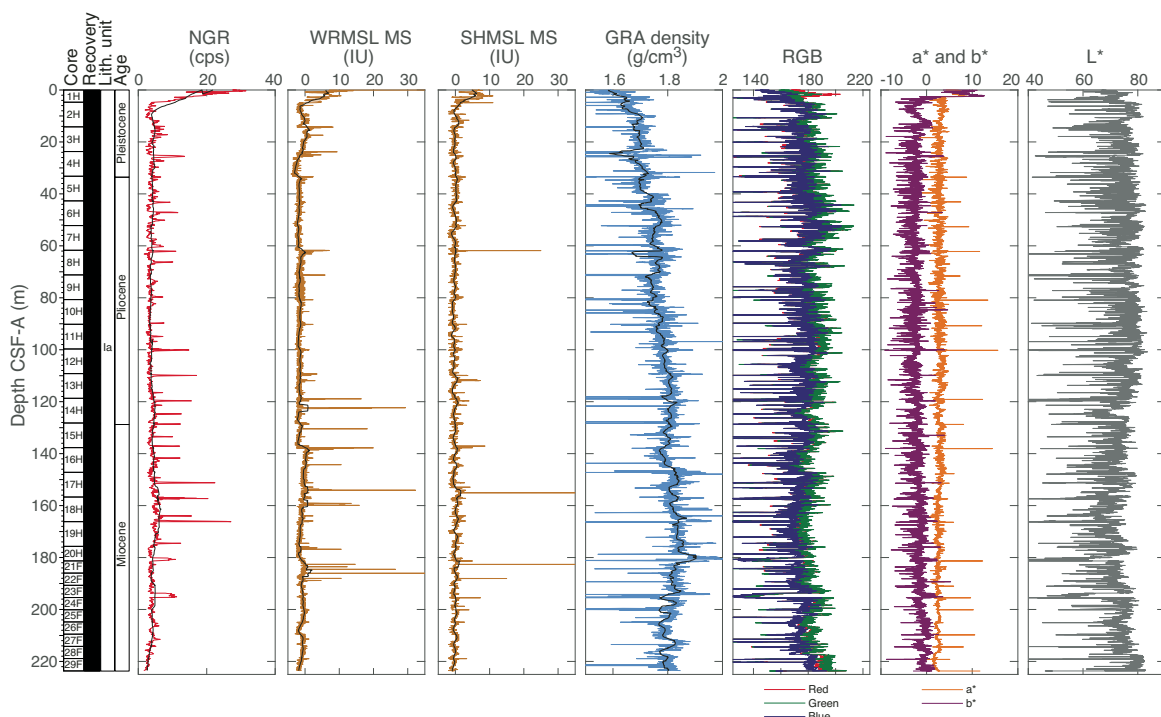


Figure F20. Physical properties, Hole U1516C. Black arrows = peaks corresponding to OAE 2 and possible MCE. Black data curves = moving average.

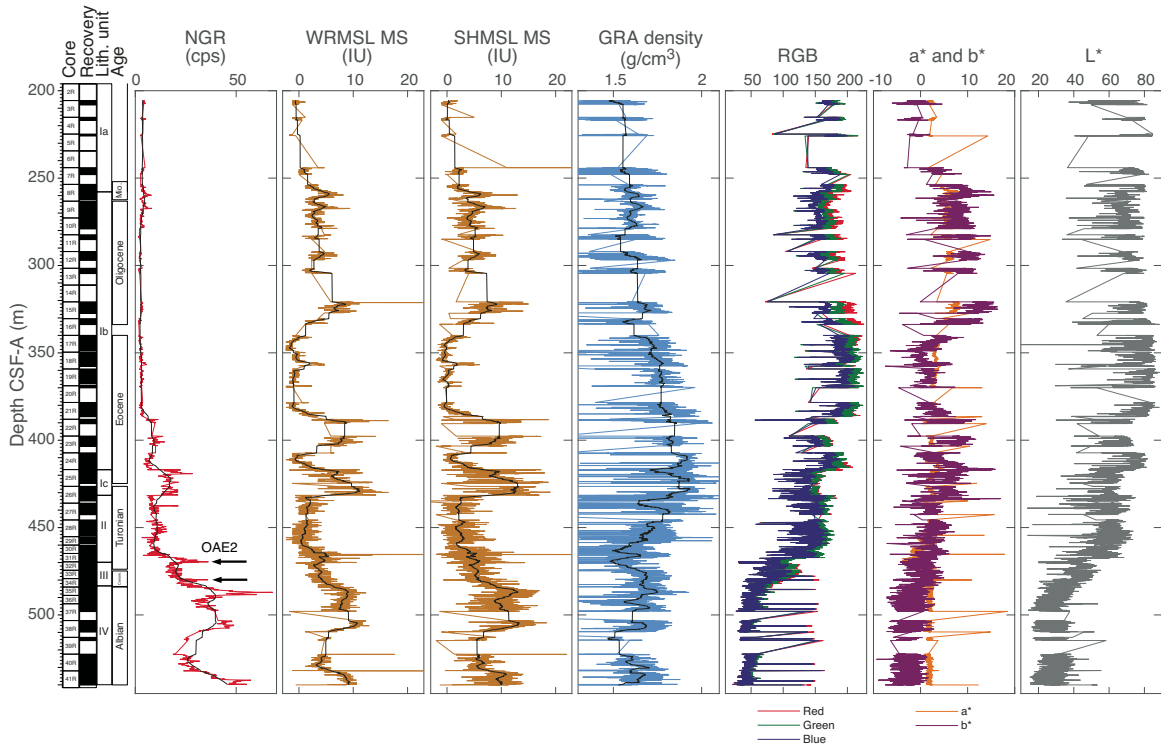
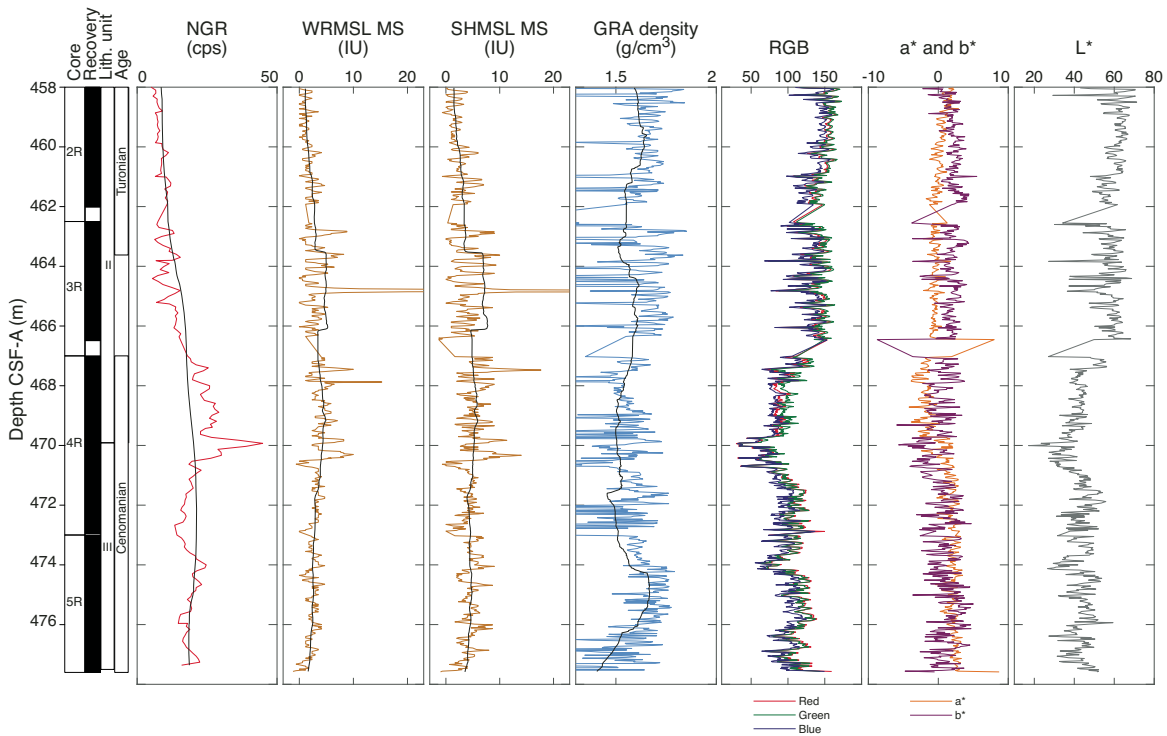


Figure F21. Physical properties, Hole U1516D. Black data curves = moving average.



(tens of centimeters) (Figure F20), similar to magnetic susceptibility at Site U1513 (see [Stratigraphic correlation](#) and [Petrophysics](#) in the Site U1513 chapter [Huber et al., 2019b]). In the upper Albian (485–505 m CSF-A), magnetic susceptibility plateaus around 10 IU.

GRA bulk density

GRA bulk density in Hole U1516A, which was measured on the WRMSL, generally increases with depth through the uppermost ~180 m of the Pleistocene to Miocene calcareous ooze that characterizes

Figure F22. NGR data, Hole U1516A. Black data curves = moving average. U/Th ratio: vertical dashed line = 1:1 ratio.

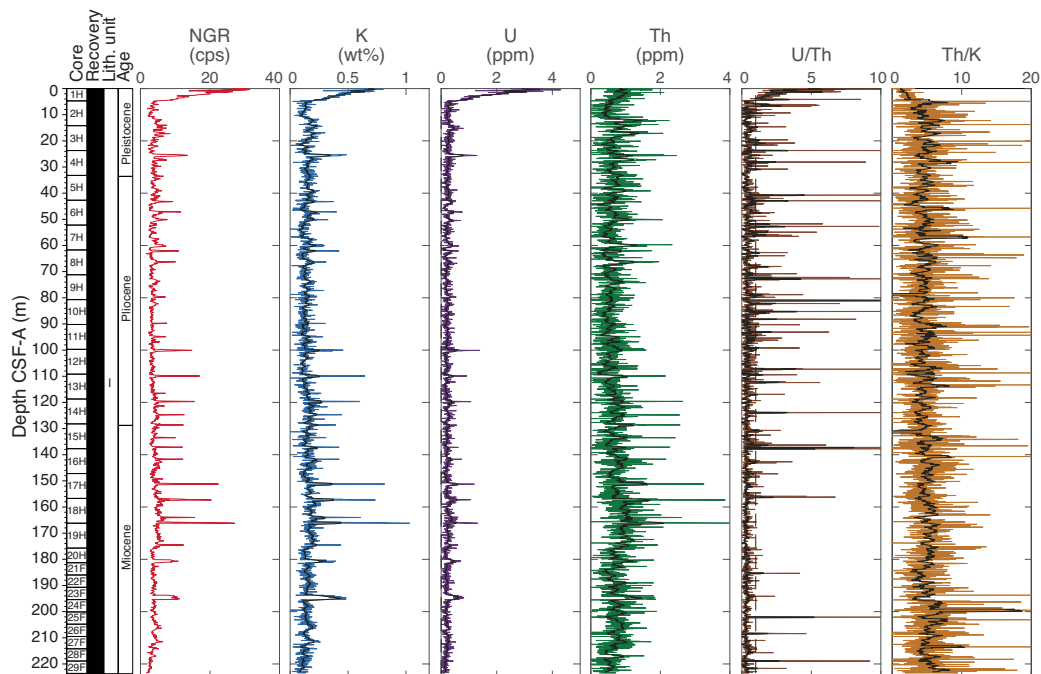
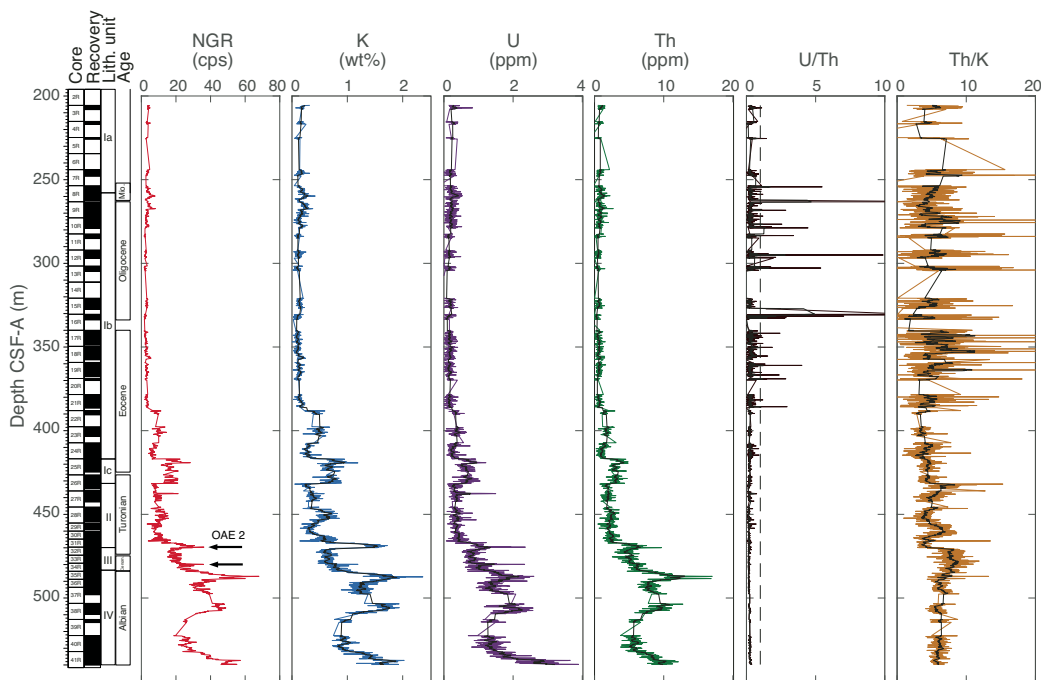


Figure F23. NGR data, Hole U1516C. U/Th ratio: vertical dashed line = 1:1 ratio. Black arrows = peaks that correspond to OAE 2 and possible MCE.



lithostratigraphic Unit I (Figure F19). In this interval, GRA bulk density increases steadily from 1.65 g/cm³ near the seafloor to 1.90 g/cm³ near 180 m CSF-A. Lower in Unit I in Hole U1516C, in intervals that overlap with Hole U1516A (~206–224 m CSF-A; see [Lithostratigraphy](#)), GRA bulk density displays higher variability and slightly lower values between 1.6 and 1.8 g/cm³, possibly reflecting the different coring system used in this hole (RCB). Deeper than 224 m CSF-A, GRA bulk density increases with depth in Subunit Ib, reaching a maximum of ~1.95 g/cm³ for the site near ~430 m CSF-A. This interval also re-

ords a relatively sharp decrease in porosity and increases in *P*-wave velocity, magnetic susceptibility, NGR, and thermal conductivity (Figure F25). These changes suggest an increase in compaction and/or cementation in the condensed interval overlying the Turonian to Eocene unconformity (see [Biostratigraphy and micropaleontology](#) and [Paleomagnetism](#)). Deeper than ~430 m CSF-A, GRA bulk density decreases. Well-resolved, 15–30 cm thick cycles in values with 0.2 g/cm³ fluctuations characterize the interval between 448 and 467 m CSF-A. These fluctuations correspond to light–dark alternations between the

Figure F24. NGR data, Hole U1616D. Black arrows = peaks corresponding to OAE 2 and possible MCE. Black data curves = moving average. U/Th ratio: vertical dashed line = 1:1 ratio.

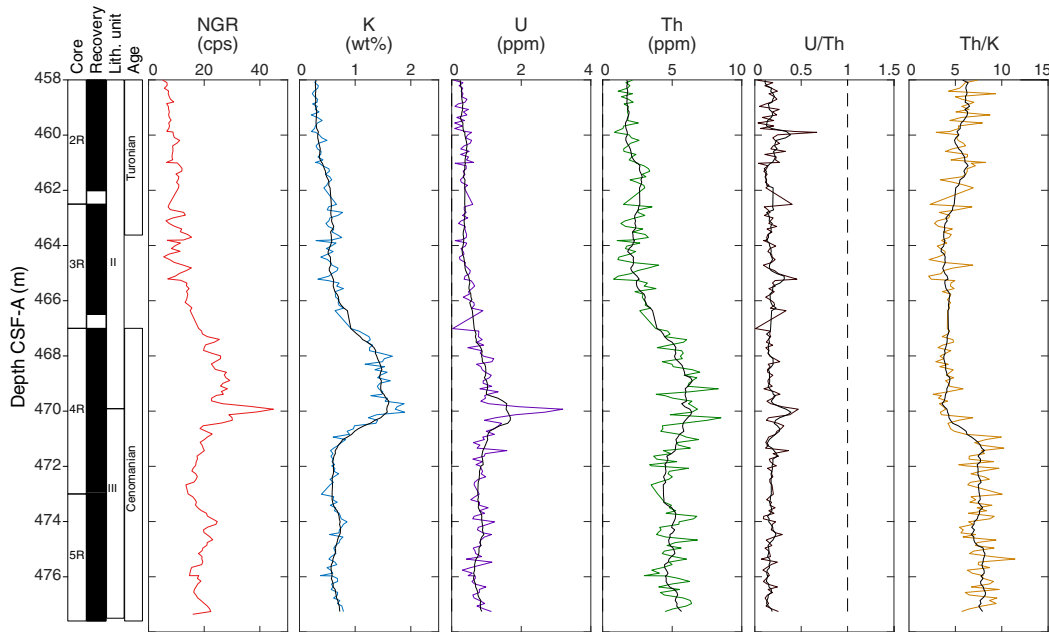
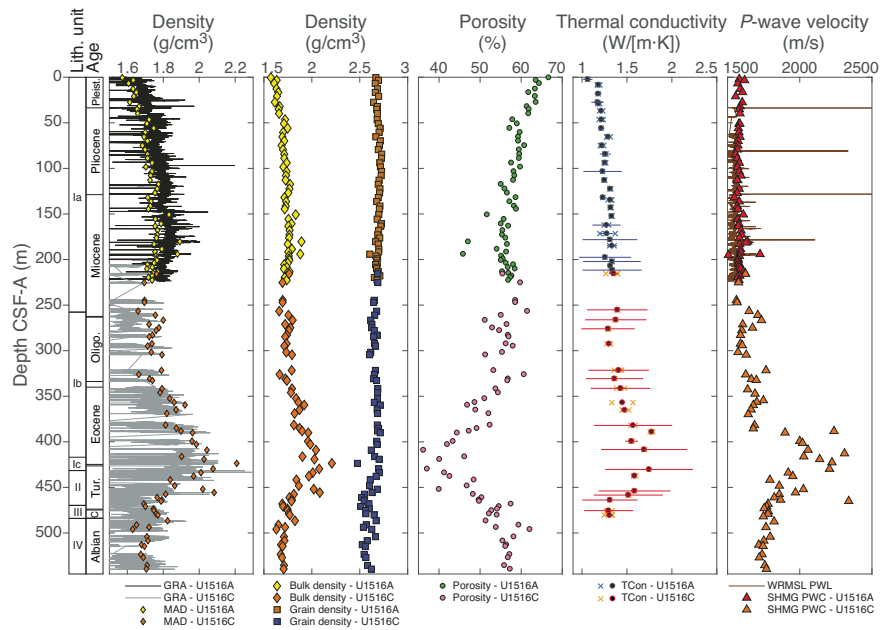


Figure F25. Density, porosity, thermal conductivity (bars = 1σ standard deviation), and P-wave velocity, Site U1516.



calcareous chalk and claystone with nanofossils lithologies in lithostratigraphic Unit II. In the Unit III claystone spanning the Cenomanian/Turonian boundary interval, GRA bulk density decreases to an average of 1.6 g/cm^3 between 467.5 and 474.5 m CSF-A. In lowermost Unit III and the dark Albian to Cenomanian claystone deeper than ~475 m CSF-A in Unit IV, GRA bulk density ranges from 1.5 to 1.75 g/cm³ and co-varies with trends in the magnetic susceptibility and NGR data.

Color reflectance

High-resolution (2.5 cm) reflectance spectroscopy and colorimetry (RSC) data such as lightness variability (L*), red versus green (a*),

and blue versus yellow (b*) from archive-half sections were measured on the SHMSL but display significant amounts of instrumental noise. With the exception of the uppermost 2.5 m, which records high a* and b*, RSC values from shallower than ~226 m CSF-A are relatively constant, averaging 73 (L*), 2.8 (a*), and -1.9 (b*) (Figures F19, F20, F21). This interval corresponds to lithostratigraphic Subunit Ia, which is composed of nanofossil ooze (see **Lithostratigraphy**). L* is slightly higher (80) from 226 to 370 m CSF-A and then decreases downhole with minor variations to ~490 m CSF-A. L* is relatively low (<math><40</math>) but constant overall from ~490 m to the bottom of Hole U1516C, corresponding to the Albian to Cenomanian black

and dark greenish gray nannofossil-rich claystone of Unit IV (see [Lithostratigraphy](#)). a^* and b^* increase deeper than 244 m CSF-A through the transition to the Miocene to Eocene chalk lithologies in Subunit Ib and then decrease downhole between 325 and 350 m CSF-A, coinciding with a decrease in magnetic susceptibility. Deeper than 350 m CSF-A, a^* is relatively constant (~ 2) to the bottom of Hole U1516C, with the exception of one decrease around 470 m CSF-A that corresponds to the relatively greenish interval around the Cenomanian/Turonian boundary. b^* increases from ~ 3 to 11 from 350 to 400 m CSF-A and then decreases downhole through Units II and III with minor variations to ~ 480 m CSF-A. From ~ 480 m CSF-A to the bottom of the Hole U1516C in Unit IV, b^* is relatively constant at ~ 3 .

Bulk density, grain density, and porosity

Bulk density, grain density, and porosity were measured on representative discrete samples of cored material using MAD measurements (Figure [F25](#)). Typically, one or two samples per core were taken for MAD measurements, depending on the rate of recovery. Bulk density increases from ~ 1.57 to 1.75 g/cm³ from 0 to ~ 150 m CSF-A, with essentially no change between ~ 150 and ~ 300 m CSF-A. Bulk density increases from ~ 1.75 to ~ 2.1 g/cm³ from ~ 300 to ~ 425 m CSF-A and decreases to ~ 1.7 g/cm³ at the base of Hole U1516C (540.1 m CSF-A). Little variation was observed in grain density values, all of which are essentially between 2.50 and 2.75 g/cm³. The porosity-depth curve is inversely proportional to the bulk density–depth curve, in that porosity values are between $\sim 65\%$ and 35% with one outlier at 18% (423.62 m CSF-A). A prominent porosity decrease around 420 m CSF-A corresponds to a condensed and indurated interval of lithostratigraphic Subunit Ic (see [Lithostratigraphy](#)).

Thermal conductivity, downhole temperature, and heat flow

Thermal conductivity at Site U1516 was measured on less disturbed cores; however, null results were obtained from multiple samples. Thermal conductivity is variable, ranging from 1.06 to 1.79 W/(m·K) (Figure [F25](#)), and gradually increases from 1.06 W/(m·K) near the seafloor to 1.5 W/(m·K) at 365 m CSF-A. From 382 to 430 m CSF-A, thermal conductivity increases to ~ 1.8 W/(m·K). Below the contact between lithostratigraphic Units I and II around 430 m CSF-A, thermal conductivity decreases to 1.25 W/(m·K) (see [Lithostratigraphy](#)).

Downhole temperatures were obtained with the APCT-3. A formation temperature was calculated from each APCT-3 record using the TP-Fit MATLAB script that identifies the characteristic peak in temperature during penetration of the core barrel and removes thermal spikes associated with the friction of the core barrel when it enters and exits the sediment. Equilibrium in situ temperature estimates were obtained in Cores 369-U1516A-3H, 5H, 7H, and 17H (Table [T15](#)). Linear regression results in an estimated bottom water temperature of 3.71°C and a geothermal gradient of 26°C/km. Heat flow was calculated to be 25 ± 4 mW/m² based on downhole temperatures (Table [T15](#)) and using Bullard's method with a best-fit linear increase in thermal conductivity with depth as described by Pribnow et al. (2000).

P-wave velocity

The WRMSL *P*-wave logger (PWL) measured whole-round core *P*-wave velocity, and the Section Half Measurement Gantry (SHMG) PWC measured working-half section and discrete sample velocity. Reported velocity values are based on automatically picked first arrival times. One or two measurements per core were taken

Table T15. Downhole temperature, Site U1516. [Download table in CSV format.](#)

Core	Depth CSF-A (m)	Temperature (°C)
369-U1516A-		
3H	23.8	3.94
5H	42.8	5.28
7H	61.7	5.36
17H	156.7	7.78

with the PWC, typically near the location where MAD samples were collected. Whole-round *P*-wave velocity was measured on all cores between ~ 81 and ~ 225 m CSF-A (Figure [F25](#)). A technical issue with the WRMSL prevented these data from being collected for Cores 369-U1516A-1H through 9H (0–81 m CSF-A). In the intervals where both PWL and PWC measurements were taken, PWC velocity values are near the maximum PWL velocity values, excluding sparse outliers.

P-wave velocity is constant (~ 1600 m/s) from the top of Hole U1516A to ~ 245 m CSF-A. Velocity generally increases deeper than ~ 245 m CSF-A to a maximum of ~ 2300 m/s at ~ 420 m CSF-A before decreasing to ~ 1750 m/s at the base of Hole U1516C (~ 540 m CSF-A) (Figure [F25](#)). The peak around 420 m CSF-A corresponds to an increase in GRA and MAD bulk density, NGR, thermal conductivity, and magnetic susceptibility (Figures [F20](#), [F25](#)) and a change in lithology from calcareous chalk to claystone (see [Lithostratigraphy](#)). A decrease in *P*-wave velocity deeper than ~ 430 m CSF-A reflects the transition from the claystone unit to calcareous and nannofossil chalk lithologies (the transition from lithostratigraphic Subunit Ic to Unit II; see [Lithostratigraphy](#)).

Geochemistry

The geochemistry program at Site U1516 was designed to characterize the composition of interstitial water and solid sediments and to assess the potential presence of volatile hydrocarbons. The samples discussed below come from Holes U1516A (0–223.6 m CSF-A; Cores 369-U1516A-1H through 29F) and U1516C (244.0–541.6 m CSF-A; Cores 369-U1516C-7R through 41R).

Headspace hydrocarbon gases

A total of 56 headspace gas samples were taken for routine safety monitoring downhole to ~ 538 m CSF-A (Table [T16](#)). Effectively, no gas was detected.

Interstitial water analyses

For analysis of water chemistry, 52 interstitial water samples were taken by squeezing whole-round samples from sediment intervals in Holes U1516A and U1516C (Table [T17](#); Figure [F26](#)). Ion chromatography was used to measure chloride (Cl⁻), bromide (Br⁻), sodium (Na), and sulfate (SO₄²⁻), and inductively coupled plasma-atomic emission spectrometry (ICP-AES) was used to analyze barium (Ba), boron (B), lithium (Li), manganese (Mn), silicon (Si), iron (Fe), calcium (Ca), phosphorus (P), potassium (K), magnesium (Mg), sulfur (S), and strontium (Sr). All ICP-AES measurements were converted to molar concentrations, and we assumed all sulfur was present as sulfate (SO₄²⁻). Ammonium (NH₄⁺) was measured by spectrophotometry (Gieskes et al., 1991).

The preliminary plan for whole-round sampling was one sample per full 9.6 m core or every other half-length core. Interstitial water

samples were taken from Hole U1516A cores starting with the mudline and continuing to 220.31 m CSF-A (Sample 369-U1516A-29F-1, 141–151 cm). Sampling resumed at 246.25 m CSF-A in Hole U1516C cores (Sample 369-U1516C-7R-2, 76–86 cm) and continued to 537.76 m CSF-A (Sample 41R-4, 143–153 cm). Interstitial water samples were not taken from Cores 11R, 13R, 14R, and 20R because of poor recovery or highly disturbed material, and Cores 31R and 32R were not sampled because of their proximity to the Cenomanian/Turonian boundary. The small volumes of interstitial water extracted from some samples meant that some analyses could not be performed for these samples. Preference was given to ICP-AES and ion chromatography analyses because of the quantity of information generated using these techniques.

Salinity, pH, and alkalinity

The salinity of interstitial water samples is generally constant between 36.5 and 38.0, except for samples from lithostratigraphic Unit IV, in which it decreases to 31.5–37.0 (Table T17; Figure F26). This drawdown in salinity is reflected in ~15% Cl⁻ and Na depletions compared with seawater concentration. All other major and

minor ions show a clear synchronous drawdown in Unit IV caused by this dilution effect. Because the presence and decomposition of gas hydrate can be excluded as a source for low-salinity water, the input of a freshwater component at depth is indicated, most likely associated with downslope movement of larger sedimentary sequences.

Alkalinity and pH measurements were limited to depths shallower than ~440 m CSF-A (Cores 369-U1516A-1H-29F and 369-U1516C-7R through 21R, 26R, and 27R) because of the small volume of interstitial water obtained from all other samples. Alkalinity generally increases from 3.25 mM in the mudline sample to 6.55 mM at 153.10 m CSF-A (Sample 369-U1516A-17H-4, 140–150 cm), followed by a decrease downhole to 2.65 mM at 430.41 m CSF-A (Sample 369-U1516C-26R-3, 135–145 cm) (Table T17; Figure F26). This pattern is compatible with low organic matter metabolization rates, which are also indicated by synchronous increases in ammonia and decreases in SO₄²⁻ (see **Sulfate and ammonium**). pH values decrease from 7.76 at the mudline to 7.33 at 332.32 m CSF-A (Sample 369-U1516C-16R-2, 91–101 cm), followed by a slight increase to 7.43 at the bottom of the hole (Table T17; Figure F26).

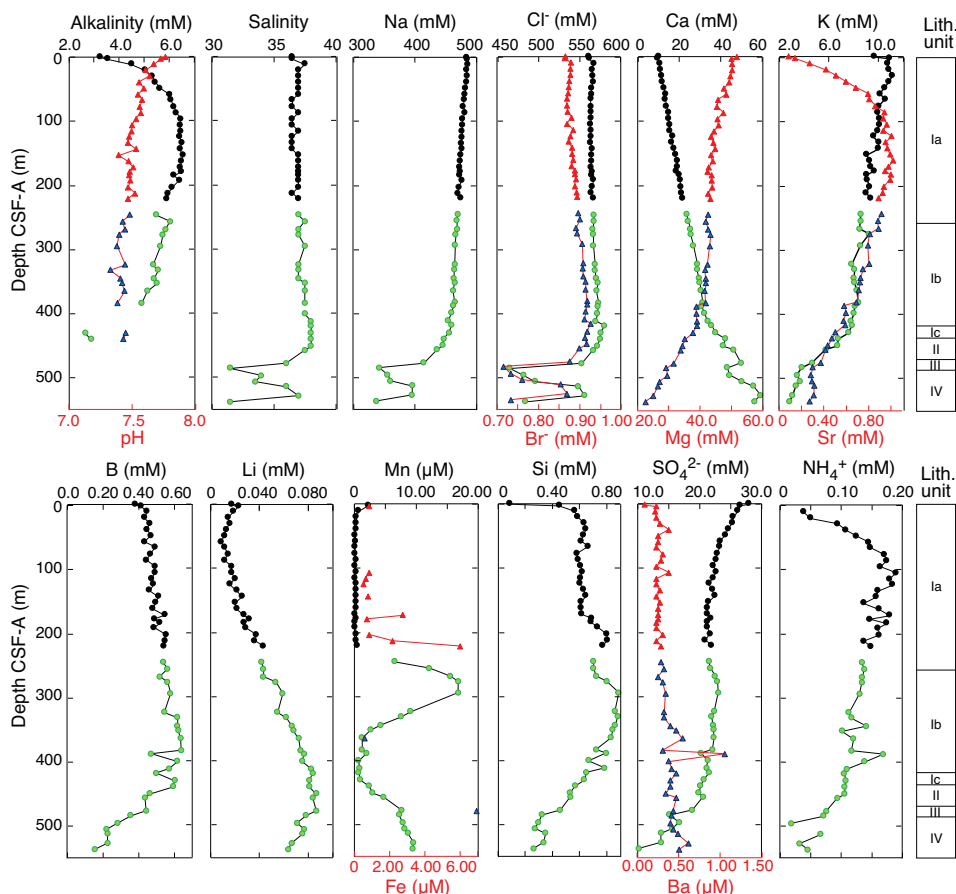
Sulfate and ammonium

SO₄²⁻ concentration decreases from 28 mM at the mudline to 22 mM at 105.6 m CSF-A (Sample 369-U1516A-12H-4, 140–150 cm), is constant between 20 and 23 mM from 105.6 to 457.10 m

Table T16. Gas element data, Site U1514. [Download table in CSV format.](#)

Table T17. Interstitial water geochemistry, Holes U1516A and U1516C. [Download table in CSV format.](#)

Figure F26. Interstitial water alkalinity, pH, and element and ion concentrations, Site U1516. Black circles, red triangles = Hole U1516A, green circles, blue triangles = Hole U1516C.



CSF-A (Sections 369-U1516A-12H-4 through 369-U1516C-29R-2), and then decreases again to 10 mM at the bottom of the cored interval (Table T17; Figure F26). NH_4^+ concentration increases from below detection limit in the mudline sample to 189 μM at 105.60 m CSF-A (Sample 369-U1516A-12H-4, 140–150 cm) and then slowly decreases to 18 μM at 496.54 m CSF-A (Sample 369-U1516C-37R-2, 141–151 cm). Trends in both SO_4^{2-} and NH_4^+ concentrations suggest low organic matter metabolization rates in the upper 100 m of the sedimentary column followed by an interval with almost no change in SO_4^{2-} and depletion in NH_4^+ (throughout the lower section of lithostratigraphic Subunits Ia and Ib). In Units II–IV, SO_4^{2-} concentration decreases further, possibly related to higher organic matter concentrations (and thus higher rates of bacterial sulfate reduction) at greater depth. The dilution effect caused by low-salinity water in Units II–IV disappears when elemental concentrations are normalized to Cl^- (not shown).

Magnesium and potassium

Dissolved Mg and K concentrations decrease with depth (Table T17; Figure F26). Mg concentration decreases from 58 mM at the mudline to 23 mM in the deepest sample (537.71 m CSF-A). K concentration decreases steadily from 11 mM at 2.98 m CSF-A (Sample 369-U1516A-1H-2, 148–153 cm) to 7 mM at 450.82 m CSF-A (Sample 369-U1516C-28R-4, 108–113 cm) and then decreases more sharply from 457.10 to 537.71 m CSF-A (Sections 369-U1516C-29R-2 through 41R-4). The coupled changes in K and Mg concentrations reflect volcanic material alteration reactions likely present in the sedimentary record below the drilled depths at this site (e.g., Gieskes and Lawrence 1981) (see below).

Calcium and strontium

Dissolved Ca concentration linearly increases downhole to lithostratigraphic Subunit Ic and then increases with a steeper gradient, reaching a maximum of 59 mM at 528.04 m CSF-A (Sample 369-U1516C-40R-4, 142–152 cm) (Table T17; Figure F26). This steeper gradient is due to the release of Ca during volcanic material alteration reactions (e.g., Bischoff and Dickson, 1975). The slight Ca concentration decrease in the low-salinity interval of lithostratigraphic Unit IV disappears when concentration is normalized to Cl^- . Dissolved Sr concentration increases from 0.88 mM at the mudline to 1.02 mM at 162.60 m CSF-A (Sample 369-U1516A-18H-4, 140–150 cm) and then decreases to 0.28 mM at the bottom of the hole. The low-salinity input in Unit IV disappears when Sr is normalized to Cl^- . The Sr concentration profile is highly influenced by carbonate diagenesis in carbonate-rich Subunit Ia. At greater depths, a Sr removal process must be operating.

Chloride, bromide, sodium, and lithium

The interstitial water concentration profiles of Cl^- and Br^- are similar. Cl^- concentration is essentially constant with minimal variation (561–580 mM) from the mudline to 485.38 m CSF-A (Sample 369-U1516C-35R-2, 138–148 cm). Cl^- concentration decreases drastically to 464–556 mM in lithostratigraphic Unit IV, coincident with the decrease in salinity (Table T17; Figure F26). The Br^- concentration profile is similar to that of Cl^- even though concentration increases gradually (from 0.86 to 0.93 mM) toward Subunit Ic. In Units II–IV, Br^- concentration decreases (0.72–0.87 mM) because of lower salinity water in Unit IV. The Br^-/Cl^- ratio (not shown) increases downhole to Subunit Ic as a result of the release of Br^- from organic matter during remineralization. Br^- decreases in Units II–IV; the large scatter in Unit IV is associated with salinity changes.

Na concentration decreases slightly with depth from 486 mM at 10.61 m CSF-A (Sample 369-U1516A-2H-4, 141–151 cm) to 454 mM at 412.0 m CSF-A (Section 369-U1516C-24R-4). A distinct decrease in concentration occurs in and below lithostratigraphic Subunit Ic, coincident with the low-salinity water in this depth range (Table T17; Figure F26). The Na/Cl ratio (not shown) decreases linearly downhole from seawater-like values around 0.86 to 0.80 at 412.0 m CSF-A. Below the condensed Paleocene interval in Subunit Ic, the Na/Cl ratio decreases steeply to 0.70, indicating that changes in Na must be associated with basement alteration reactions similar to those seen at Site U1513 (see [Geochemistry](#) in the Site U1513 chapter [Huber et al., 2019b]).

Li concentration decreases from seawater-like values (0.02 mM in Section 369-U1516A-1H-2) to a minimum of 0.01 mM at 58.1 m CSF-A (Sample 7H-4, 140–150 cm) and then increases to a maximum of 0.09 mM in lithostratigraphic Subunits Ic, IIa, and IIb before decreasing again through Unit IV (Table T17; Figure F26). The Li and Li/Cl ratio depth profiles are very similar and suggest that the upper interval of Unit IV, where the freshening is most pronounced, may represent the source for Li enrichment.

Barium, boron, and silicon

Ba concentration is strongly related to the presence or absence of SO_4^{2-} in interstitial water (Torres et al., 1996) (Table T17; Figure F26). SO_4^{2-} is present throughout Site U1516; therefore, Ba concentration is barely above detection limit, primarily $<1 \mu\text{M}$, following the solubility product of barite (Church and Wolgemuth, 1972).

Dissolved Si concentration increases from 0.09 to 0.60 mM from the mudline to Section 369-U1516A-2H-4 and then remains fairly constant downhole to Section 18H-4 (162.60 m CSF-A). Si concentration further increases in the lower part of lithostratigraphic Subunits Ia and Ib. Generally, high Si concentration reflects the presence of biogenic siliceous tests and sponge spicules (Table T17; Figure F26). Below the condensed interval in Subunit Ic, Si concentration decreases to 457 μM at 477.83 m CSF-A (Sample 369-U1516C-33R-3, 130–140 cm). Dissolved Si concentration decreases further in Unit IV to values typical for intervals below the opal-A/CT boundary (Murray et al., 1992).

B concentration increases gradually from 0.38 mM in the mudline sample to a maximum of 0.64 mM at 383.37 m CSF-A (Sample 369-U1516C-21R-4, 96–106 cm), followed by a general decrease between 383.37 and 537.71 m CSF-A (Table T17; Figure F26). Adsorption/desorption and alteration reactions within the sedimentary column are likely responsible for this decrease (Brumsack and Zuleger, 1992). B concentration does not appear to be significantly influenced by the low-salinity interstitial water present in lithostratigraphic Unit IV.

Manganese and iron

Two intervals of increasing Mn concentration occur in the sediment profile: one starting near the bottom of lithostratigraphic Subunit Ia and continuing to the top of Subunit Ib (246.25–365.01 m CSF-A; Sections 369-U1516C-7R-2 through 19R-4) and a smaller one starting in Unit II and continuing to Unit IV (440.28–537.71 m CSF-A; Sections 27R-3 through 41R-4). This second maximum is not altered by the low-salinity water in Unit IV (Table T17; Figure F26) when considering Mn/Cl ratio (not shown). The high Mn concentration reflects the reducing character of the sedimentary column in parts of Subunits Ia and Ib and Units II–IV, an idea supported by the presence of green and/or black sediment intervals.

The Mn concentration minimum around 400 m CSF-A occurs in the highly condensed oxic interval of Subunit Ic.

For Fe, only a few reliable values could be generated because of the rapid oxidation of this element during the squeezing process (Table T17; Figure F26). Noticeably high Fe concentration is mostly detected at the bottom of lithostratigraphic Subunit Ia (172.10–220.31 m CSF-A; Sections 369-U1516A-19H-4 through 29F-1) and at 477.83 m CSF-A (Section 369-U1516C-33R-3). The reducing character of the sedimentary column, the presence of green intervals, and the high Mn concentration, in combination with low bacterial SO_4^{2-} reduction rates, suggest that Fe concentration likely was higher in situ.

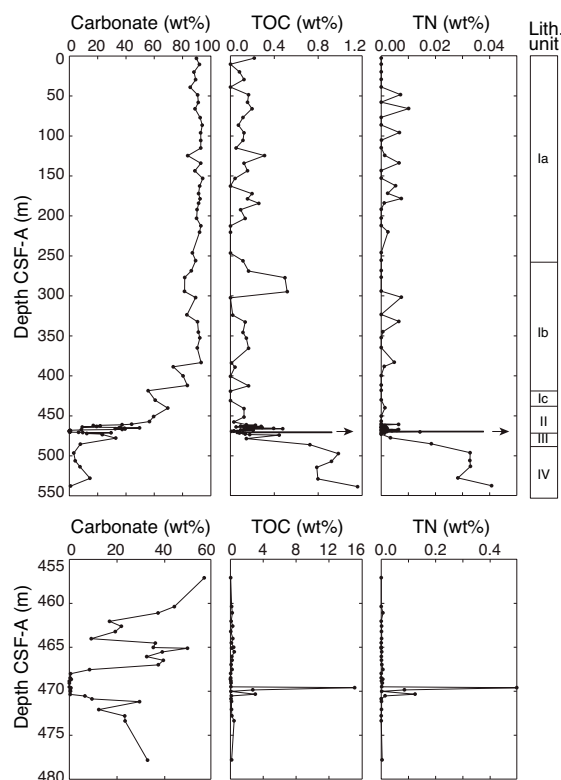
Bulk sediment geochemistry

A total of 43 bulk sediment samples were collected to ~540 m CSF-A (Core 369-U1516C-41R). For standard low-resolution analyses, these samples were taken from the interstitial water squeeze cake when an interstitial water sample was taken; otherwise, a small sample was taken from the working-half section. Additional samples were taken in the anticipated OAE 2 interval spanning Cores 30R through 32R.

Carbonate content at this site ranges from 0.10 to 94 wt% (Table T18; Figure F27). It is highest in lithostratigraphic Subunits Ia and Ib and decreases through Subunit Ic to Unit IV. Carbonate content is lowest in the greenish clay samples from the Cenomanian/Turonian boundary interval, where values dropped to ~0 wt%.

Table T18. Bulk sediment geochemistry, Site U1514. [Download table in CSV format.](#)

Figure F27. Carbon and total nitrogen (TN), Site U1516. TOC and TN values are near the detection limit. Lower plots are expanded across the inferred OAE 2 interval.



Total organic carbon (TOC) content at this site ranges from 0 to 14 wt% (Figure F27; Table T18) and is generally low (~0.2 wt%) in lithostratigraphic Units I and II downhole to 457 m CSF-A. TOC content in Unit III, the suspected OAE 2 interval, varies significantly with lithology. The greenish gray claystone has a TOC content of <0.1 wt% (Sections 369-U1516C-31R-3, 31R-4, and 32R-1), whereas the black layers in the sections contain 2–14 wt% TOC.

Total nitrogen (TN) content is below detection level for more than half of the samples from lithostratigraphic Units I and II; samples with quantifiable TN do not reach 0.05 wt%. Because TOC and TN contents are near the detection limit, the TOC/TN ratio is subject to significant error from 0–457 m CSF-A. In comparison, TOC and TN contents in Units III and IV were sufficiently high to reliably evaluate the TOC/TN ratio. The TOC/TN ratio in Unit III shows large variation (~8–50) through the suspected OAE 2 interval but is relatively stable (23–41) in Unit IV, which suggests the organic matter in the Unit IV samples are of terrestrial origin.

Organic matter source analysis

Three samples with ≥ 0.8 wt% TOC based on bulk-rock analyses and additional samples from the likely OAE 2 horizon were evaluated during source rock analysis (SRA). TOC content was independently evaluated based on detection of pyrolyzed organic matter. Because this calculation of TOC content employs a different analytical method than that used for bulk sediment, these TOC values do not necessarily correspond to TOC values reported from bulk sediment analysis (see **Bulk sediment geochemistry**). To discriminate TOC content derived from regular bulk sediment analysis, we designate values calculated during SRA as TOC_{SRA} . Measurements with low TOC_{SRA} values (<0.8 wt%) have large uncertainties and potentially overestimate hydrogen index (HI) and oxygen index (OI) values. The nominal temperature of the maximum rate of hydrocarbon yield (T_{max}) from these samples with low TOC_{SRA} also varies greatly and cannot be employed for estimating the thermal maturity of organic matter.

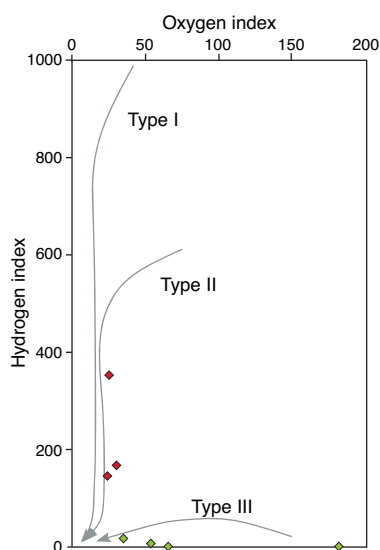
Samples with high TOC_{SRA} content (>2 wt%) are interpreted to contain Type II kerogen with a likely predominant marine algal source (Table T19; Figure F28). Lower HI values from Samples 369-U1516C-31R-4, 120–121 cm, and 32R-1, 75–76 cm, may indicate a degraded state of Type II kerogen. The HI and OI of samples with low TOC_{SRA} content (<2 wt%) suggest Type IV kerogen or degraded organic matter (Peters et al., 2004). The composition of organic matter in samples from Cores 37R, 38R, and 41R (which contain ~1 wt% TOC_{SRA}) indicates Type IV kerogen and an exclusively terrestrial source. However, the low TOC content in these samples mean this interpretation is qualified.

The black layers in the suspected OAE 2 interval (red diamonds in Figure F28) have the highest TOC_{SRA} content. Sample 369-U1516C-32R-1, 1–2 cm, located at the top of an 8 cm thick black layer, has the highest TOC_{SRA} content (14.0 wt%) and HI value (352 mg hydrocarbon (HC)/g TOC), indicating Type II kerogen. Greenish clay samples with low TOC_{SRA} content (<0.7 wt%) yielded a very small (~0.02) S2 peak but a relatively large S3 peak (>0.20), suggesting a terrestrial source; however, the low absolute height of the S2 peak means uncertainty is high in this inference. T_{max} values obtained from samples containing ≥ 1 wt% TOC_{SRA} range from 411° to 431°C (except for Sample 369-U1516C-30R-3, 27–28 cm, for which S2 was below detection), indicating that the organic matter is thermally immature.

Table T19. Source rock analysis data, Site U1516. * = less reliable data because of low total organic carbon (TOC) value. HC = hydrocarbon, T_{max} = nominal temperature of the maximum rate of hydrocarbon yield, HI = hydrogen index, OI = oxygen index, PI = production index. [Download table in CSV format.](#)

Core, section, interval (cm)	Depth CSF-A (m)	S1 (mg HC/g rock)	S2 (mg HC/g rock)	S3 (mg HC/g rock)	T_{max} (°C)	TOC (wt%)	HI	OI	PI
369-U1516C-									
30R-3, 27–28	463.22	0.08	0.00	1.86	313.9	1.03	0*	181	1.00*
31R-2, 59–60	466.48	0.07	0.00	1.00	335.0	0.66*	0*	151*	1.00*
31R-3, 84–85	468.00	0.09	0.02	0.27	443.3	0.06*	32*	465*	0.83*
32R-1, 1–2	469.61	0.63	49.09	3.52	414.6	13.96	352	25	0.01
31R-4, 120–121	469.86	0.24	4.30	0.76	428.8	2.57	167	30	0.05
32R-1, 43–44	470.03	0.07	0.02	0.20	437.0	0.17*	14*	114*	0.75*
32R-1, 75–76	470.35	0.11	4.48	0.69	428.9	2.88	155	24	0.02
32R-1, 94–95	470.54	0.07	0.02	1.16	419.6	0.53*	3*	217*	0.79*
37R-2, 141–151	496.54	0.07	0.00	0.84	408.2	1.3	0	65	0.94
38R-3, 109–119	506.27	0.07	0.08	0.75	431.7	1.39	6	54	0.47
41R-4, 143–153	537.76	0.10	0.25	0.56	411.8	1.58	16	35	0.28

Figure F28. Source rock analysis (pyrolysis) results, Site U1516. Red = samples from black layers in the suspected OAE 2 interval, green = samples from other lithologies.



Stratigraphic correlation

At Site U1516, Hole U1516A was cored with the APC and HLAPC systems to 223.72 m CSF-A. Recovery was 104%, and only 1 of 29 cores had <100% recovery. Hole U1516C was drilled to 196 m DSF, where coring with the RCB system commenced. The hole was then continuously cored to 540.10 m CSF-A with an average recovery of 60%. Hole U1516D was advanced to 458.0 m DSF and then cored with the RCB system to 477.60 m CFS-A with 95% recovery. A splice was made for overlapping cored intervals in Holes U1516C and U1516D that cover the upper Cenomanian to lower Turonian.

Guidance for coring

Prior to coring Hole U1516C, target depths were recommended based on the occurrence of discrete features in the physical property records from the lowermost 20 m of core recovered from Hole U1516A. Specifically, four peaks in NGR (~2 counts/s over base levels; see [Petrophysics](#)) were identified as targets for correlation in the 205–218 m CSF-A interval. Because sediment is relatively un-

consolidated in this interval, recovery was expected to be limited, motivating the decision to begin coring at 196 m DSF. Unfortunately, recovery was poor in Cores 369-U1516C-2R through 6R (11.5% average recovery), and no features were recognized that would allow us to confidently correlate between Holes U1516A and U1516C. Therefore, no splice was attempted.

Efforts to bridge coring gaps and to correlate precisely between overlapping portions of Holes U1516C and U1516D was much more successful than the analogous efforts for overlapping portions of Holes U1516A and U1516C. We devised a coring strategy to work backward from the depth of a target horizon recognizable by a distinct set of beds with characteristic NGR and magnetic susceptibility variation patterns. This target horizon occurs near the midpoint of a high-priority 4 m thick interval inferred to represent deposition during the peak of OAE 2. In Hole U1516C, the horizon occurs at the level of a core break. Recovery of shorter cores was better than recovery of full cores in Hole U1516C, and the value of this improved recovery seemed to outweigh the cost of an increased number of core breaks. Based on these observations, our strategy was to cut a 6 m core centered on the target horizon with two 4.5 m long cores preceding it and one 4.5 m core following it (Table T1). Both NGR and magnetic susceptibility data collected as soon as possible after Core 369-U1516D-2R was curated suggest that the driller hit the target depth within 25 cm of the predicted level. Subsequent coring proceeded without adjustments. Recovery for the four Hole U1516D cores averaged 95%.

Correlation of cores

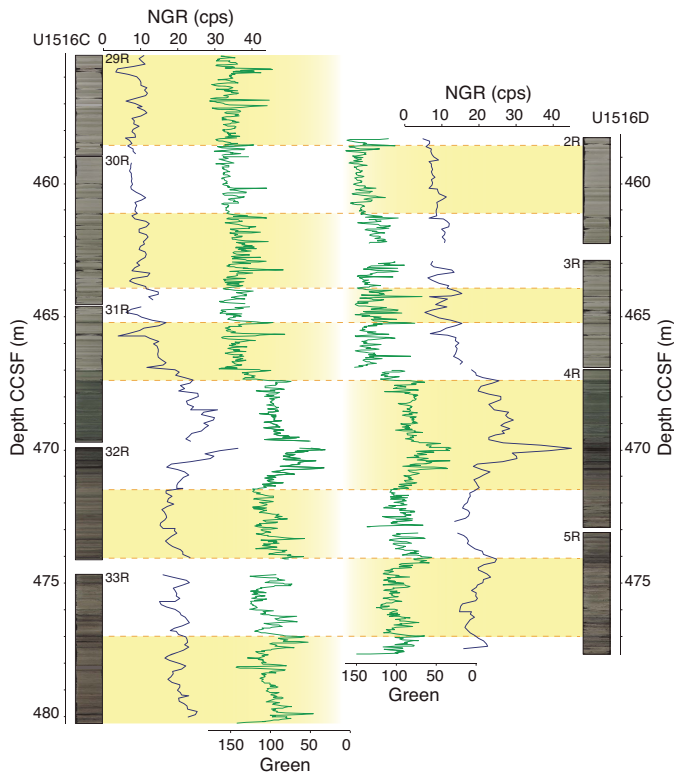
Holes U1516A and U1516C

As discussed above, poor recovery in Cores 369-U1516C-2R through 6R precluded correlation between Holes U1516A and U1516C at a finer resolution than that provided by the CSF-A scale.

Holes U1516C and U1516D

The interval cored in both Holes U1516C and U1516D from 458 to 477.5 m CSF-A (Cores 369-U1516C-29R through 33R and 369-U1516D-2R through 6R) contains distinctive variations in physical properties and lithology that allow for accurate correlation between holes (Figure F29). Most notable are several 5–20 cm thick organic-rich beds interpreted to represent a local extreme in depositional conditions during the OAE 2 interval. Moreover, color, lithology, NGR, and magnetic susceptibility all show correlatable patterns with centimeter-scale resolution and confirm the accuracy of the splice. The splice, although floating relative to the seafloor, contains no aligned coring gaps or obvious intervals of drilling disturbance.

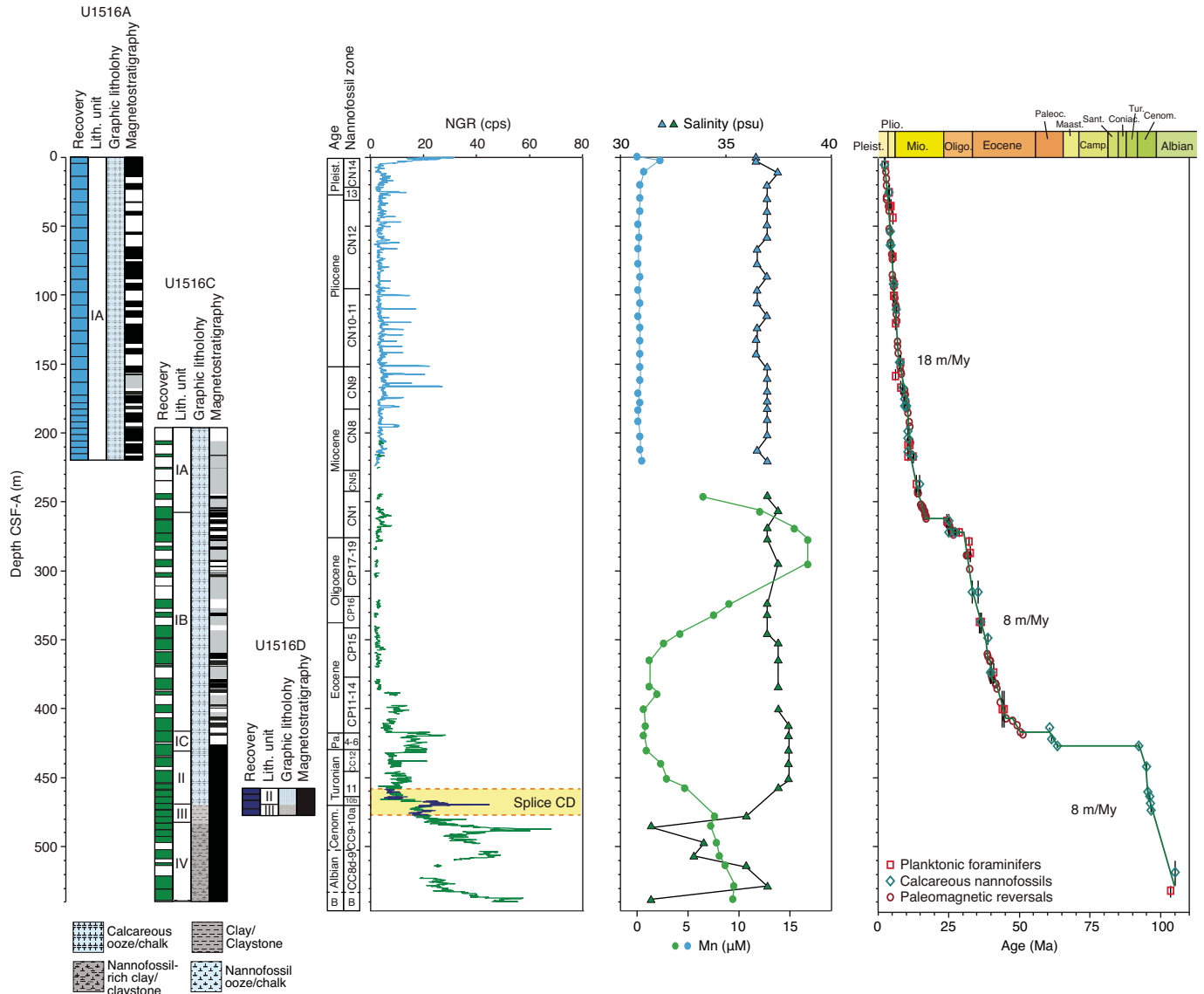
Figure F29. Correlation of Holes U1516C and U1516D from 455 to 480 m CCSF. RGB green data is an apparently sensitive color band to locate dark beds in the cores. Yellow shading = intervals selected for the splice.



Summary

Hole U1516A cores provide a 225 m thick, continuous record of middle Miocene to recent deposition at this site. Although reworking is recognized in microfossil residues, indicating some sedimentological complexity, the sequence seems to be biostratigraphically and magnetostratigraphically complete. Large coring gaps in Hole U1516C compromise the record of the early Miocene, much of the Oligocene, and portions of the Eocene, but both the Oligocene/Miocene boundary interval and a 30 m long late Eocene interval were well recovered. Much of the Late Cretaceous, all of the Paleocene, and much of the Eocene are either missing or represented in a 15 m thick interval of condensed deposition and/or erosion and nondeposition spanning from Section 369-U1516C-26R-4, 106 cm, to the top of Core 25R. Sediment accumulation during the late Albian to middle Turonian, in comparison, seems to have been continuous, albeit at a modest sedimentation rate of 8 m/My (Figure F30).

Figure F30. Site U1516 summary. Hole U1516B (~16 m) was sampled completely on the catwalk. Light blue = Hole U1516A, green = Hole U1516C, dark blue = Hole U1516D. Yellow shading = floating spliced interval.



References

- Bischoff, J.L., and Dickson, F.W., 1975. Seawater-basalt interaction at 200°C and 500 bars: implications for origin of sea-floor heavy-metal deposits and regulation of seawater chemistry. *Earth and Planetary Science Letters*, 25(3):385–397. [https://doi.org/10.1016/0012-821X\(75\)90257-5](https://doi.org/10.1016/0012-821X(75)90257-5)
- Borissova, I., 2002. *Geological Framework of the Naturaliste Plateau*. Geoscience Australia, 2002/20. <http://www.ga.gov.au/metadata-gateway/metadata/record/40535/>
- Brumsack, H.-J., and Zuleger, E., 1992. Boron and boron isotopes in pore waters from ODP Leg 127, Sea of Japan. *Earth and Planetary Science Letters*, 113(3):427–433. [https://doi.org/10.1016/0012-821X\(92\)90143-J](https://doi.org/10.1016/0012-821X(92)90143-J)
- Church, T.M., and Wolgemuth, K., 1972. Marine barite saturation. *Earth and Planetary Science Letters*, 15(1):35–44. [https://doi.org/10.1016/0012-821X\(72\)90026-X](https://doi.org/10.1016/0012-821X(72)90026-X)
- De Vleeschouwer, D., Dunlea, A.G., Auer, G., Anderson, C.H., Brumsack, H., de Loach, A., Gurnis, M., et al., 2017. Quantifying K, U, and Th contents of marine sediments using shipboard natural gamma radiation spectra measured on DV JOIDES Resolution. *Geochemistry, Geophysics, Geosystems*, 18(3):1053–1064. <https://doi.org/10.1002/2016GC006715>
- Expedition 320T Scientists, 2009. *Expedition 320T Preliminary Report: USIO Sea Trials and Assessment of Readiness Transit (START): Ontong Java Plateau*. Integrated Ocean Drilling Program. <https://doi.org/10.2204/iodp.pr.320T.2009>
- Falzone, F., Petrizzo, M.R., Jenkyns, H.C., Gale, A.S., and Tsikos, H., 2014. Planktonic foraminiferal biostratigraphy and assemblage composition across the Cenomanian–Turonian boundary interval at Clot Chevalier (Vocontian Basin, SE France). *Cretaceous Research*, 59:69–97. <https://doi.org/10.1016/j.cretres.2015.10.028>
- Gale, A.S., Bown, P., Caron, M., Crampton, J., Crowhurst, S.J., Kennedy, W.J., Petrizzo, M.R., and Wray, D.S., 2011. The uppermost middle and upper Albian succession at the Col de Palluel, Hautes-Alpes, France: an integrated study (ammonites, inoceramid bivalves, planktonic foraminifera, nannofossils, geochemistry, stable oxygen and carbon isotopes, cyclostratigraphy). *Cretaceous Research*, 32(2):59–130. <https://doi.org/10.1016/j.cretres.2010.10.004>
- Gieskes, J.M., Gamo, T., and Brumsack, H., 1991. *Technical Note 15: Chemical Methods for Interstitial Water Analysis Aboard JOIDES Resolution*. Ocean Drilling Program. <https://doi.org/10.2973/odp.tn.15.1991>

- Gieskes, J.M., and Lawrence, J.R., 1981. Alteration of volcanic matter in deep-sea sediments: evidence from the chemical composition of interstitial waters from deep sea drilling cores. *Geochimica et Cosmochimica Acta*, 45(10):1687–1703. [https://doi.org/10.1016/0016-7037\(81\)90004-1](https://doi.org/10.1016/0016-7037(81)90004-1)
- Gradstein, F.M., Ogg, J.G., Schmitz, M.D., and Ogg, G.M. (Eds.), 2012. *The Geological Time Scale 2012*: Amsterdam (Elsevier).
- Huber, B.T., Hobbs, R.W., Bogus, K.A., Batenburg, S.J., Brumsack, H.-J., do Monte Guerra, R., Edgar, K.M., Edvardsen, T., Garcia Tejada, M.L., Harry, D.L., Hasegawa, T., Haynes, S.J., Jiang, T., Jones, M.M., Kuroda, J., Lee, E.Y., Li, Y.-X., MacLeod, K.G., Maritani, A., Martinez, M., O'Connor, L.K., Petrizzo, M.R., Quan, T.M., Richter, C., Riquier, L., Tagliaro, G.T., Wainman, C.C., Watkins, D.K., White, L.T., Wolfring, E., and Xu, Z., 2019a. Expedition 369 methods. In Hobbs, R.W., Huber, B.T., Bogus, K.A., and the Expedition 369 Scientists, *Australia Cretaceous Climate and Tectonics*. Proceedings of the International Ocean Discovery Program, 369: College Station, TX (International Ocean Discovery Program). <https://doi.org/10.14379/iodp.proc.369.102.2019>
- Huber, B.T., Hobbs, R.W., Bogus, K.A., Batenburg, S.J., Brumsack, H.-J., do Monte Guerra, R., Edgar, K.M., Edvardsen, T., Garcia Tejada, M.L., Harry, D.L., Hasegawa, T., Haynes, S.J., Jiang, T., Jones, M.M., Kuroda, J., Lee, E.Y., Li, Y.-X., MacLeod, K.G., Maritani, A., Martinez, M., O'Connor, L.K., Petrizzo, M.R., Quan, T.M., Richter, C., Riquier, L., Tagliaro, G.T., Wainman, C.C., Watkins, D.K., White, L.T., Wolfring, E., and Xu, Z., 2019b. Site U1513. In Hobbs, R.W., Huber, B.T., Bogus, K.A., and the Expedition 369 Scientists, *Australia Cretaceous Climate and Tectonics*. Proceedings of the International Ocean Discovery Program, 369: College Station, TX (International Ocean Discovery Program). <https://doi.org/10.14379/iodp.proc.369.104.2019>
- Kaminski, M.A., and Gradstein, F.M., 2005. Atlas of Paleogene cosmopolitan deep-water agglutinated foraminifera. *Grzybowski Foundation Special Publication*, 10. <http://www.foraminifera.eu/atlas.html>
- Kirschvink, J.L., 1980. The least-squares line and plane and the analysis of palaeomagnetic data. *Geophysical Journal of the Royal Astronomical Society*, 62(3):699–718. <https://doi.org/10.1111/j.1365-246X.1980.tb02601.x>
- Lurcock, P.C., and Wilson, G.S., 2012. PuffinPlot: a versatile, user-friendly program for paleomagnetic analysis. *Geochemistry, Geophysics, Geosystems*, 13(6):Q06Z45. <https://doi.org/10.1029/2012GC004098>
- Maloney, D., Sargent, C., Diren, N.G., Hobbs, R.W., and Gröcke, D.R., 2011. Re-evaluation of the Mentelle Basin, a polyphase rifted margin basin, offshore southwest Australia: new insights from integrated regional seismic datasets. *Solid Earth*, 2(2):107–123. <https://doi.org/10.5194/se-2-107-2011>
- Norris, R.D., Wilson, P.A., Blum, P., Fehr, A., Agnini, C., Bornemann, A., Boulila, S., Bown, P.R., Cournede, C., Friedrich, O., Ghosh, A.K., Hollis, C.J., Hull, P.M., Jo, K., Junium, C.K., Kaneko, M., Liebrand, D., Lippert, P.C., Liu, Z., Matsui, H., Moriya, K., Nishi, H., Opdyke, B.N., Penman, D., Romans, B., Scher, H.D., Sexton, P., Takagi, H., Turner, S.K., Whiteside, J.H., Yamaguchi, T., and Yamamoto, Y., 2014. Site U1405. In Norris, R.D., Wilson, P.A., Blum, P., and the Expedition 342 Scientists, *Proceedings of the Integrated Ocean Drilling Program*, 342: College Station, TX (Integrated Ocean Drilling Program). <http://dx.doi.org/10.2204/iodp.proc.342.106.2014>
- Ogg, J.G., 2012. Geomagnetic polarity time scale. In Gradstein, F.M., Ogg, J.G., Schmitz, M.D., and Ogg, G.M. (Eds.), *The Geologic Time Scale 2012*: Amsterdam (Elsevier), 85–113. <https://doi.org/10.1016/B978-0-444-59425-9.00005-6>
- Pearson, P.N., Olsson, R.K., Hemleben, C., Huber, B.T., and Berggren, W.A., 2006. Atlas of Eocene planktonic foraminifera. *Special Publication - Cushman Foundation for Foraminiferal Research*, 41.
- Peters, K.E., Walters, C.C., and Moldowan, J.M., 2004. *The Biomarker Guide (Volume 2): Biomarkers and Isotopes in Petroleum Systems and Earth History (2nd edition)*: Cambridge, United Kingdom (Cambridge University Press). <https://doi.org/10.1017/CBO9781107326040>
- Petrizzo, M.R., 2000. Upper Turonian–lower Campanian planktonic foraminifera from southern mid–high latitudes (Exmouth Plateau, NW Australia): biostratigraphy and taxonomic notes. *Cretaceous Research*, 21(4):479–505. <https://doi.org/10.1006/cres.2000.0218>
- Petrizzo, M.R., 2001. Late Cretaceous planktonic foraminifera from the Kerguelen Plateau (ODP Leg 183): new data to improve the Southern Oceans biozonation. *Cretaceous Research*, 22(6):829–855. <https://doi.org/10.1006/cres.2001.0290>
- Petrizzo, M.R., 2003. Late Cretaceous planktonic foraminiferal bioevents in the Tethys and in the Southern Ocean record: an overview. *Journal of Foraminiferal Research*, 33(4):330–337. <https://doi.org/10.2113/0330330>
- Petrizzo, M.R., and Huber, B.T., 2006. Biostratigraphy and taxonomy of late Albian planktonic foraminifer from ODP Leg 171B (western North Atlantic). *Journal of Foraminiferal Research*, 36(2):166–190. <https://doi.org/10.2113/36.2.166>
- Premoli Silva, I., and Sliter, W.V., 1995. Cretaceous planktonic foraminiferal biostratigraphy and evolutionary trends from the Bottaccione section, Gubbio, Italy. *Palaeontographia Italica*, 82:2–90.
- Pribnow, D., Kinoshita, M., and Stein, C., 2000. *Thermal Data Collection and Heat Flow Recalculations for Ocean Drilling Program Legs 101–180*: Hanover, Germany (Institute for Joint Geoscientific Research, Institut für Geowissenschaftliche Gemeinschaftsaufgaben [GGA]). <http://www-odp.tamu.edu/publications/heatflow/ODPREprt.pdf>
- Richter, C., Acton, G., Endris, C., and Radsted, M., 2007. *Technical Note 34: Handbook for Shipboard Paleomagnetists*. Ocean Drilling Program. <https://doi.org/10.2973/odp.tn.34.2007>
- Torres, M.E., Brumsack, H.-J., Bohrmann, G., and Emeis, K.C., 1996. Barite fronts in continental margin sediments: a new look at barium remobilization in the zone of sulfate reduction and formation of heavy barites in diagenetic fronts. *Chemical Geology*, 127(1–3):125–139. [https://doi.org/10.1016/0009-2541\(95\)00090-9](https://doi.org/10.1016/0009-2541(95)00090-9)
- van Morkhoven, F.P.C.M., Berggren, W.A., Edwards, A.S., and Oertli, H.J., 1986. Cenozoic cosmopolitan deep-water benthic foraminifera. *Bulletin des Centres de Recherches Exploration-Production Elf-Aquitaine: Mémoire*, 11.
- Wade, B.S., Pearson, P.N., Berggren, W.A., and Pälike, H., 2011. Review and revision of Cenozoic tropical planktonic foraminiferal biostratigraphy and calibration to the geomagnetic polarity and astronomical time scale. *Earth-Science Reviews*, 104(1–3):111–142. <https://doi.org/10.1016/j.earscirev.2010.09.003>
- Zijderveld, J.D.A., 1967. AC demagnetization of rocks: analysis of results. In Collinson, D.W., Creer, K.M., and Runcorn, S.K. (Eds.), *Developments in Solid Earth Geophysics (Volume 3): Methods in Palaeomagnetism*: Amsterdam (Elsevier), 254–286. <https://doi.org/10.1016/B978-1-4832-2894-5.50049-5>